SCUOLA DI DOTTORATO

UNIVERSITÀ DEGLI STUDI DI MILANO-BICOCCA

Dipartimento di Scienze dell'Ambiente e della Terra

Dottorato in Scienze Chimiche, Geologiche e Ambientali XXXVII ciclo

curriculum Scienze Geologiche

TIME-LAPSE ELECTRICAL TOMOGRAPHY FOR MONITORING BACTERIAL COMMUNITY DEVELOPMENT ON A BURIED POLLUTED SOIL VOLUME IN EXTREME ENVIRONMENTAL CONDITIONS

Giacomo Upendo Caniatti
Mat. 071272

Tutor: Giovanni Crosta

Supervisor: Paolo Frattini

Coordinator: Marco G. Malusa' **ACADEMIC YEAR** **2024/2025**

Index

1 Introduction

1.1 Background and motivation

Hydrocarbon contamination of soils and groundwater represents one of the most pervasive forms of environmental degradation worldwide. Spills from petroleum storage, transport, and industrial activities introduce complex mixtures of aliphatic and aromatic hydrocarbons that persist for decades. These compounds not only alter the geochemical balance of subsurface environments but also threaten ecosystems and human health (Sales da Silva et al., 2020). Effective remediation therefore requires not only removing pollutants but also monitoring the underlying biogeochemical transformations in situ.

From a management perspective, remediation success increasingly relies on process-based monitoring that can discriminate whether and where microbially mediated transformation (MMT) is occurring. Traditional point sampling is informative but sparse in space and time, often missing the heterogeneity that controls contaminant fate. Conversely, geophysical monitoring provides volumetric coverage and high temporal resolution, enabling the observation of evolving plumes and reaction fronts. This motivates the integration of electrical methods with microbiology and geochemistry within a unified biogeophysical framework (Atekwana & Slater, 2009).

At the core of this framework is the recognition that microbial metabolism and hydrocarbon weathering modify pore-water chemistry and interfacial properties, which in turn impact bulk electrical conductivity. Because these feedbacks unfold over days to months, time-lapse (4D) ERT is a natural candidate to capture their dynamics at relevant scales (Abdulkadir et al., 2019).

1.2 Hydrocarbon contamination and environmental impact

Hydrocarbon pollutants modify both the chemical and physical properties of soils. They create reducing conditions, decrease permeability, and alter ionic concentrations (Sales da Silva et al., 2020). The presence of hydrocarbons also stimulates indigenous or injected microbial communities capable of metabolizing complex organic molecules (Atekwana & Slater, 2009). During degradation, microorganisms generate metabolites, organic acids, biosurfactants, and gases, which influence redox potential and ionic strength, ultimately modifying the electrical conductivity of pore fluids (Abdulkadir et al., 2019). These bioelectrical and electrochemical transformations can be indirectly observed through geophysical signals, linking biological activity to electrical conductivity changes in contaminated sediments (Atekwana et al., 2004a; Atekwana et al., 2004b; Atekwana & Atekwana, 2010).

However, in the early stages of contamination, hydrocarbons behave as electrical insulators, increasing the resistivity of affected soils by displacing conductive pore water and reducing ionic mobility (Atekwana et al., 2000; Revil et al., 2012). Over time, microbial degradation of hydrocarbons can reverse this trend by producing ionic metabolites and acids that enhance conductivity. Consequently, the temporal evolution of resistivity—from initial increase to later decrease—can serve as a diagnostic signal of microbially mediated transformation (MMT) stages.

From a biochemical standpoint, aerobic attack on linear and branched alkanes proceeds via terminal oxidation and β-oxidation pathways, whereas aromatic compounds undergo dioxygenase-mediated ring cleavage; *Rhodococcus erythropolis* is particularly versatile on C5–C16 hydrocarbons and tolerates moderate salinity, though complete mineralization typically requires months (de Carvalho & da Fonseca, 2005). Such time scales imply that, in highly contaminated matrices (> 100,000 ppm), electrical changes are expected to be modest over short monitoring windows—yet still detectable with sensitive time-lapse ERT.

1.3 Traditional remediation monitoring techniques

Conventional monitoring of remediation processes relies on chemical sampling, chromatographic analyses, and microbiological cultures. Although highly specific, these techniques are destructive, spatially limited, and often unrepresentative of subsurface heterogeneity (Sales da Silva et al., 2020). Direct sampling provides valuable information about concentration trends and microbial presence but cannot capture the continuous spatial evolution of degradation fronts.

In contrast, geophysical techniques such as ERT offer high spatial coverage and temporal continuity. The apparent resistivity (ρ_a) is derived from the voltage-to-current ratio scaled by a geometry factor (Binley & Kemna, 2005; Loke, 2021). Time-lapse ERT imaging provides a powerful framework for monitoring changes in subsurface electrical properties during bioremediation (Abdulkadir et al., 2019). Laboratory experiments have confirmed that time-lapse ERT can successfully detect the migration and microbially mediated transformation (MMT) of petroleum hydrocarbons, with resistivity variations reflecting the concentration, saturation, and ionic composition of pore fluids (Abdulkadir et al., 2019; Atekwana & Slater, 2009). When combined with laboratory analyses, ERT can reveal how microbial and chemical processes evolve in space and time.

Table 1.1 – *Conceptual comparison between traditional chemical/microbial sampling and time-lapse ERT monitoring approaches, illustrating differences in spatial and temporal resolution, invasiveness, and process specificity as discussed in Section 1.3.*

Aspect	Chemical/Microbial Sampling	Time-lapse ERT
Spatial coverage	Sparse points	Volumetric
Temporal resolution	Episodic	High (repeatable 4D)
Invasiveness	Destructive	Non-invasive
Process specificity	High (molecular)	Indirect (needs calibration)
Sensitivity to heterogeneity	High bias	Captures structure

1.4 From Geophysics to Biogeophysics

The concept of *biogeophysics* emerges from the recognition that biological activity leaves measurable geophysical fingerprints. Microbial metabolism, biofilm formation, redox gradients, and mineral precipitation or dissolution all affect the electrical, magnetic, and mechanical properties of the subsurface (Atekwana & Slater, 2009). Among these, electrical resistivity has proven particularly sensitive to ionic variations and interfacial processes.

Since the early 2000s, field investigations have reported conductivity anomalies co-located with hydrocarbon plumes and zones of active microbially mediated transformation (MMT) (Atekwana et al., 2004a; 2004b). These findings established that microbial processes can modify the electrical behaviour of contaminated sediments through increased ionic strength, mineral weathering, and biofilm growth. During the following decade, controlled laboratory experiments and synthetic modelling further consolidated this paradigm, clarifying mechanisms such as surface conduction within biofilms and redox-driven ion release (Atekwana & Atekwana, 2010; Revil et al., 2012).

More recent studies have confirmed that time-lapse Electrical Resistivity Tomography (ERT) can serve as an early-warning proxy for microbially mediated transformation

(MMT) dynamics (Abdulkadir et al., 2019), while pilot-scale tests have demonstrated detectable electrical responses during bioaugmentation with *Rhodococcus* species (Masy et al., 2016). In contrast, in-situ chemical oxidation (ISCO) processes produce monotonic conductivity increases dominated by oxidant chemistry rather than microbial metabolism (Teng et al., 2023). This growing body of research has progressively defined biogeophysics as a quantitative framework linking microbial processes and geophysical observables, yet several aspects of signal attribution remain open.

1.5 Research gap and rationale

Over the past two decades, numerous studies have advanced our understanding of how biological activity influences the electrical properties of soils and sediments (Atekwana & Slater, 2009; Abdulkadir et al., 2019). Nevertheless, distinguishing electrical changes driven by chemical reactions from those produced by microbial processes remains challenging. Temperature fluctuations, ionic migration, moisture variations, and mineral dissolution can easily obscure or mimic biogenic signals, particularly under heterogeneous field conditions.

Building on these substantial achievements, the present work aims to contribute to the ongoing effort to better identify and interpret the electrical expression of microbial activity in hydrocarbon-contaminated systems. The experimental sandbox developed in this PhD research was conceived to isolate and quantify the biogeophysical signature of hydrocarbon degradation under controlled conditions. By combining high-resolution ERT with microbiological analyses, the study investigates the mechanistic link between resistivity variations and bacterial metabolism.

Specifically, the research focuses on differentiating the electrical responses associated with two bacterial strains—*Rhodococcus erythropolis* and *Escherichia coli*—which exhibit distinct metabolic pathways and environmental tolerances. Attention is given to the role of nutrient availability and hydrocarbon toxicity in shaping the observed electrical response, in order to clarify the conditions under which biological activity can be distinguished from purely physicochemical transformations (de Carvalho & da Fonseca, 2005; Sales da Silva et al., 2020).

Ultimately, this work does not attempt to provide a definitive solution, but to add reproducible experimental evidence to a growing field. It aims to refine methodological approaches for coupled monitoring, contribute quantitative metrics for ERT interpretation, and extend laboratory understanding toward real-world, highly contaminated scenarios.

1.6 Biogeophysical coupling: physical and biological interactions

The coupling between physical and biological processes is central to understanding how microbial activity modifies subsurface electrical properties. Microbial growth, biofilm formation, and redox cycling directly influence pore-water conductivity and interfacial polarization (Atekwana & Slater, 2009). Biogeophysics, as defined by Atekwana and Slater (2009), represents a frontier in Earth science where biological processes and geophysical signals are fundamentally intertwined—driven by cell growth, metabolic by-products, and microbe–mineral interactions.

In this thesis, this coupling is operationalized through an integrated workflow combining: high-frequency 4D ERT acquisition, singular value decomposition (SVD) to separate global ionic trends from spatially structured biological residuals, and microbiological validation based on genetic markers (e.g., *Rhodococcus*, *Aquabacterium*).

This framework follows the recommendations of recent laboratory and modelling studies that emphasize joint interpretation, variance-aware data processing, and integration of microbiological evidence (Abdulkadir et al., 2019; Revil et al., 2012). Through this approach, biogeophysical coupling is not treated as a conceptual notion but as a measurable process linking physical signals to microbial function.

1.6.1.1 State of the art and knowledge gaps

The current body of research demonstrates that hydrocarbon contamination generates complex electrical responses arising from both insulating and conductive processes (Atekwana & Slater, 2009; Revil et al., 2012). Initially, hydrocarbons increase resistivity due to their non-conductive nature (Atekwana et al., 2000), while subsequent microbial degradation enhances conductivity through the production of ionic metabolites, organic acids, and conductive biofilms. This dual behaviour reflects the interplay between abiotic and biogenic mechanisms and underlines the difficulty of interpreting electrical data without complementary microbiological or chemical information.

Despite significant advances, several knowledge gaps persist. Quantitative assessment of biogenic versus abiotic contributions remains rare, particularly under conditions of high contaminant toxicity or long-term aging typical of legacy hydrocarbon plumes (Caterina et al., 2017). Furthermore, few controlled experiments explicitly report effect sizes, sensitivity limits, or the reproducibility of resistivity trends (Masy et al., 2016; Abdulkadir et al., 2019). Existing reviews emphasize the need for multivariate frameworks capable of jointly analysing microbial, chemical, and geophysical datasets (Atekwana & Slater, 2009).

Within this context, the present study offers an incremental but significant contribution: it quantifies how 4D ERT responses relate to microbial activity under extreme contamination, tests reproducible analytical workflows (temperature correction, spatial resampling, variance normalization), and provides an empirical basis to refine biogeophysical interpretation in complex, aged hydrocarbon systems (Teng et al., 2023).

1.7 Structure of the thesis

This thesis is structured to follow a progressive logic from conceptual framework to applied results. Chapter 1 introduces the theoretical background and motivation, presenting the evolution from geophysics to biogeophysics and identifying the existing knowledge gaps. Chapter 2 describes the experimental setup, including the sandbox configuration, instrumentation and sampling protocols. Chapter 3 details the geoelectrical acquisition and inversion procedures, as well as data correction and post-processing workflows. Chapter 4 presents the results of resistivity evolution and microbial characterization, focusing on spatial correlations and functional interpretations. Chapter 5 integrates the findings into a broader discussion on biogeophysical mechanisms and implications for monitoring strategies. Finally, Chapter 6 presents interpretative hypothesis and eco-physical framework of the experiment. Chapter 7 summarizes the main conclusions and perspectives for scaling the approach to field applications and environmental monitoring programs.

2 Aim of the study

2.1 General objective

The objective of this PhD research is to evaluate the applicability of time-resolved Electrical Resistivity Tomography (ERT) to investigate the electrical response associated with the injection of two bacterial strains — *Rhodococcus erythropolis* and *Escherichia coli* — into a diesel-contaminated volume. *Rhodococcus erythropolis* is known to degrade hydrocarbons through enzymatic oxidation and biosurfactant-mediated solubilization mechanisms (de Carvalho & da Fonseca, 2005; Pacheco et al., 2010; de Carvalho, 2005), while *E. coli* is not. The idea behind the experiment is to simulate an aged and highly polluted soil body and to test the applicability of ERT as a monitoring tool for remediation interventions in heavily contaminated environments.

To this end, the contaminated volume was left under an extractor hood for 24 hours before being buried in the experimental box and allowed to age for one year. The environment was designed to be extremely toxic by contaminating the soil with an initial diesel concentration exceeding 100,000 ppm. Under such conditions, only limited degradation activity by the bacteria was expected, due to the extreme toxicity of the medium. Nevertheless, the experiment aimed to study the evolution of bacterial and physicochemical responses through continuous ERT monitoring, assessing whether subtle electrical changes could be related to microbial adaptation or to physicochemical re-equilibration processes.

2.2 Specific research aims

This study adopts a process-based biogeophysical perspective in which hydrocarbon contamination initially acts as an electrical insulator — increasing bulk resistivity by displacing conductive pore water — followed by potential conductivity enhancement driven by microbial metabolism, ionic metabolite release, and biofilm-related interfacial conduction (Atekwana et al., 2000; Revil et al., 2012). Consequently, the monitored electrical response is expected to reflect a competition between insulating hydrocarbon phases and conductive biogeochemical products.

Within this framework, *Rhodococcus erythropolis* is anticipated to drive detectable electrical changes under nutrient limited, high toxicity conditions only to a modest extent (de Carvalho & da Fonseca, 2005). *Escherichia coli*, lacking specific hydrocarbon degrading pathways, serves as a negative biological control to test whether observed electrical responses can be attributed to hydrocarbon-specific microbially mediated transformations rather than to generic microbial presence (Atekwana & Slater, 2009). The use of 4D ERT allows volumetric, non-invasive tracking of these coupled processes in space and time (Abdulkadir et al., 2019).

2.3 Research questions

Can time resolved ERT measurements resolve electrical variations following the injection of *R. erythropolis* versus *E. coli* in a highly contaminated and toxic matrix?

To what extent do insulating hydrocarbon phases versus conductive biogenic products dominate the electrical signal over 73 days of monitoring windows?

Under extreme contamination (>100,000 ppm) and long aging (1 year), what is the expected magnitude and spatial coherence of ERT variations attributable to microbial activity?

2.4 Structure and workflow of the study

The experimental workflow was designed to reproduce the main stages of a real contaminated site remediation while maintaining full control of environmental parameters.

The contaminated soil volume was prepared on 24 June 2024, by mixing clean sand and silt with commercial diesel fuel to reach an initial concentration greater than 100,000 ppm. After homogenization, the mixture was left under an extractor hood for 24 hours to stabilize the volatile fractions.

On 27 June 2024**,** the contaminated volume was buried in a dedicated sandbox within a controlled laboratory environment, ensuring constant temperature and humidity. From that date, it underwent a one-year aging period, intended to simulate the physicochemical stabilization typical of mature hydrocarbon spills.

The ERT monitoring campaign began on 7 July 2025, marking the start of the 4D time-lapse acquisition. During this stage, bacterial suspensions of *Rhodococcus erythropolis* and *Escherichia coli* were injected in opposite sectors of the contaminated volume. The experimental protocol included systematic ERT acquisitions, temperature and humidity measurements, and a post-experimental microbiological sampling to support the interpretation of the observed electrical variations.

The workflow of the study can be summarized as follows:

- Preparation of the contaminated volume (24 June 2024).
- Burial and aging phase (27 June 2024 – 7 July 2025).
- Start of 4D ERT monitoring (7 July 2025).

This design ensured temporal separation between contamination, aging, and development phases, allowing the isolation of electrical responses attributable specifically to microbial activity, rather than to physicochemical equilibration of the system.

3 Materials and methods

3.1 Tank, soil and diesel contamination

The experimental setup consisted of a reinforced PVC tank commercial box to simulate a controlled biogeophysical system under hydrocarbon contamination. The tank is a plastic box with internal dimensions of 79 × 52 × 52 cm (L × W × H) and volume about 140 l**.**

The internal stratigraphy comprised three layers:

- a 5 cm basal gravel layer for drainage and mechanical stability approximately 20 kg;
- a 40 cm sandy gravel layer of medium to coarse sand with a primary grain-size range between 200 and 1000 µm, and a modal peak around 800–900 µm (0.8–0.9 mm);
- a 5 top cm with clean sand and silty material cover minimizing evaporation and maintaining surface integrity and electrode soil connection.

The main filling material consisted of 100 kg of medium to coarse sand (Fig. 3.1.a) a primary grain-size range between 200 and 1000 µm, and a modal peak around 800–900 µm (0.8–0.9 mm**)**. This classification corresponds to a medium–coarse sand according to the USGS scale. The sand was combined with 50 kg of rounded gravel (7–14 mm fraction). The granulometric distribution indicates a uniform structure with minimal silt and clay fractions (<3%), ensuring homogeneous electrical and hydraulic properties.

Hydric boundary conditions. The tank was operated with a stable water table located approximately 20 cm above the bottom. The contaminated volume was therefore positioned within the unsaturated zone, but under continuous capillary influence from the underlying saturated layer. After the initial filling and sealing of the system with plastic foil, no additional water was supplied. Relative humidity inside the tank was continuously monitored and remained close to 100% throughout the entire monitoring period, ensuring hydric stability and preventing progressive drying of the porous medium. Although volumetric water content was not directly measured, the combination of a stable water table, persistent high relative humidity, and sealed boundary conditions suggests that moisture conditions remained effectively constant during the experiment.

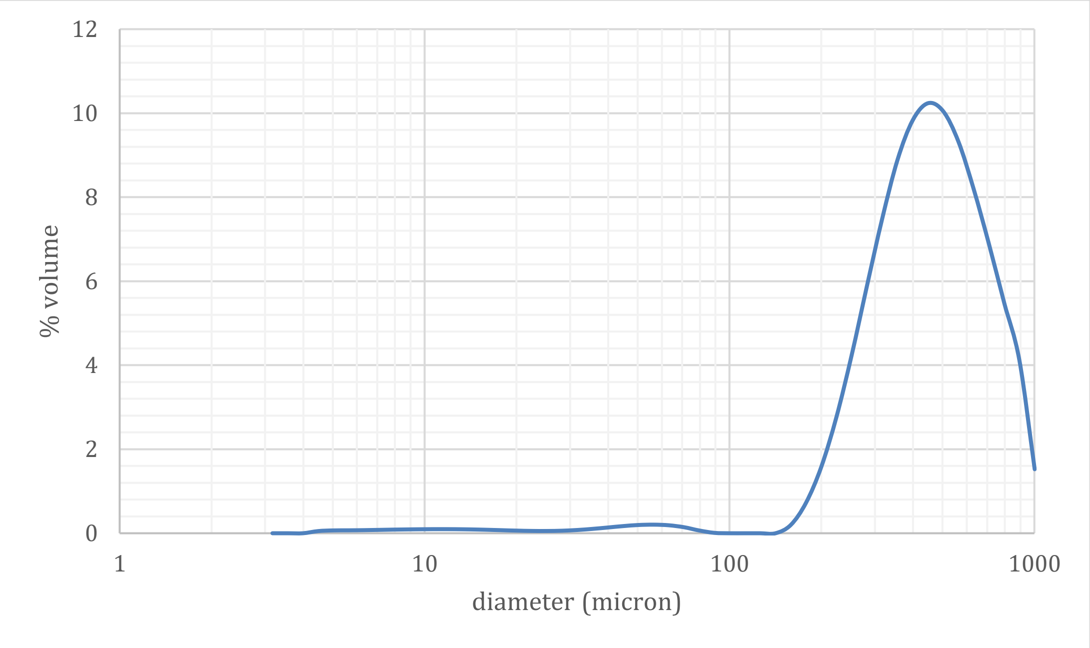

Figure 3.1.a – *Grain size distribution and of the sandy matrix used for the contaminated tank experiment. Modified from original laboratory documentation (2024).*

3.1.1 Contaminated volume preparation

The contaminated volume was created using the same base material as the surrounding matrix, consisting primarily of fine to medium sand (0.062–1 mm) with a minor gravel fraction (<5%, 7–14 mm) according to the USGS grain-size classification. The low gravel content ensured a homogeneous structure with pore sizes representative of a typical sandy aquifer, while maintaining similar hydraulic and electrical properties to the bulk medium.

The sterile sand–gravel mixture (1.25 kg total) was carefully impregnated with 200–250 mL of commercial diesel fuel**.** Given the measured dimensions (15 × 8 × 4 cm) and total matrix mass (1.25 kg), the diesel used corresponded to an estimated hydrocarbon concentration of approximately 100 000–150 000 ppm relative to the total mass of the contaminated block. The mixture was homogenized to ensure uniform hydrocarbon distribution and then placed under a fume hood for 48 hours to allow volatilization of light fractions, leaving mainly heavy hydrocarbons (C > 12). This approach simulated a mature, weathered contamination and avoided artefacts caused by vapor-phase hydrocarbons.

After preparation, the contaminated block (≈ 0.48 L) was buried at a depth of –14 cm, centered (Fig. 3.1.b) within the tank between the borehole electrodes and directly beneath the bacterial injection tubes. This defined a precisely located pollution source representing approximately 0**.**33% of the total tank volume, serving as the target zone for resistivity and biogeochemical monitoring.

Figure 3.1.b – *Position of the contaminated volume within the tank*

After preparation, the contaminated material was left under an extraction hood for 24 hours to allow partial volatilization and oxygen equilibrium before burial within the tank. The tank was sealed and allowed to age naturally for one year, from 24 June 2024 (production of the contaminated volume) to 7 July 2025 (beginning of electrical monitoring). During this time, no further interventions were made, reproducing the chemical and biological aging typical of legacy diesel contamination.

3.2 Electrode design and construction

The electrode system consisted of 84 stainless-steel electrodes fabricated in two distinct types:

- Surface electrodes: 1.8 mm stainless-steel rods with an active surface of 1.5 cm, used to measure near-surface variations and lateral gradients.
- Borehole electrodes: made of two turns of insulated stainless-steel cable, ensuring stability and electrical continuity in depth.

And in particular, each electrode was labelled sequentially:

- 1–20**:** borehole electrodes (4 borehole with 5 electrodes each),
- 21–24: external surface electrodes (outside the grid),
- 25–84**:** main surface array electrodes within the 4 × 4 cm grid.

Each electrode connection was individually tested with an electronic tester before every acquisition to confirm full continuity from connector to tip. The cable–electrode junction was isolated to prevent short-circuits, while the metal contact was left exposed to ensure direct coupling with the soil.

Electrodes were symmetrically distributed along both X and Y central axes. To guarantee positional precision, a **2** mm plexiglass support grid with 90 pre-drilled holes (4 × 4 cm spacing**)** was installed during the setup phase. This rigid geometry minimized displacement during compaction or saturation cycles.

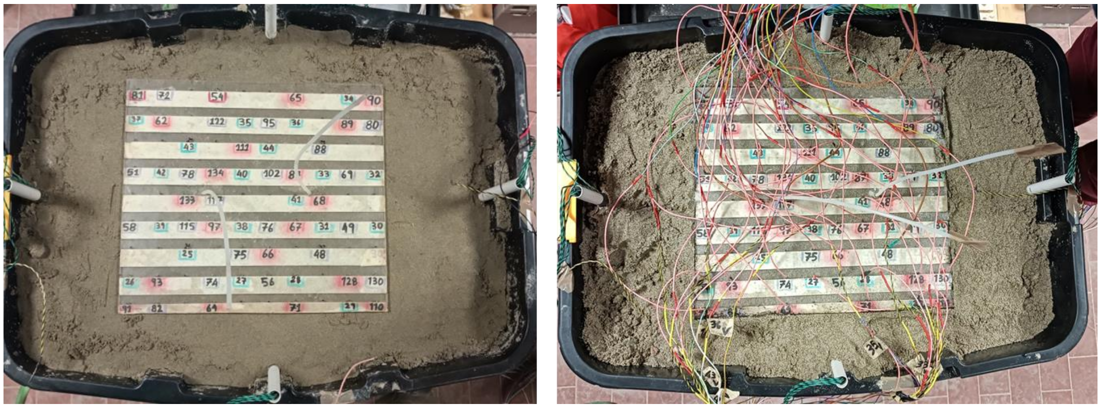

Figure 3.2.a – *Plexiglass electrodes support with injection tube left, right during electrodes setup.*

3.2.1 Electrodes array position reconstruction

At the end of the monitoring campaign, a laser-scan 3D calibration was performed to verify electrode geometry and detect possible deformations of the tank structure caused by prolonged mechanical and hydrological stress. The scan revealed slight wall deformations (Fig 3.2.b), and actual electrode coordinates were reconstructed accordingly before data inversion.

This precise reconstruction ensured consistency between the physical setup and the digital mesh employed in the inversion workflow, minimizing geometric artefacts.

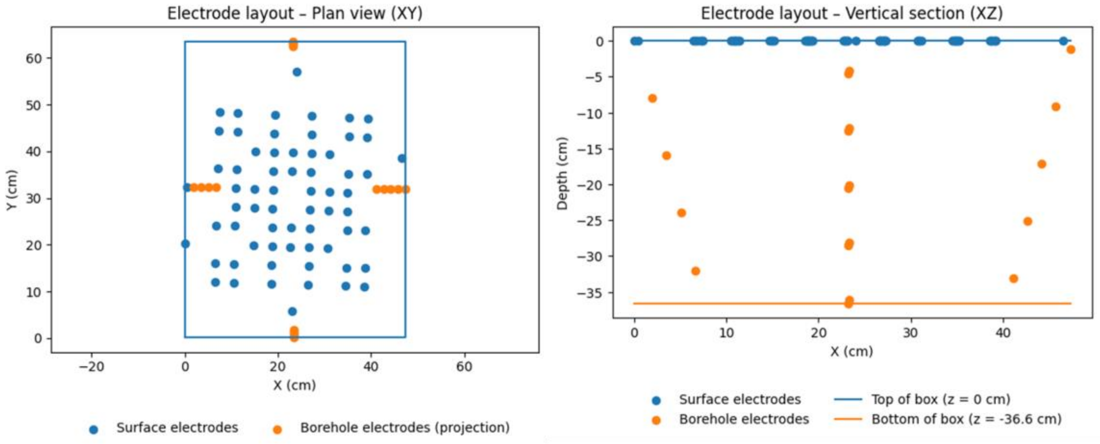

Figure 3.2.b – *Electrode configuration and spatial positioning accuracy inside the experimental tank (spacing 4 cm in surface, 8 cm in vertical; four vertical electrode lines).*

3.3 Data acquisition and custom sequence

The ERT measurements were collected with a Syscal Pro system. A custom measurement sequence was generated using a Python script specifically designed to optimize quadrupole selection and spatial coverage near the contaminated zone. The approach followed the theoretical guidelines of (Loke, 2014), (Binley & Kemna, 2005), and (Wilkinson et al., 2012), focusing on numerical stability, target of investigation, and data balance.

Measurements were run in automatic sequencing mode, with the instrument controlling electrode addressing and repeating each datum according to predefined quality constraints (*stacking* and *standard-deviation* criteria).

The transmitter current ON-time (pulse duration) was set to 0.25 s, a value within the standard Syscal options (0.2–8 s). Longer ON-times increase the injected charge per cycle and typically improve signal-to-noise at the cost of longer cycle times.

Stacking limits were minimum = 3, maximum = 6, meaning each measurement was repeated at least three times and up to six times adaptively, stopping early if the quality threshold was met.

The requested output voltage V_{AB} was 24 V, corresponding to constant-voltage control between current electrodes A–B. Consequently, the transmitted current was automatically adjusted to the contact resistance according to the fundamental relation:

$$I = V / R$$

where I is the injected current, V the applied voltage (24 V), and R the measured contact resistance. This configuration ensured consistent data quality and minimized variability across measurement cycles.

To maximize acquisition throughput, reciprocal measurements were not included in the sequence. Given the controlled laboratory conditions and the large number of measurements acquired per time step (18,921 measurements in approximately 2 h 30 min), including reciprocal measurements would have resulted in quasi-continuous acquisition. Priority was therefore given to maximizing spatial and temporal data density.

Data quality was controlled through stacking statistics, with measurements exhibiting an internal standard deviation greater than 0.5% being automatically rejected during acquisition, and through post-inversion residual analysis (see Chapter 5).

3.3.1 Sequence generation principles

Resistivity measurements are inherently ill-posed inverse problems, governed by non-linear relationships between potential differences and resistivity distributions. Therefore, survey design must balance resolution and stability (Menke, 2012). The optimization framework adopted in this study combines the model resolution matrix approach (Wilkinson et al., 2012) with error-aware measurement weighting (Binley, 2015). The model resolution matrix

$$R = (G^{T}G + C)^{-1} G^{T}G$$

quantifies how well each model cell is constrained by the data, where:

- G = Jacobian matrix (sensitivity matrix)
- C = constraint matrix imposing damping and smoothness

The optimization maximizes the mean model resolution while penalizing high-sensitivity clusters that could lead to overfitting or unstable inversions voxel-based weighting system to assess geometric representativeness of quadrupole configurations. The workflow follows three main phases, consistent with the structure of Wilkinson et al. (2012) and Binley (2015):

  - Pre-computation Phase: all potential current and potential dipole combinations are evaluated based on geometric feasibility (e.g., maximum AB and MN lengths ≤ 50 cm). Invalid configurations are excluded early to reduce computational load.

- Voxel Classification: the domain is discretized into a 3D voxel grid (20–60 cm × 10–44 cm × −20 to −5 cm). Each quadrupole is assigned to a voxel index using barycentric coordinates, and voxel density counters are incremented accordingly. Configurations are weighted based on their location relative to a *target region* (centered at x=40, y=26, z=−12 cm), an *expanded region* for near-target sensitivity, and peripheral or deep zones.
- Sequence Assembly and Balancing: valid quadrupoles are categorized into “target,” “deep,” “peripheral,” and “balanced” subsets. Weighted random selection ensures that approximately 5500 quadrupoles are retained, with a minimum of 2200 targeting the central region. This ensures consistent spatial coverage while maintaining computational tractability for inversion.

Each step incorporates literature-based constraints: voxel weighting thresholds and angular filters (Menke, 2012), density balancing (Wilkinson et al., 2012), and statistical noise modelling (Binley, 2015). The final selection process ensures compliance with Electre Pro+ specifications, using shuffled randomized ordering to avoid sequential electrode polarization (Wilkinson et al., 2012; Dahlin, 2000)

3.3.2 Numerical and physical justification

Following (Oldenburg & Li, 1999*)* and (Binley, 2015), the procedure ensures an adequate balance between near-surface and deeper sensitivities, minimizing potential numerical artefacts during inversion. By constraining electrode spacing and ensuring randomization within acceptable geometrical limits, the algorithm reduces spatial bias while maintaining full numerical compatibility with the Electre Pro+ acquisition system. Fig. 3.3.a show the development process used to create the custom sequence adopted in this work.

Each complete measurement cycle included 18921 measurements, subdivided into three cycles of 5997 measurements each (using electrodes 1–44 with 3 different cable), plus an additional 930 measurements employing electrodes 1–24 over 54 time steps across 73 days.

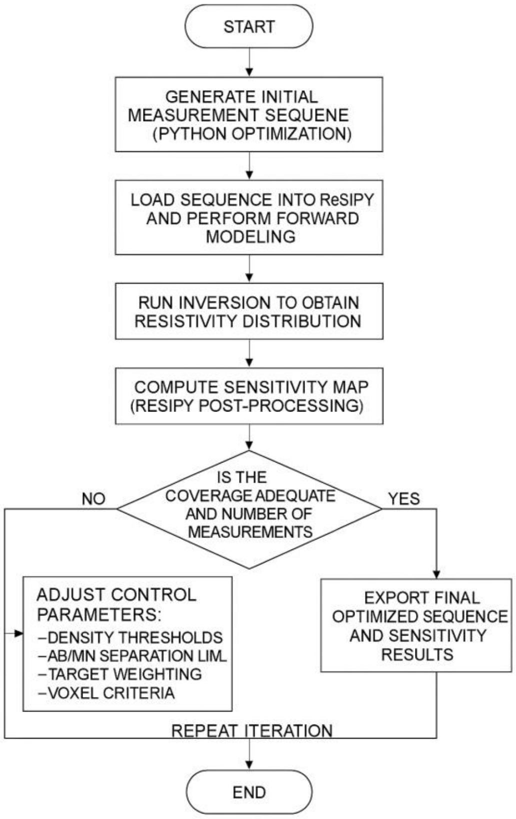

Figure 3.3.a – *Iterative control flow for ERT sequence optimization through forward modelling, inversion, and sensitivity balancing using ResIPy.*

Electrode polarization is a common issue when metallic electrodes are reused for potential measurement soon after current injection (Dahlin, 2000). To minimize this effect, a simulated annealing reordering routine was applied to maximize time separation between current and potential reuses.

The optimization cost function was defined as:

$$\boldsymbol{c} = \boldsymbol{\Sigma} \left(\frac{\mathbf{1}}{\boldsymbol{d}_{\mathrm{i}}}\right)$$

where d_i represents the number of configurations between a current injection and the next potential measurement using the same electrode.

Minimizing c ensures that polarization decay times (>10 s) are respected, thereby reducing systematic voltage drift and ensuring reproducible data.

Following the recommendations of Binley (2015), the error model was implemented as a linear mixed-effects function, combining proportional and electrode-group-dependent noise components:

$$\boldsymbol{\sigma}_{\mathrm{i}} = \boldsymbol{a} + \boldsymbol{b}\,|\boldsymbol{R}_{\mathrm{i}}| + \boldsymbol{\varepsilon}_{\mathrm{e}}(_{\mathrm{i}})$$

where:

- σ_i = standard deviation of the i-th measurement
- R_i = measured transfer resistance
- a, b = empirical constants derived from calibration
- $\varepsilon_e(_i)$ = electrode-specific variance term

This formulation captures electrode-specific noise patterns more effectively than a simple uniform linear model.

The final sequence provides dense coverage in the target zone and improved uncertainty propagation characteristics in inversion workflows, consistent with Oldenburg & Li (1999).

3.4 Measurement cycles and full acquisition scheme

The complete acquisition scheme consisted of four independent measurement sequences designed to ensure both spatial coverage and temporal continuity over the monitoring period.

The first sequence included 930 quadrupole measurements, acquired exclusively using electrodes 1–24, corresponding to the borehole array positioned along the central Y-X axis of the tank. This configuration targeted the vertical resistivity gradients and allowed high-resolution monitoring of the contaminated core through depth, as illustrated in the Fig. 3.4.a right hand panel.

Subsequently, three extended cycles of 5997 quadrupole measurements each were executed using electrodes 1–44. These measurements employed three separate cables, enabling the use of all available electrodes (45-84) within both the surface and borehole networks. This design maximized spatial sampling of the resistivity field and improved the inversion stability by providing overlapping current–potential configurations with distinct geometric factors (Fig. 3.4.a left hand panel).

In total, 18,921 measurements were collected, distributed across the three large cycles (5997 × 3) and the 930-borehole-only sequence, recorded over 73 days with 54 temporal acquisitions. This sequence structure ensured robust sensitivity to both lateral and vertical resistivity changes, while allowing time-lapse comparison across identical quadrupole sets.

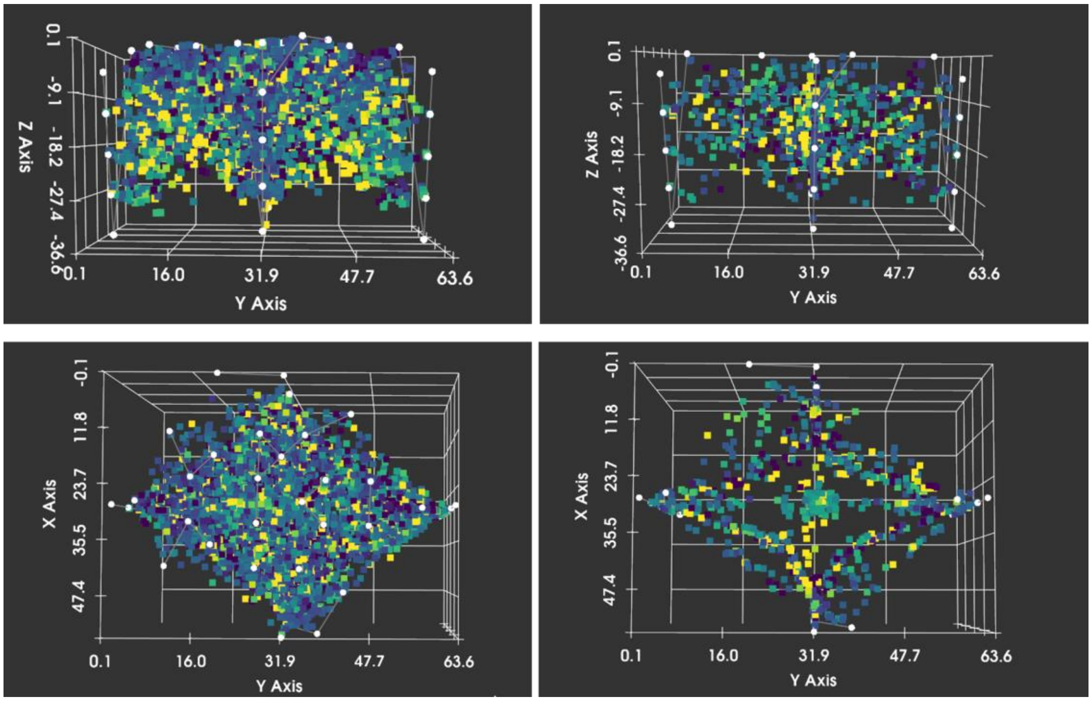

Figure 3.4.a – *Pseudosection and distribution of measure points, left the sequence 5997 measure with borehole and surface (electrode 1-44), right sequence only borehole (electrodes 1-24) 930 measure; Top – front view; bottom – top view.*

3.5 Mesh construction and model discretization

The three-dimensional computational domain was generated in Gmsh (version 4.13.1) to accurately reproduce the geometry of the experimental tank and the electrode layout described in Chapter 3. The mesh incorporated both the 3° internal slope of the tank base and the slight wall curvature observed in the post-experiment 3D laser scan, ensuring geometric consistency between the physical and numerical models used in the inversion.

To balance computational efficiency with inversion accuracy, a non-uniform tetrahedral discretization was implemented according to the following criteria:

- Surface refinement – element size ≈ 2 cm in proximity to surface electrodes;
- Intermediate layer refinement – element size ≈ 4 cm between the surface electrode plane and the buried contaminated volume;
- Bulk domain discretization – element size gradually increasing to ≈ 8 cm toward the tank boundaries;
- Localized densification around the borehole electrodes (IDs 1–20) and the contaminated zone centered at $z = -14$ cm, where higher resistivity gradients were expected.

Each electrode was included as a nodal constraint, uniquely indexed according to its identifier in the field acquisition files. This ensured direct one-to-one correspondence between the physical electrode network and the numerical model.

Mesh quality was validated using the Gmsh element-quality metric, achieving a minimum tetrahedral quality of 0.72, which satisfies standard inversion stability thresholds (Clement & Moreau, 2016).

The final mesh contained 47,812 tetrahedral elements and 9,605 nodes, exported in both: .msh (native Gmsh) and .vtk (visualization) formats for direct import into ResIPy. This discretization provided an optimal trade-off between numerical accuracy and computation time, preserving fine-scale resolution near the contaminated block while maintaining model smoothness in peripheral regions.

The volumetric geometry accurately reproduced the experimental configuration, thereby minimizing potential geometric artefacts during inversion and ensuring a physically meaningful spatial distribution of resistivity values.

The same mesh was employed consistently for both synthetic forward modelling and experimental inversions, ensuring direct comparability between sensitivity analyses and inversion results and minimizing discretization-related biases.

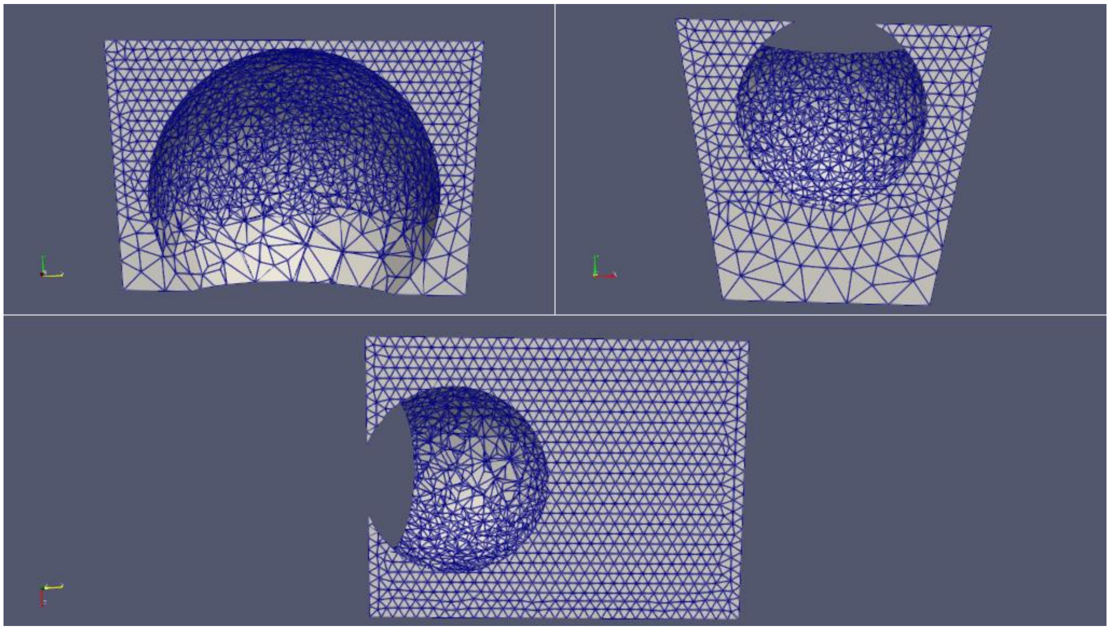

Figure 3.5.a *– Sphere-clipped 3D view of the experimental mesh: top left – side view; top right – front view; bottom – top view (constructed in Gmsh).*

3.6 ResIPy software for electrical data inversion

The inversion and data processing were carried out using ResIPy (Blanchy et al., 2020), an open-source Python-based graphical user interface (GUI) for electrical resistivity tomography (ERT). The software employs the R3t computational core (Binley, 2015), originally developed at Lancaster University, which performs three-dimensional finite-element inversion with smoothness-constrained regularization.

ResIPy provides an efficient link between field data and inversion modelling by integrating preprocessing tools, synthetic model generation, and inversion monitoring in real time. The program is compatible with several data acquisition formats, including Syscal Pro, ensuring direct import and geometric configuration consistency.

3.6.1 ResIPy software environment

ResIPy (Blanchy et al., 2020) is an open-source Python-based software package designed for the inversion and modelling of Electrical Resistivity Tomography (ERT) and Induced Polarization (IP) data. It provides both a graphical user interface (GUI) and a Python API, allowing flexible interaction for users ranging from field operators to advanced researchers. ResIPy integrates and extends the R2/cR2/R3t inversion codes developed by A. Binley at Lancaster University (Binley, 2015), which are widely recognized in hydrogeophysics for their stability and computational efficiency.

The software architecture is organized into three hierarchical layers:

- Computation layer – includes the compiled inversion codes R2, cR2, and R3t for two-dimensional, complex IP, and three-dimensional problems, respectively. These codes solve the forward and inverse problems using the finite element method (FEM) to simulate electrical potential fields in complex geometries.
- Intermediate API layer – acts as a Python wrapper that manages data I/O, mesh generation, model parameter definition, and inversion control. It provides an efficient bridge between user operations and the compiled numerical engines.
- Graphical user interface (GUI) – allows direct import of raw data (e.g., from Syscal Pro), configuration of electrode arrays, creation of computational meshes, and visualization of inversion results through pseudo sections, 3D renderings, and sensitivity maps.

ResIPy supports both forward modelling—for survey design and sensitivity testing—and inversion—for resistivity reconstruction of subsurface structures. Mesh generation is handled via the Gmsh engine (Geuzaine & Remacle, 2009), which automatically refines the grid in regions of high potential gradient, improving the accuracy of the FEM solution.

The interface also enables batch execution of inversion runs, sensitivity testing, and uncertainty estimation. Each inversion can be configured through a flexible parameter file that defines mesh resolution, damping factors, and convergence criteria.

3.6.2 The R3t computational core

The R3t core solves the forward problem for steady-state electrical conduction using the governing partial differential equation:

$$\nabla \cdot (\sigma \nabla V) = 0$$

where:

σ = electrical conductivity (S/m)
V = electric potential (V)

The measured apparent resistivity is derived from Ohm's law as:

$$\rho_a = k \times (\Delta V / I)$$

where:

ρ_a = apparent resistivity ($\Omega \cdot$m)
k = geometric factor (m)
ΔV = potential difference (V)
I = injected current (A)

The inversion problem aims to determine the subsurface resistivity model m that best reproduces the observed data d by minimizing an objective function composed of data misfit and model roughness terms:

$$\Phi = ||W_d\,(d_{obs} - f(m))||^2 + \lambda^2\,||W_m\,(m - m_0)||^2$$

where:

Φ = total objective function
d_{obs} = observed data vector
f(m) = predicted data vector
λ = regularization (smoothing) parameter
W_d = data weighting matrix
W_m = model weighting matrix
m_0 = reference (initial) model

The model is iteratively updated according to the smoothness-constrained least-squares scheme:

$$m_{i+1} = m_i + (J^T J + \lambda^2 W^T W)^{-1} J^T (d - f(m_i))$$

where:

J = Jacobian (sensitivity) matrix
W = spatial smoothing matrix

This Occam-type inversion balances data fit and model smoothness, minimizing non-physical oscillations in the recovered resistivity field. The R3t implementation is fully three-dimensional and allows for irregular topography, non-rectangular boundaries, and hybrid surface-borehole electrode configurations, making it suitable for controlled laboratory experiments and field-scale surveys alike.

ResIPy exports results in standard VTK and TXT formats for post-processing and visualization in ParaView, Python, or GIS platforms.

3.7 Environmental monitoring (HOBO sensor)

Continuous monitoring of temperature and relative humidity was achieved using HOBO U23 Pro v2 sensors, placed on the surface within the tank (Fig. 3.7.a).

- **Sampling interval:** every 1 hour.
- **Temperature range recorded:** 20-24°C, with an average of 22 ± 2 °C.
- **Relative humidity:** typically, 100%, indicating no evaporation loss.

Temperature data were used to evaluate thermal drift and to guide correction of resistivity values. Environmental parameters remained stable throughout the campaign, confirming consistent hydrothermal conditions.

Figure 3.7.a – *Location of HOBO sensors for environmental monitoring and corresponding temperature trends. Modified from experimental data (2025).*

The environmental dataset provided the baseline for temperature normalization, ensuring that resistivity variations could be attributed primarily to biogeochemical activity rather than thermal artefacts (Abdulkadir et al., 2019; Teng et al., 2023; Hayley et al., 2010).

4 Microbial and Molecular Analyses

4.1 Microbial inoculation and injection tubes

Two microbial strains—*Rhodococcus erythropolis* and *Escherichia coli*—were used to assess the detectability of biologically induced resistivity variations. The inoculation system consisted of two independent sterilized PVC tubes (internal diameter 2 mm). The tubes were placed during the filling of the tank, positioned on the surface of the contaminated volume to inoculate directly on the polluted volume the solution containing the two bacterial strain.

Both tubes were installed along the same Y-axis, ensuring symmetrical conditions across the contaminated volume:

Tube 1 (*Rhodococcus erythropolis*): positioned between electrodes 45 and 77, representing the "active" inoculation side.

Tube 2 (*Escherichia coli*): positioned between electrodes 41 and 56, representing the "inactive" control side.

This configuration was designed to verify whether, by inoculating the two bacteria on opposite sides of the contaminated core, it was possible to observe an electrical signature corresponding to the expected metabolic activity of *Rhodococcus* and the inactivity of *E. coli*, the latter being intolerant to high hydrocarbon concentrations and lacking hydrocarbon-degrading enzymes.

4.2 Microbial Characteristics

Two bacterial strains were selected to evaluate the electrical response associated with hydrocarbon microbially mediated transformation (MMT) and to isolate biogenic from abiotic electrical effects.

Rhodococcus erythropolis is a Gram-positive, non-sporulating, hydrocarbon-oxidizing bacterium known for producing surface-active compounds that facilitate the solubilization of hydrophobic substrates. It exhibits high tolerance to organic solvents, heavy metals, and osmotic stress, and can grow over a broad temperature range (5–40 °C). These characteristics make it a model organism for studying bioremediation under harsh environmental conditions (de Carvalho & da Fonseca, 2005; Pacheco et al., 2010; de Carvalho, 2005).

Escherichia coli, a Gram-negative facultative aerobe, was used as a non-degrading control. While it does not metabolize hydrocarbons, it provides insight into the purely physical–electrical responses of a non-hydrocarbon-degrading microbial population in a contaminated environment (Madigan et al., 2018).

The choice of these contrasting strains allowed the experiment to decouple the electrical effects associated with biological degradation from those due to ionic or structural changes in the medium.

4.3 Culture Preparation and Handling Protocol

To evaluate the specific effects of microbial activity on hydrocarbon degradation, two bacterial strains were selected and inoculated separately: *Rhodococcus erythropolis*, a hydrocarbon-degrading actinobacterium capable of metabolizing long-chain alkanes, and *Escherichia coli*, a non-degrading model organism used as a biological control.

The comparative behaviour of these strains allowed assessing both biotic and abiotic contributions to the electrical and chemical evolution within the contaminated volume.

Materials Media components: Distilled water, LD broth, M9 10X medium (all autoclaved after preparation). Sterilized flasks, gloves, ethanol (70%), sterile loops, pipettes and filter tips.

Equipment Laminar flow hood, rotary shaker, incubator, autoclave, UV/visible spectrometer.

Cultivation in Liquid Media Liquid media are nutrient solutions that support the growth of microorganisms in suspension, providing homogeneous access to nutrients and oxygen. This environment promotes faster growth and stable metabolic activity. Step 1: Preparation of Medium Prepare LD broth following standard proportions: 3 g tryptone (1%), 2 g yeast extract (0.5%), and 2 g NaCl (0.5%) in 400 ml of distilled water. Prepare M9 10X medium with 28 g Na_2HPO_4, 12 g KH_2PO_4, 2 g NaCl, and 4 g NH_4Cl in 400 ml. Autoclave both media and distilled water for sterilization.

Step 2: Inoculation Work under a laminar flow sterile hood. Using a 25 ml pipette, transfer LD broth into sterile flasks (approximately one-fifth of the flask volume, e.g., 50 ml LD broth in a 250 ml flask). For each strain, collect a fresh colony (<3 months old) from a Petri dish using a sterile loop and inoculate the liquid medium by gently swirling.

Step 3: Incubation Incubate inoculated flasks on a rotary shaker at the appropriate temperature: 37 °C for *Escherichia coli* and 30 °C for *Rhodococcus erythropolis*. After 24 h, assess the turbidity of the medium. If sufficient growth is observed, proceed to washing.

Step 4: Cell Washing Divide the culture suspension into 50 ml sterile Falcon tubes. Centrifuge for 15 min at 4000×g. Discard the supernatant and resuspend the pellet in 2–5 ml of M9 1:50 (depending on pellet size). Repeat centrifugation and washing twice more under the same conditions. Measure OD_{600} (optical density at 600 nm) using a

UV/visible spectrometer. For this experiment, the starting inoculum must have OD_{600} = 0.1. If higher, dilute with M9 1:50 to reach the target OD_{600}.

This standardized preparation ensures reproducible bacterial inoculation for the bioremediation experiment described in the following sections.

Bacterial inoculation was carried out using liquid cultures of Rhodococcus erythropolis and Escherichia coli prepared under sterile laboratory conditions. For each strain, a volume of 50 mL of actively growing culture was injected into the sandbox system through the dedicated injection lines.

On this basis, and considering the observed growth behaviour of both strains, the inoculated biomass is conservatively estimated to be on the order of 10^7–10^8 cells per milliliter. This estimate is intentionally expressed as an order of magnitude only. It is provided to document the experimental conditions and the scale of biological input, and it is not used for quantitative coupling with the geophysical response. The experimental design does not aim to establish a direct proportional relationship between inoculated biomass and electrical signal, but rather to investigate the emergence of electrical variability under controlled and extreme environmental conditions.

4.4 Sampling Procedure

Sampling was carried out on 24 September 2025, immediately following the completion of the 73-day acquisition phase, to evaluate the distribution and persistence of microbial activity within the contaminated core. The position of the samples is shown in Fig. 4.4.a. Three cylindrical plexiglass corers (length 9 cm, diameter 2.8 cm) equipped with conical stainless-steel shoes were used to extract undisturbed soil cores from the contaminated layer. Before coring, the soil immediately below the electrode plate was carefully removed, while leaving approximately 2 cm of uncontaminated sand above the contaminated volume. This procedure was adopted to preserve an undisturbed matrix during coring and to minimize disturbance of the biological material.

Sampling was performed under sterile laboratory conditions, using 70% ethanol for sterilization and sterile gloves to avoid cross-contamination. Each sample was labelled with its depth, position, and inoculated bacterial strain.

Two sampling points were located directly below the bacterial injection lines:

- *Rhodococcus erythropolis* zone (active microbially mediated transformation MMT) left side
- *Escherichia coli* zone (inactive control side, right side).

and an additional blank control sample was collected from uncontaminated soil near electrode wells 6–10.

Cores were immediately sealed in sterile polyethylene bags and transported to the microbiology laboratory for subsampling.

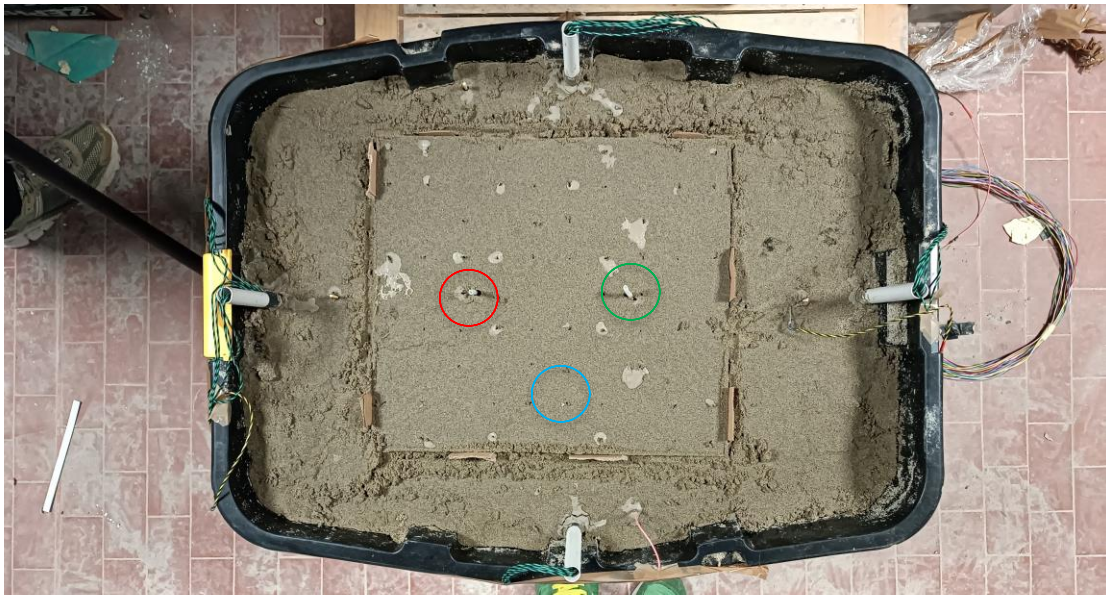

Figure 4.4.a – *Sampling positions beneath bacterial injection lines and electrode array. Red circle R.erythropolis, green circle E.coli and blue circle blank sample.*

Under a laminar flow hood, each plexiglass core was carefully extracted from the sampler and longitudinally opened. For the Rhodococcus erythropolis core, three subsamples were collected corresponding to the upper (top), central (middle), and lower (bottom) portions of the contaminated interval. For the Escherichia coli core, two subsamples were collected from the upper (top) and central portions, reflecting the reduced vertical extent of the colonized zone. The blank control core was homogenized by combining material from the upper, middle, and lower portions into a single composite sample. This procedure resulted in a total of six biological samples used for downstream molecular analyses.

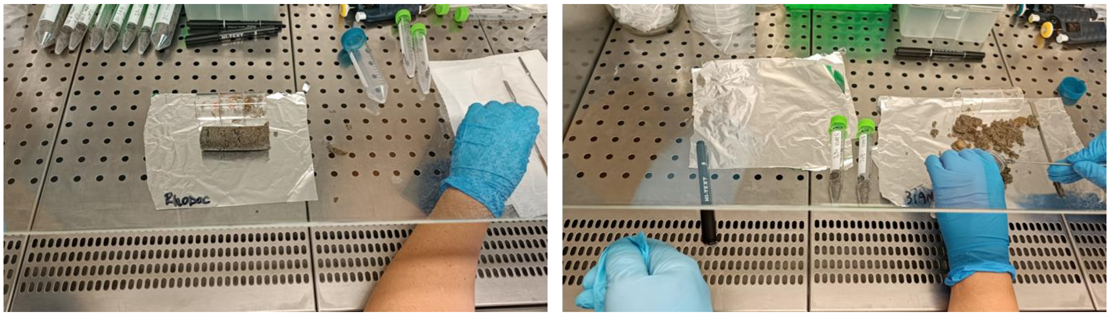

Figure 4.4.b – *Preparation of biological aliquots under laminar flow hood. Plexiglass cores were longitudinally opened and subsampled to obtain upper (top), central (middle), and lower (bottom) portions of the contaminated interval. Subsamples were transferred into sterile containers for subsequent molecular analyses.*

Summary of the samples and relative aliquot are presented in the table below:

Table 4.5.a – *Summary of collected samples and characteristics.*

Sample ID	Sampling Zone	Depth Interval (cm)	Inoculated Strain	Aliquot Section	Laboratory Code	Notes
BLK	Uncontaminated zone	-10/-19	None	Whole core	BLK-01	Sterile blank sample

COL1	Eastern (E. coli)	-10/-19	*E. coli*	Upper	EC-01	under injection tube 2
COL2	Eastern (E. coli)	-10/-19	*E. coli*	Middle	EC-02	Mid-depth
RHO1	Western (Rhodococcus)	-10/-19	*R. erythropolis*	Upper	RH-01	under injection tube 1
RHO2	Western (Rhodococcus)	3–6	*R. erythropolis*	Middle	RH-02	Mid-layer of contaminated core
RHO3	Western (Rhodococcus)	6–9	*R. erythropolis*	Lower	RH-03	Deep portion

4.5 DNA Sequencing – Illumina MiSeq Platform

The sequencing of bacterial DNA was performed using the Illumina MiSeq™ System (Illumina Inc., USA) (Fig. 4.6.a), a benchtop next-generation sequencing (NGS) platform based on sequencing-by-synthesis (SBS) chemistry. This system integrates cluster generation, sequencing, and base-calling into a single automated workflow, ensuring high accuracy and reproducibility for small-genome and amplicon studies.

Samples were sequenced using the MiSeq Reagent Kit v3 (600-cycle, 2 × 300 bp) configuration, providing up to 15 Gb of output and over 70% of bases above Q30 quality score (Illumina, 2021).

The Illumina SBS chemistry employs reversible terminator nucleotides, allowing detection of each incorporated base by fluorescent imaging at every cycle. This ensures high accuracy even across homopolymeric regions (Bentley et al., 2008).

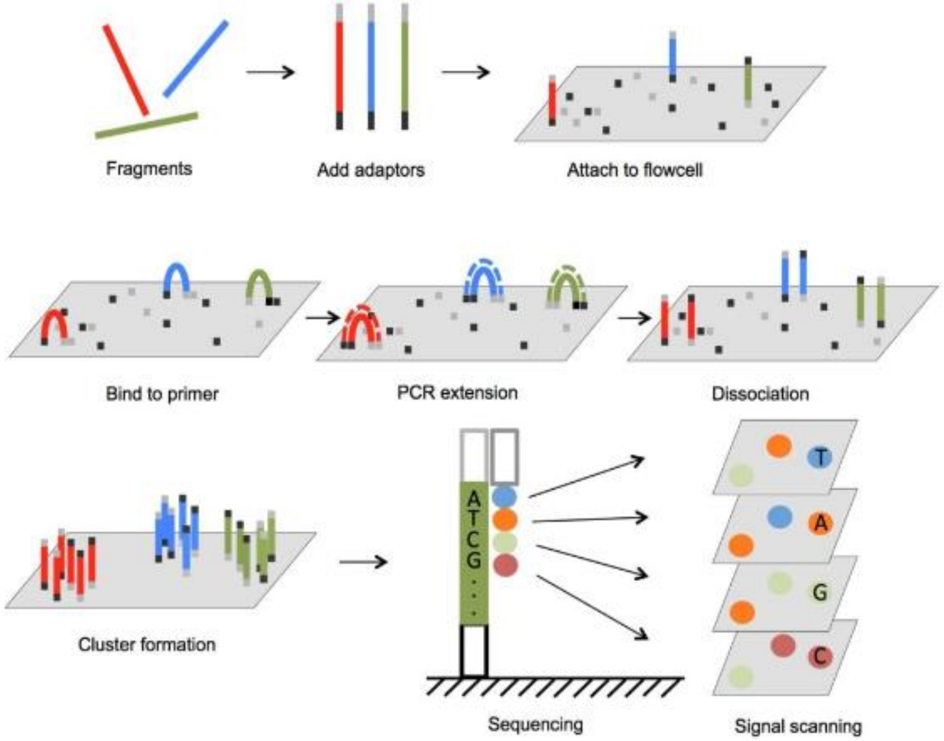

Figure 4.6.a – *Illumina MiSeq sequencing-by-synthesis (SBS) workflow (Illumina, 2021).*

Taxonomic assignment was performed using:

- SILVA rRNA gene database (v138**)** – to remove non-bacterial sequences, chloroplasts, and mitochondria.
- RDP classifier – for finer bacterial taxonomic classification.

The final ASV table was normalized and used to assess bacterial community diversity across samples. Relative abundance plots and taxonomic bar charts were produced to visualize bacterial composition.

4.6 Sequence Analysis

The sequencing output was obtained in FASTQ format, where each sample produced two paired-end reads: R1 (Forward**)** and R2 (Reverse). Each FASTQ entry consists of four lines:

- a header line beginning with **@**, followed by the sample name,
- the nucleotide sequence,
- a **+** separator, and
- a quality score string, which encodes the probability of a base call error.

Raw reads were processed using the DADA2 pipeline (Callahan et al., 2016), which performs quality filtering, dereplication, merging, and chimera removal. Low-quality reads were discarded, and sequences were trimmed to 180 bp (R1) and 150 bp (R2) before merging. Overlapping pairs were aligned, and those with imperfect overlap were eliminated.

High-quality merged reads were then clustered into Amplicon Sequence Variants (ASVs**)**, where each ASV represents a unique biological sequence differing by at least one base. PCR chimeras and singletons (ASVs occurring only once in the entire dataset) were removed to reduce artefacts.

A feature table was constructed showing the frequency of each ASV per sample. ASV sequences were taxonomically classified using the SILVA and RDP databases. The SILVA database was first used to filter out non-bacterial sequences (e.g., chloroplasts and mitochondria), as it provides reliable annotation of organelle DNA, followed by RDP classification for finer taxonomic resolution.

From the resulting dataset, relative abundance histograms were generated to visualize the bacterial community composition across samples and depths.

5 Results

The monitoring campaign produced a large ERT dataset (54 repeated acquisitions, each including 18,921 quadrupole measurements). To ensure interpretability while keeping the inversion workflow computationally tractable, results are presented using a two-level strategy. First, the full dataset is analyzed statistically in terms of apparent resistivity variations ($\Delta\rho_a$) to identify global trends, transient events, and changes in variability through time. Second, spatial interpretation is supported by 3D inversions computed on a subset of 12 representative time steps spanning the key experimental phases. These selected time steps were processed using both independent inversions and a time-lapse inversion constrained to a common reference model. The agreement between the two inversion approaches is used as an internal consistency check to strengthen the robustness of the interpreted electrical patterns.

5.1 Statistical and multivariate analysis of apparent resistivity variations

This section presents the results of the 73-day Electrical Resistivity Tomography (ERT) monitoring, conducted between **7** July 2025 (T_{00}) and 18 September 2025 (T_{53})**.** The objective is to link apparent resistivity variations ($\Delta\rho_a$) to the biological and ionic processes within the contaminated sandbox system. The analysis combines statistical, temporal, and multivariate tools to interpret the evolution of the system, following the biogeophysical framework described by Atekwana & Slater (2009) and Binley & Slater (2020). The approach enables distinction between global background evolution and localized transient anomalies. The full dataset comprises 54 acquisitions; however, time-lapse inversion of the complete sequence would require several days of computation and more than 7 GB of memory per run. For this reason, a representative subset of time steps was selected based on statistical diagnostics (mean, variance, PCA/RPCA) to preserve the temporal structure of the experiment while maintaining numerical feasibility.

5.1.1 Dataset description and normalization to baseline

Each measurement represents a specific current–potential quadrupole combination (ABMN), measuring the apparent resistivity (ρ_a) of the subsurface volume. To ensure consistency in time-lapse comparisons, all apparent resistivity values were normalized to the initial baseline Day 0 T_{00}, representing the state of the system prior to any biological or chemical perturbation. The bacterial inoculation was performed using a conductive aqueous solution with an electrical conductivity of approximately 335 $\mu S \cdot cm^{-1}$, while the final booster solution exhibited a much higher conductivity (≈ 12 $mS \cdot cm^{-1}$). These contrasts are reflected in the early-time apparent resistivity response discussed in the following sections. The time-lapse variations were expressed both in absolute and in relative form, according to the following relationships:

$$\Delta\rho_{\mathrm{a}}(x_{\mathrm{i}}, t_{\mathrm{j}}) = \rho_{\mathrm{a}}(x_{\mathrm{i}}, t_{\mathrm{j}}) - \rho_{\mathrm{a}}(x_{\mathrm{i}}, T_0)$$

$$\Delta\rho_{\mathrm{a}}, \%(x_{\mathrm{i}}, t_{\mathrm{j}}) = 100 \times \frac{[\rho_{\mathrm{a}}(x_{\mathrm{i}}, t_{\mathrm{j}}) - \rho_{\mathrm{a}}(x_{\mathrm{i}}, T_0)]}{\rho_{\mathrm{a}}(x_{\mathrm{i}}, T_0)}$$

Stacking the apparent resistivity variations for each quadrupole (x_i) over all time steps (t_j) yields a data matrix ($A \in \mathbb{R}^{mxn}$), where (m) is the number of valid quadrupoles and (n = 54) is the number of acquisition times. This configuration preserves the spatial geometry of the sandbox while allowing temporal trends to be analysed statistically.

The chronological sequence of experimental events defines a baseline reference and two main perturbation windows. The baseline reference state corresponds to T_0, acquired before any biological or chemical input. The first perturbation window includes the bacterial inoculation and its immediate electrical transient (T01–T02, first hours). The second perturbation window corresponds to the late-stage saline–nutrient booster injection (T50, followed by post-booster evolution T51–T53). These phases provide a chronological framework for the interpretation of apparent resistivity variations; detailed electrical and process-based interpretations are developed in the following sections.

Table 5.1.a – *Summary of apparent resistivity variations through the monitoring period*

Phase	Time window (steps)	Approx. duration (days)	Experimental control	Purpose within the experiment
Baseline reference	T00	Day 0	System at rest (pre-injection)	Reference state for normalization
Injection transient	T01–T02	Day 0 (first hours)	Bacterial inoculation (conductive solution)	Capture the short-term electrical response to injection
Early post-injection evolution	T03–T10	Day 1–11	Passive evolution (no external forcing)	Transition from physical redistribution to biologically influenced regime
Autonomous evolution	T11–T49	Day 11–58	Microbial and ionic processes (unforced)	Main long-term system response
Booster perturbation	T49–T50	Day 66	Saline–nutrient booster injection	External ionic reinforcement
Late evolution	T51–T53	Day 67–73	Passive re-equilibration	Post-booster adjustment and recovery

5.1.2 Descriptive statistics of apparent resistivity changes

A comprehensive statistical analysis was performed on the normalized apparent resistivity changes ($\Delta\rho_a$) before any inversion or spatial processing. The overall distribution of $\Delta\rho_a$ is strongly non-Gaussian and characterized by a heavy positive tail, as summarized in Table 5.1.b.

Table 5.1.b – *Descriptive statistics of apparent resistivity changes ($\Delta\rho_a$). Statistical parameters summarizing the global variability of apparent resistivity variations during the 73-day monitoring period. Acronyms: μ = mean; σ = standard deviation; IQR = interquartile range; MAD = median absolute deviation; γ_1 = skewness; γ_2 = kurtosis; MMT = microbially mediated transformation; MIER = microbially influenced electrical response.*

Parameter	**Symbol**	**Value**	**Interpretation**
Mean	μ	3.62	Small relative to σ; slight positive bias
Standard deviation	σ	172.5	High dispersion; strong heterogeneity
Coefficient of variation	CV	46.7	Large relative spread relative to the mean
Median	Q_2	79.4	Central tendency robust to outliers
Interquartile range	$IQR = Q_3 - Q_1$	33.7	Scale robust to extreme values
Median absolute deviation	MAD	21.4	Robust measure of dispersion
5th / 95th percentiles	P_5, P_{95}	45.1 / 112.9	Central 90% variability range
Skewness	γ_1	99.7	Dominance of high-magnitude outliers
Kurtosis	γ_2	1.35×10^4	Heavy tails; localized anomalies
Sample size	-	18 921	Valid ABMN after filtering

High skewness (γ_1) and kurtosis (γ_2) indicate that the dataset is dominated by localized high-magnitude anomalies rather than Gaussian noise. The large coefficient of variation (CV = 46.7) confirms strong spatial heterogeneity across quadrupoles, while robust indicators such as the interquartile range (IQR) and MAD highlight the presence of consistent variability beyond outlier influence. The 5th and 95th percentiles define the core range of the dataset, capturing the evolution of both conductive and resistive deviations.

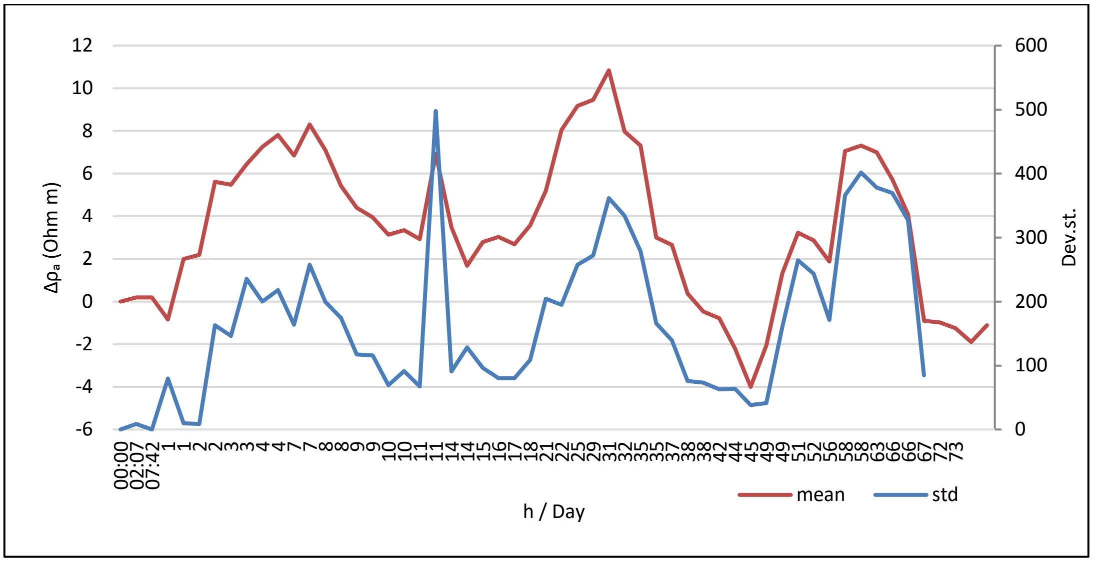

Figure 5.1.a – *Temporal evolution of apparent resistivity variations ($\Delta\rho_a$, Ω·m) and their standard deviation (σ) during the 73-day monitoring period. The mean (red line) indicates the overall conductivity trend, while the standard deviation (blue line) highlights the progressive increase in data variability linked to bio-ionic activation after T02 and booster injection between T49–T50.*

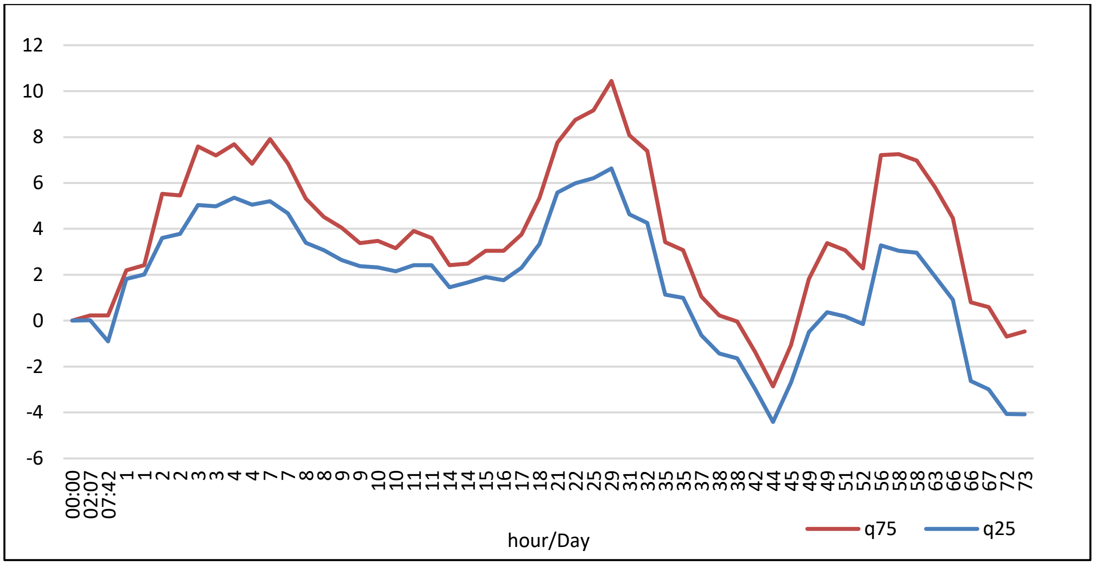

Figure 5.1.b – *Quartiles of $\Delta\rho_a$ variations through time, showing the evolution of the interquartile range (Q25–Q75) and its progressive widening.*

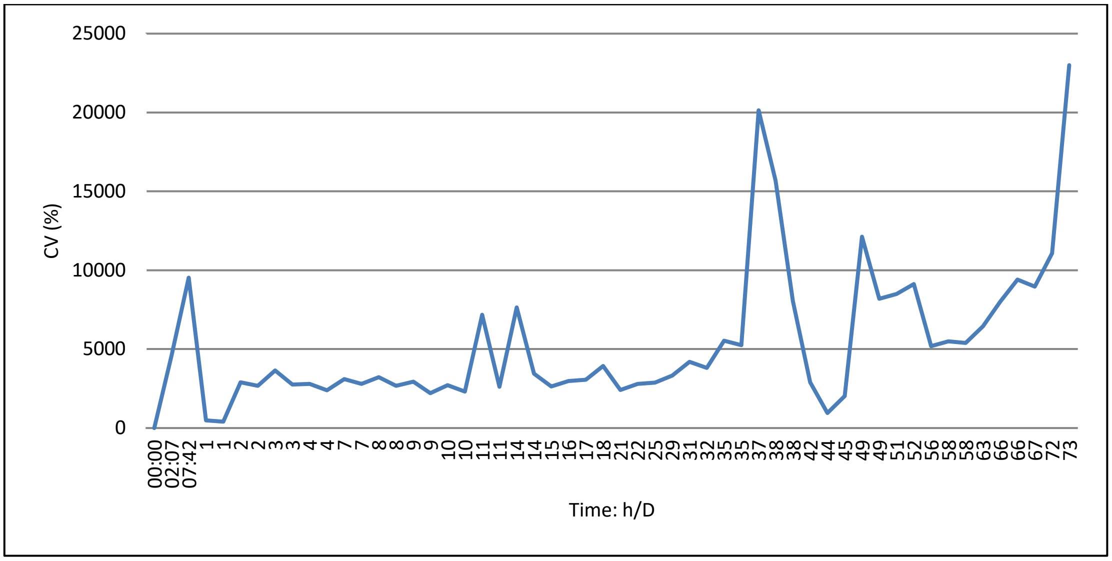

Figure 5.1.c – *Coefficient of variation (CV%) vs time, summarizing the temporal evolution of normalized variability across all measurements.*

Percentile analysis (p_5–p_{95}) confirms the same behaviour. The core range of apparent resistivity changes remains relatively narrow, whereas the outer tails broaden markedly after T02, coinciding with the start of biological activity. This broadening reflects the appearance of localized regions where $\Delta\rho_a$ deviates strongly—either positively (resistive patches) or negatively (conductive zones)—from the bulk median.

5.1.3 Temporal evolution of raw $\Delta\rho_a$

The temporal evolution of $\Delta\rho_a$ provides insight into the progressive transitions associated with microbially mediated transformations (MMT) and microbially influenced electrical responses (MIER) observed during the 73-day experiment. In contrast to the global statistical description above, this section focuses on temporal dynamics and their correspondence with biological and physicochemical processes.

Table 5.1.c – *Summary of events of the temporal evolution of Δρ_a*

Time window / Step	**Approx. time**	**Dominant process**	**Observed Δρ_a trend**	**ERT / RPCA signature**	**Interpretation label**
T00	0 h	Hydraulic–electrical steady state	~0	PC1 flat, very low variance	Baseline equilibrium
T01–T02	0–3 h	Injection of conductive bacterial solution	↓ (initial conductive drop)	Strong sparse S impulse	Injection-driven conductive transient
T03–T05	1–5 d	Fluid redistribution and early bio-physical adjustment	↑ (progressive resistive rebound)	L rising trend	Early post-injection equilibration
T06–T10	5–11 d	Ionic redistribution and metabolic activation	↓ with minimum at ~Day 10–11	L downward with sparse S	Early conductive phase (MMT onset)
T11–T25	11–25 d	Biofilm development and metabolite accumulation	↑ (gradual resistive growth)	L upward, S sparse	Biofilm-controlled resistive phase
T26–T42	25–42 d	System-wide ionic dominance	↓↓ (maximum conductive deviation)	Dominant L downward	Peak conductive phase
T43–T49	42–58 d	Partial ionic consumption / structural rebound	↑ (resistive rebound)	L upward stabilization	Late resistive rebound
T49-T50	66 d	Booster injection (high-conductivity solution)	↓ (conductive drop)	Strong S + L perturbation	Booster-driven conductive event
T51–T53	67–73 d	Post-booster reactivation and re-equilibration	↑ (renewed resistive trend)	L recovery, low S	Post-booster recovery

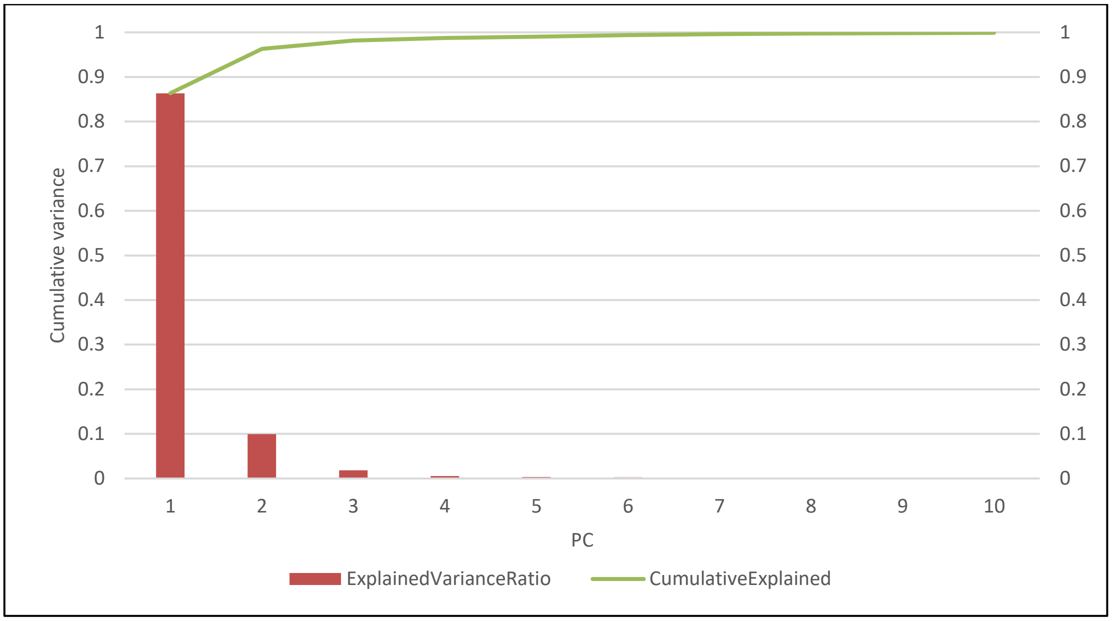

Figure 5.1.d – *Explained variance ratio and cumulative variance from, showing that the first principal components capture >90% of the total variance.*

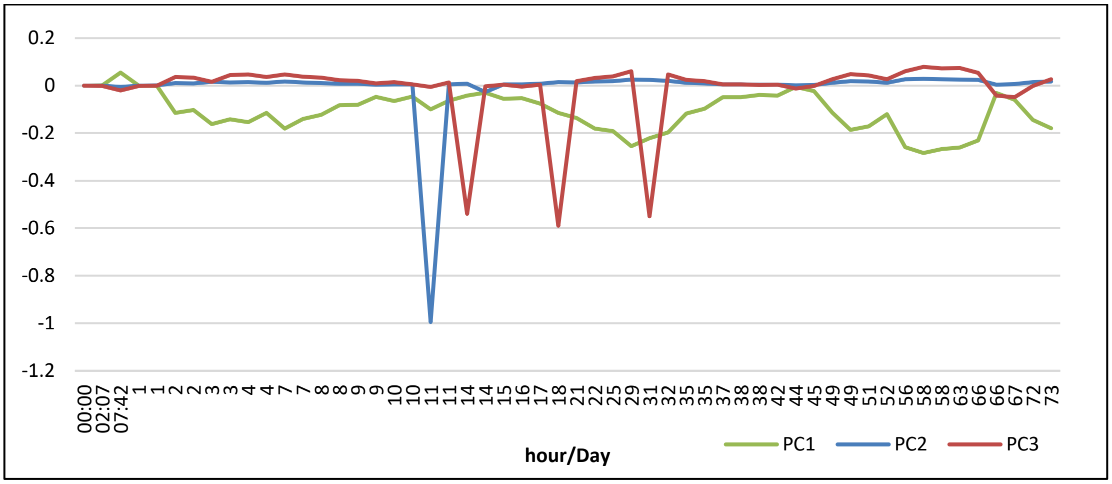

Figure 5.1.e – *Temporal loadings of the first three PCA components, showing their independent, orthogonal temporal signatures.*

Figures 5.1.d and 5.1.e illustrate the dimensionality reduction achieved through PCA, showing that the first principal components capture the majority of temporal variance and exhibit distinct, orthogonal temporal signatures. These components provide a compact representation of the dominant temporal patterns described above and form the basis for the subsequent robust decomposition.

5.1.4 PCA and robust PCA analysis

The PCA analysis described above was extended to a Robust PCA (RPCA) framework to better isolate transient outliers from the coherent background. The $\Delta\rho_a$,% matrix A was decomposed as A = L + S, with L capturing the low-rank background and S the sparse, localized anomalies. This decomposition allows visual inspection through heatmaps. Statistical and multivariate methods such as PCA have been widely used in environmental geophysics (Binley & Slater, 2020); here they provide a detailed separation of global and transient electrical responses within the dataset.

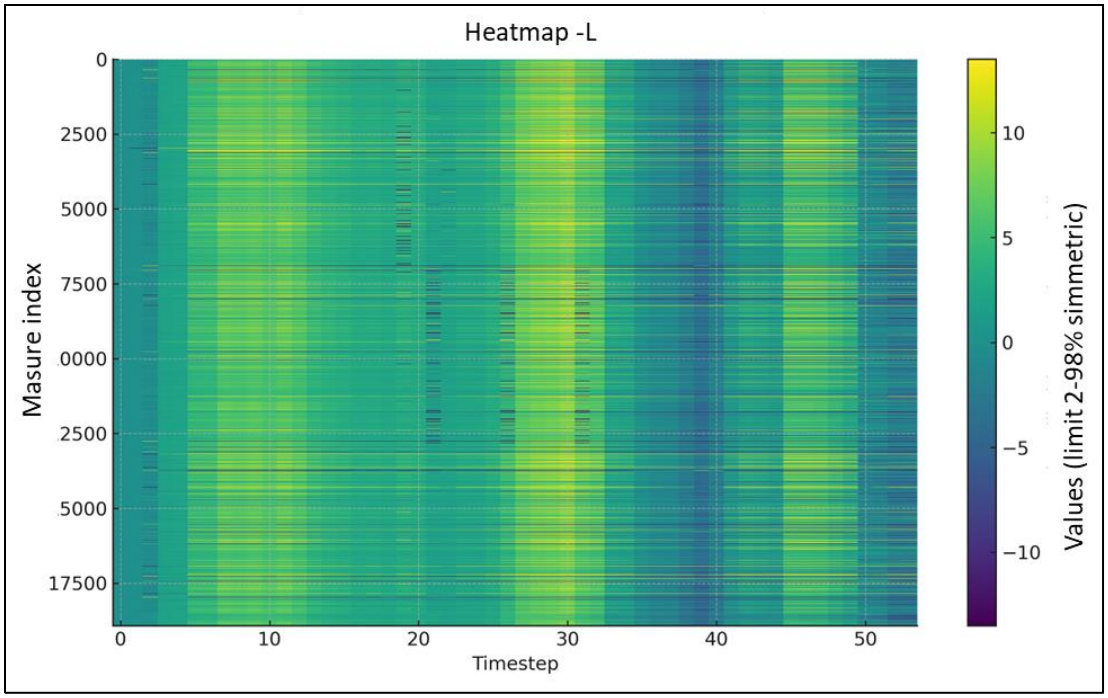

Figure 5.1.f – *RPCA decomposition heatmaps: low-rank component L, and S (next figure) showing respectively the transient anomalies and the coherent background evolution.*

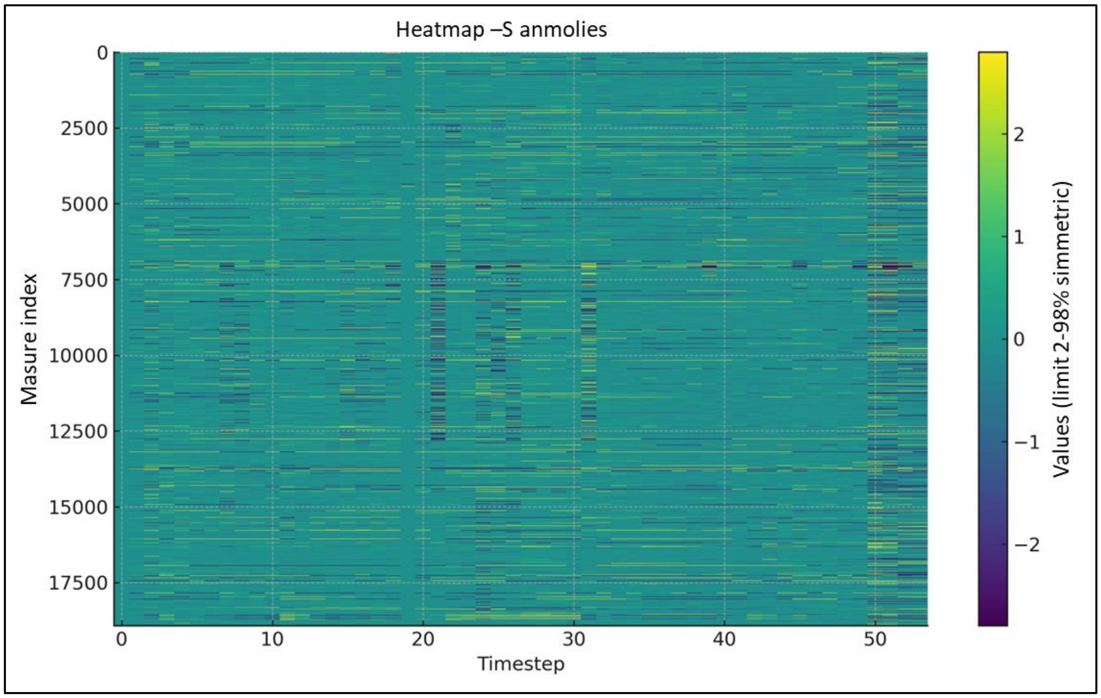

Figure 5.1.g – *RPCA decomposition heatmaps sparse component S*

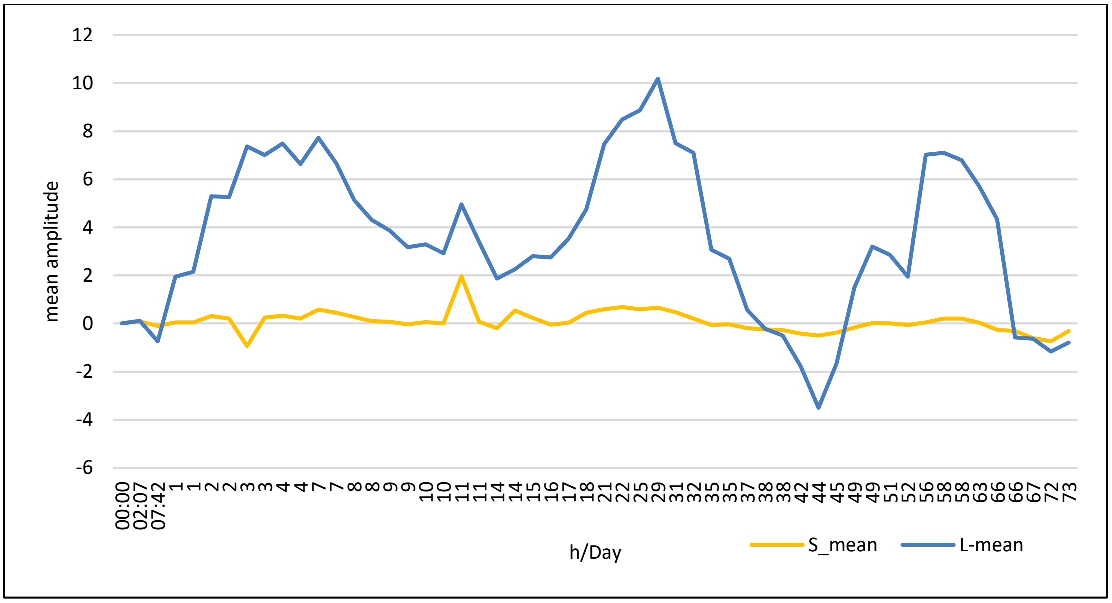

Figure 5.1.h – *Time evolution of S-mean and L-mean derived from RPCA, summarizing the relative strength of sparse events (S) and background trends (L) across the experiment.*

5.1.5 Temperature tracking in raw data

Temperature effects on apparent resistivity were evaluated by comparing $\Delta\rho_a$ against temperature measurements acquired simultaneously in the laboratory.

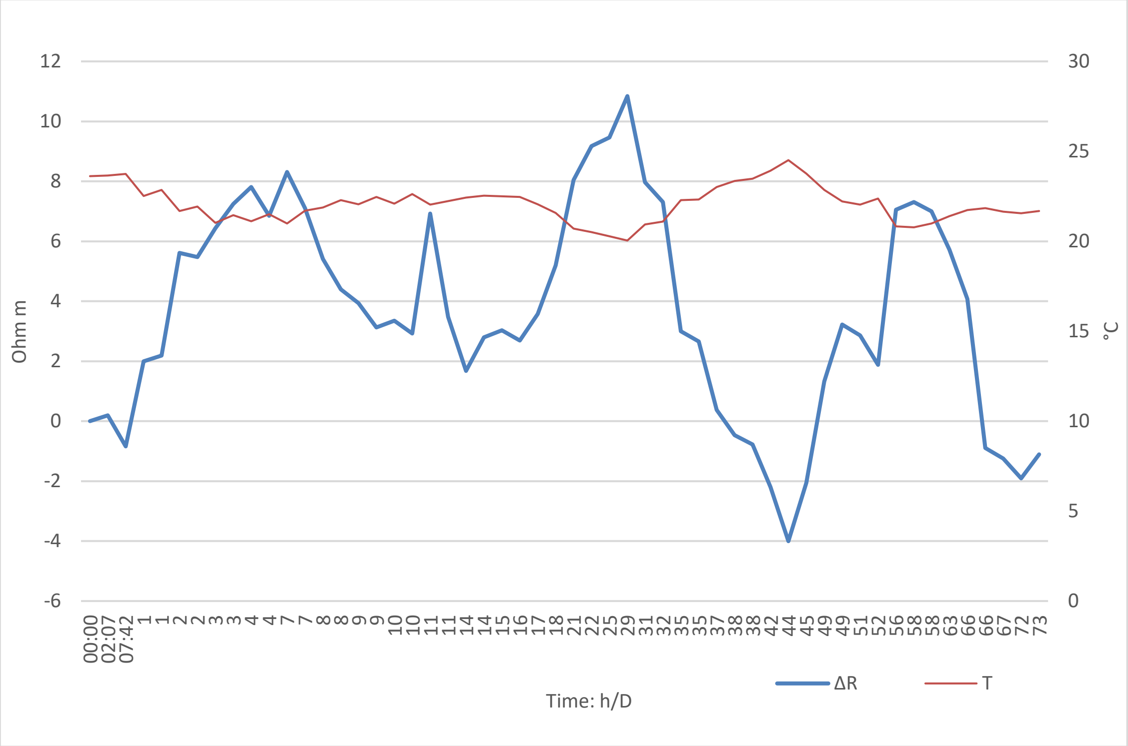

Figure 5.1.i – *$\Delta\rho_a$ vs temperature, showing partial correlation between electrical and thermal trends.*

Figure 5.1.l – *Comparison between original $\Delta\rho_a$ (red line) and temperature-corrected values (blue line), confirming minimal thermal bias.*

The linear approximation $\rho_T \approx \rho_{ref} [1 + \alpha (T - T_{ref})]$ was used with $\alpha \approx 0.02$ °C^{-1}. References for temperature-resistivity behaviour are taken from Herring et al. (2021) and Besson et al. (2019), whose models describe both ionic conduction and activation-energy effects in porous media. Explicit correction is discussed later in Section 5.2.8.

5.1.6 Summary of raw-data analysis

The analysis of the raw $\Delta\rho_a$ dataset reveals several key features (Fig. 5.1.l):

- The distribution of apparent resistivity variations is highly non-Gaussian, dominated by localized and transient anomalies rather than random noise.
- An initial decrease in mean apparent resistivity is observed within the first hours after bacterial injection, reflecting the high conductivity of the injected solution relative to the background pore water.

- This initial conductive response is followed by a progressive increase in resistivity up to approximately Day 5, consistent with redistribution of fluids and early bio-physical adjustments within the porous medium.
- Between Days 5 and 10, resistivity decreases again, reaching a local minimum around Day 10–11, after which a new phase of resistivity increase develops until approximately Day 25.
- The most pronounced conductive phase occurs between Days 25 and 42, during which $\Delta\rho_a$ reaches its maximum negative deviation relative to Day 0 T_{00}, indicating system-wide ionic and metabolic influence.

A subsequent resistive rebound develops, peaking around Day 58, followed by a renewed decrease in resistivity associated with the booster injection at Day 66.

After the booster event, resistivity begins to increase again, suggesting reactivation of microbial processes and partial system re-equilibration.

PCA and RPCA analyses confirm that these phases are temporally coherent across the dataset and are not driven by measurement noise or thermal effects. Collectively, these results provide a statistically robust foundation for the inversion-based 3D reconstruction described in the next section (5.2).

5.1.7 Integrated Interpretation

The statistical analyses presented above indicate that the apparent resistivity variability observed during the 73-day monitoring period arises from the superposition of two main components:

- A low-frequency, system-wide background evolution (low-rank component L), reflecting gradual changes in bulk ionic content, moisture redistribution, and long-term bio-physical processes.

- Localized and transient perturbations (sparse component S), associated with short-lived.

The statistical results provide quantitative constraints on the timing, magnitude, and persistence of apparent resistivity variations, but they do not by themselves allow spatial attribution or causal interpretation of the underlying processes. In particular, no inference on volumetric dominance, spatial extent, or mechanistic drivers is drawn at this stage based solely on statistical indicators.

These results therefore serve as a descriptive and diagnostic framework that guides the subsequent spatial analysis. The localization, geometry, and physical meaning of the observed electrical variations are addressed through three-dimensional inversion in Section 5.2, where statistical trends are evaluated against the reconstructed resistivity distributions.

5.2 Inversion results and model validation

5.2.1 Synthetic forward modelling and sensitivity analysis

Before presenting the inversion results obtained from the experimental dataset, a synthetic forward-modelling exercise was carried out to assess the numerical behaviour, sensitivity distribution, and statistical consistency of the adopted inversion workflow. The objective of this analysis is not to reproduce the experimental system in detail, but to provide a conservative diagnostic framework for evaluating detectability, non-uniqueness, and resolution limits associated with the electrode configuration and inversion strategy.

A synthetic forward model was computed using the same three-dimensional mesh, electrode geometry (surface and borehole electrodes), and acquisition sequence adopted for the experimental inversions. The model domain was assigned a homogeneous resistivity of 100 Ω·m, representative of the uncontaminated sand matrix, in order to verify that no artificial structures arise solely from numerical discretization, meshing, or solver-related effects (Fig. 5.2.a). The absence of spatial artefacts in the forward response confirms the internal consistency of the modelling setup.

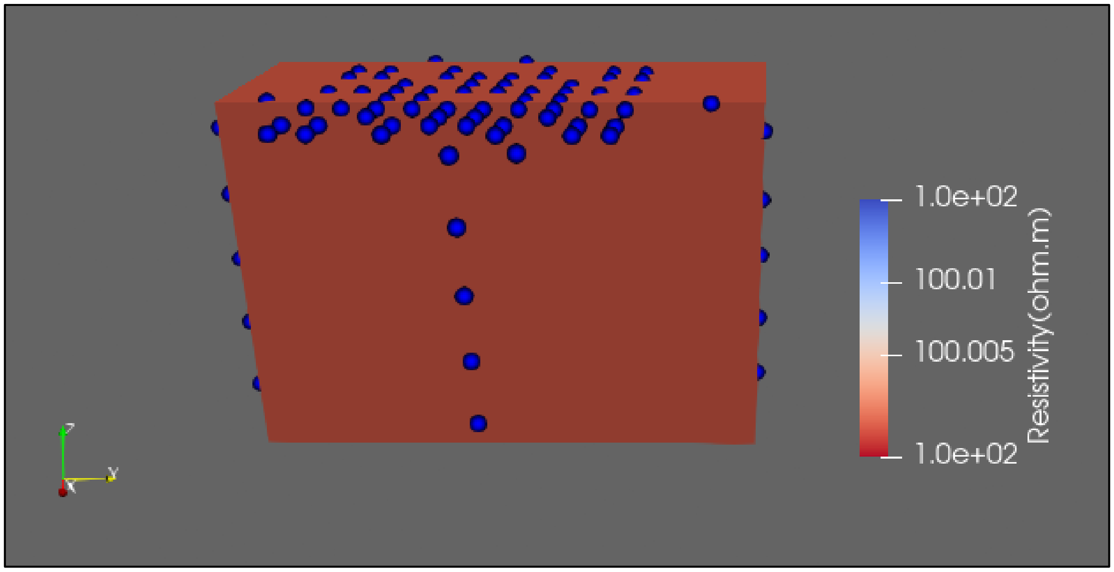

Figure 5.2.a — *Synthetic forward resistivity model computed using the experimental mesh, electrode geometry and acquisition sequence. A homogeneous resistivity of 100 Ω·m was assigned to verify the absence of numerical artefacts*.

To evaluate the intrinsic resolving power of the electrode configuration, the spatial distribution of model sensitivity was computed from the inversion of the synthetic dataset. Figure 5.2.b shows a representative central slice of the logarithmic sensitivity map, overlaid with electrode positions. Sensitivity is highest in the vicinity of electrodes and near the domain boundaries, while it decreases toward the central portions of the tank. Notably, the shallow region corresponding to the bacterial injection area lies within a zone of intermediate sensitivity, close to the transition between well-resolved and weakly resolved domains. Consequently, resistivity variations occurring in this region are expected to be detectable at a bulk scale but recovered with smoothing and reduced contrast.

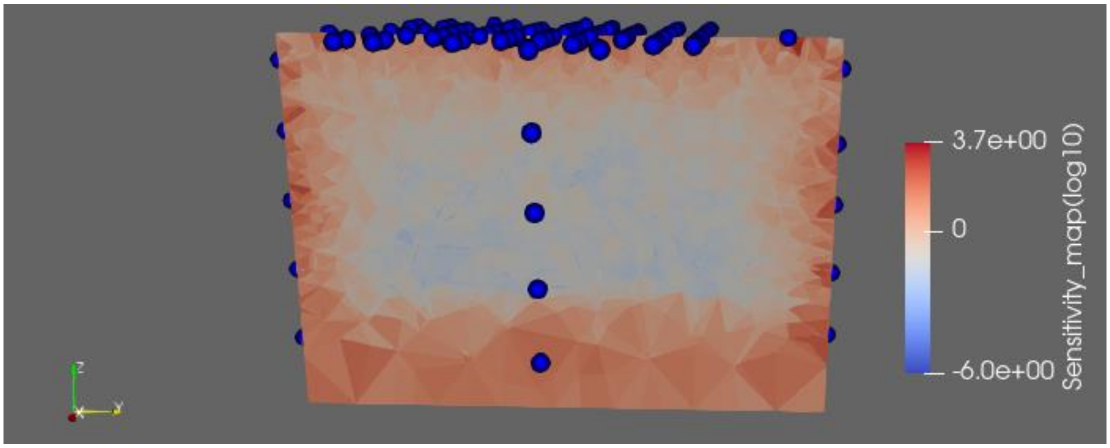

Figure 5.2.b — *Central slice of the logarithmic model sensitivity distribution derived from the inversion of the synthetic forward dataset. Electrode positions are indicated for reference.*

The inversion of the synthetic dataset converged rapidly and exhibited stable numerical behaviour. Figure 5.2.c presents the distribution of normalized residuals obtained after inversion of the noisy synthetic data. Residuals are centered around zero and are largely contained within ±3 standard deviations, indicating that the assumed error model is statistically consistent, and that the inversion does not exhibit systematic bias or overfitting. This result confirms that the inversion framework behaves as expected under controlled conditions and provides a robust baseline for interpreting the experimental time-lapse results.

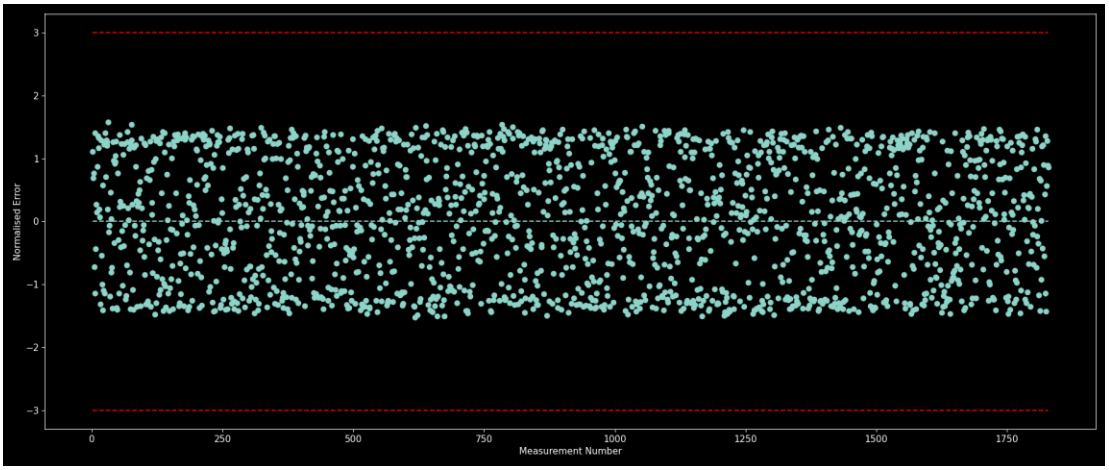

Figure 5.2.c — *Distribution of normalized residuals obtained from the inversion of noisy synthetic data. Residuals are centered around zero and largely contained within ±3 standard deviations*.

5.2.2 Inversion workflow, quality control, and selection of representative time steps

The volumetric inversion of the apparent-resistivity dataset was performed using ResIPy coupled with the R3t finite-element solver, implementing a full three-dimensional smoothness-constrained least-squares approach. The inversion parameterization involved a total of approximately 51 175 model parameters. The model domain, generated in Gmsh, contained approximately 47,800 tetrahedral elements (minimum element quality ≳ 0.72) to ensure sufficient spatial resolution of the contaminated zone while maintaining computational stability.

The full monitoring comprised 54 acquisitions (T00–T53) over 73 days. To maintain computational feasibility while preserving interpretability, inversions were computed on a subset of 12 representative time steps. These were selected to sample the early injection transient, capture the first days of post-injection adjustment, represent intermediate and late stages highlighted by the raw-data statistics (mean, variance, PCA/RPCA), and bracket the late booster perturbation and post-booster evolution.

The selected time steps and their positions within the 73-day experiment are:

- T00 (Day 0; 00:00)
- T01 (Day 0; +2 h 07 min)
- T02 (Day 0; +7 h 42 min)
- T03 (Day 1)
- T11 (Day 7)
- T20 (Day 11)

- T40 (Day 45)
- T49 (Day 66)
- T50 (Day 66; booster injection)
- T51 (Day 67)
- T52 (Day 72)
- T53 (Day 73)

This selection preserves the temporal structure of the experiment while keeping the inversion workflow numerically tractable. In particular, the late-stage perturbation associated with the saline–nutrient booster is explicitly bracketed by T49 (pre-booster) and T50–T53 (post-booster evolution).

The independent inversion workflow was applied to each selected time step to ensure direct comparability between frames while avoiding the introduction of temporal smoothing constraints.

For each selected time step, an independent 3D inversion was performed using identical meshing, electrode configuration, regularization settings, and error weighting to ensure comparability.

The inversion objective function minimized the combined data misfit and model roughness according to:

$$\Psi_{tot(m)} = \big(d - f(m)\big)^{\mathrm{T}} W_{d^{\mathrm{T}}} W_d \big(d - f(m)\big) + \alpha\,(m - m_0)^{\mathrm{T}} R\,(m - m_0)$$

where *d* and *f(m)* denote observed and modelled data, respectively; W_d is the data-weighting matrix; R is the model roughness operator; and α is the regularization parameter controlling the model smoothness. Model updates at each iteration were computed through the linearized system:

$$(J^{\mathrm{T}} W_{d^{\mathrm{T}}} W_d J + \alpha\, R)\Delta m = J^{\mathrm{T}} W_{d^{\mathrm{T}}} W_d \big(d - f(m_{\mathrm{i}})\big) - \alpha\, R\,(m_{\mathrm{i}} - m_0)$$

where J denotes the Jacobian matrix linking model perturbations to predicted data.

Quality control and filtering. Each quadrupole was stacked 3–6 times. Readings with internal standard deviation > 0.5% were rejected prior to inversion. For time-lapse processing (see below), residual-based filtering was additionally applied based on the normalized error distribution.

5.2.3 Time-lapse (TL) inversion strategy

In addition to independent inversions, a time-lapse inversion was performed on the same subset of representative time steps to explicitly assess temporal coherence and to reduce frame-to-frame artefacts. The adopted strategy relies on a background regularization scheme, penalizing deviations from a common reference model rather than enforcing temporal smoothing between consecutive frames. The TL inversion used a regularization-from-initial-model scheme in which each frame is penalized relative to a common reference model (baseline), rather than being smoothed independently. The reference model was provided as Start_res.dat.

Two-pass TL workflow.

1 Initial TL inversion of the selected frames using the regularization-from-initial-model option.
2 Residual-based post-processing: data were filtered using the normalized error (residual) distribution, retaining measurements within −2.5 to +2.5 (normalized units), and the TL inversion was repeated. This second pass reduced inversion artefacts and produced TL models consistent with the independent inversions.

Key TL settings (ResIPy/R3t):

- Data type: Normal
- Regularization mode: Regularization from initial model
- Value for tolerance: 1.2

- Maximum number of iterations: 10
- Error columns: resError (resistivity) and phaseError
- Data weighting parameters: a_wgt = 0.001, b_wgt = 0.02
- Advanced options: sensitivity matrix, patch size (x = 1, y = 1), update the weights, α_aniso = 1.0, α_s = 1.0, 10 parallel threads, crop below mesh fine region enabled.

The TL inversion converged normally for all frames. For the selected time steps, the number of retained measurements per frame ranged approximately from ~1510 to ~1950, depending on filtering.

The consistency between the two inversion strategies was evaluated by direct comparison of the resulting resistivity models. The TL and independent inversions were compared systematically. Both approaches reproduced the same dominant resistivity structures and their temporal evolution (location and polarity of the main anomalies). The observed agreement is used as an internal consistency check supporting the robustness of the inversion-based interpretation.

RMS misfit expression.

$$RMS = \sqrt{\left[\left(\frac{1}{N}\right) \cdot \sum_{i} \left(\frac{(d_{\mathrm{i}} - f_{\mathrm{i}}(m))}{\varepsilon_{\mathrm{i}}}\right)^{2}\right]}$$

Data misfit and model roughness terms.

$$\Psi_d = (d - f(m))^{\mathrm{T}} W_d^{\mathrm{T}} W_d \, (d - f(m))$$

$$\Psi_m = (m - m_0)^{\mathrm{T}} R \, (m - m_0)$$

and

$$\Psi_{tot} = \Psi_d + \alpha \, \Psi_m .$$

Table 5.2.a — *Summary of inversion characteristics for independent and time-lapse inversions*

Parameter	Independent inversions	Time-lapse inversion	Interpretation
RMS error	1.3–1.6	1.45–1.83	Comparable data fit across approaches
Iterations	5–7	6–10	Stable convergence behaviour
Rejected data	~3.7%	3–6% (post-filtering)	Robust residual-based filtering
Model parameters	~51 175	~51 175	Identical parameterization
Measurements per frame	14000–18000	14000–18000	Variable after quality control
Resistivity range (Ω·m)	45–113 (p_5–p_{95})	45–113 (p_5–p_{95})	Stable dynamic range
Regularization	Spatial smoothness	Background (initial-model)	Temporal coherence constraint
Reference model	—	Start_res.dat T00 inverted	Common baseline for TL

5.2.4 Inversion results

Full-domain inversion. The first inversion was performed on the entire sandbox to verify the consistency between the 3D electrical image and the laboratory configuration described previously. The model shows a central resistive nucleus matching the known position of the contaminated block, surrounded by a conductive matrix with resistivities of approximately 100 Ω·m. In addition, a high-resistivity zone at the tank bottom is visible. These geometric characteristics will be revisited in the Discussion.

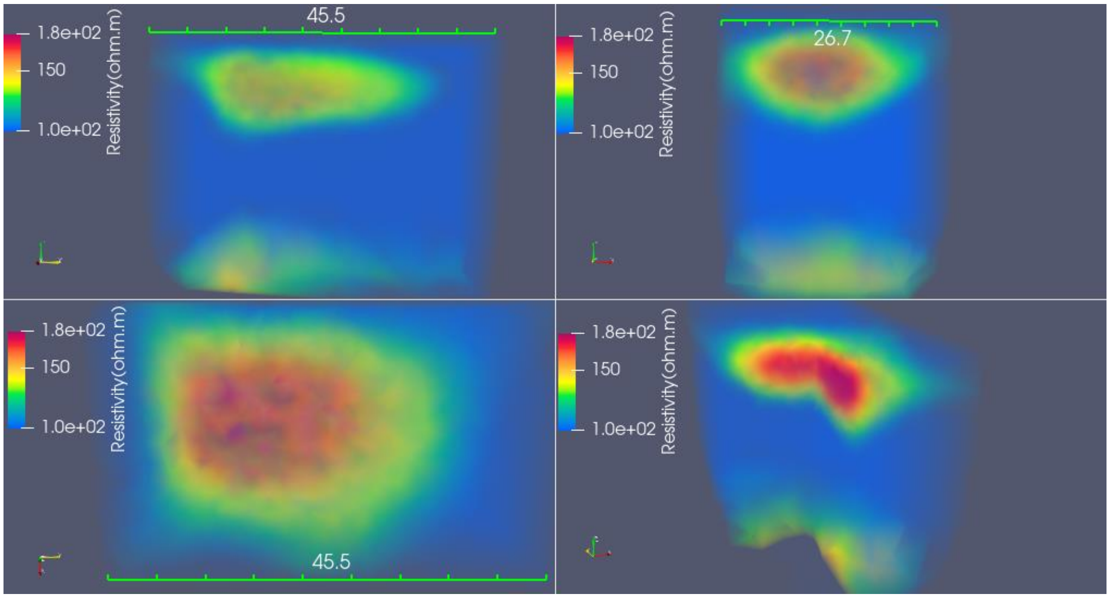

Figure 5.2.d — *Full-domain inverted resistivity model (orthogonal views and volume clip). The central resistive core corresponds to the contaminated block; note the high-resistivity patch at the base of the tank (to be discussed later).*

ROI-focused view**.** In order to facilitate the analysis of the contaminated area, a clip operation in ParaView was applied to isolate the region of interest (ROI) corresponding to the injection zone of bacterial cultures, where biological and ionic transformations were expected. No new inversion was performed: the mesh and inversion are identical to the full-domain case. The clip was introduced purely for visualization and quantitative focus within the contaminated region.

5.2.5 Central cross section

To visualize the spatial and temporal evolution of resistivity within the contaminated sandbox, a series of central cross-sections were extracted from the 3D inversion models computed on the 12 selected representative time steps and compared in ParaView (v5.12). These selected inversions span the full 73-day monitoring window (baseline, early post-injection, intermediate evolution, and late booster/post-booster phase). Fig. 5.2.e and 5.2.f illustrate representative stages of the resistivity evolution across the central vertical plane of the contaminated block. representative stages of the resistivity evolution across the central vertical plane of the contaminated block.

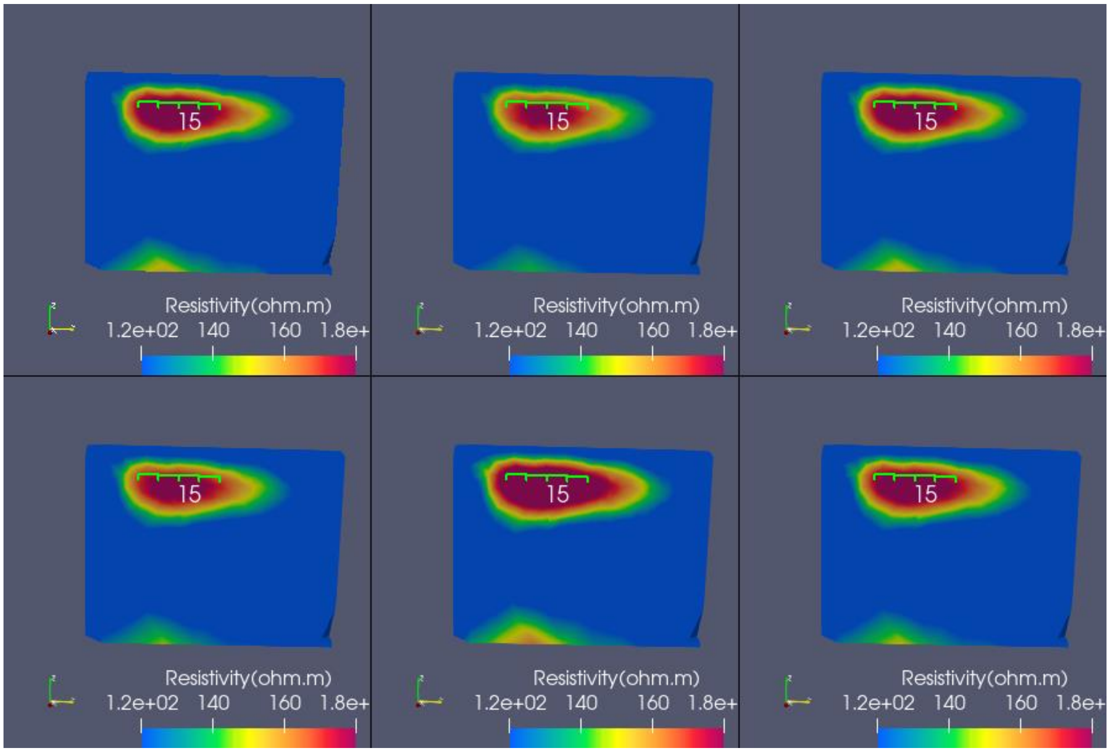

Figure 5.2.e — *Central cross-sections of inverted resistivity model From Top left T00, T01, T02, T03, T11 and T20*

During the early stages, a distinct resistive anomaly (≈180 Ω·m) remains localized in the upper part of the contaminated zone, consistent with the hydrocarbon-rich region described in Chapter 3. The anomaly retains a compact geometry, reflecting limited ionic mobility prior to significant microbial or chemical transformation.

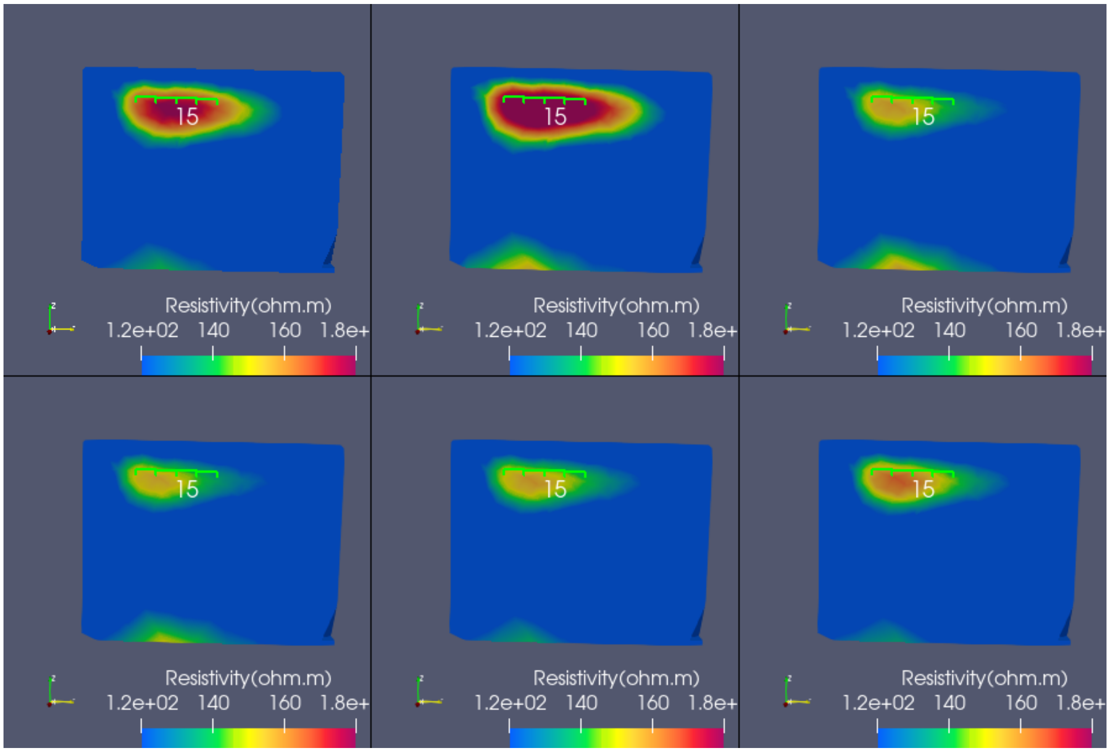

Figure 5.2.f — *Central cross-sections of inverted resistivity model From Top left T40, T49, T50, T51, T52 and T53.*

In later stages, the resistive nucleus progressively weakens and expands laterally, while a conductive halo develops around it. This behaviour indicates redistribution of charge carriers and the transition from resistive dominance (hydrocarbon barrier) to conductive dominance (ionic/biofilm-related processes). Identical meshing, color scaling and inversion parameters were used for all time steps, ensuring consistent comparison across the entire 73-day monitoring window.

In addition to vertical sections, plan-view reconstructions were analyzed to assess lateral propagation of resistivity variations (Fig. 5.2.n) while a vertical profile is reported in (Fig. 5.2.p).

Within this ROI (Fig. 5.3.g) the contaminated block appears as a high-resistivity volume (> 180 Ω·m) enveloped by a surrounding zone with resistivities between 120–140 Ω·m, while the outer matrix remains more conductive (~100 Ω·m). The spatial coherence confirms the correct positioning of the contaminated region and its electrical distinctiveness from the surrounding sand.

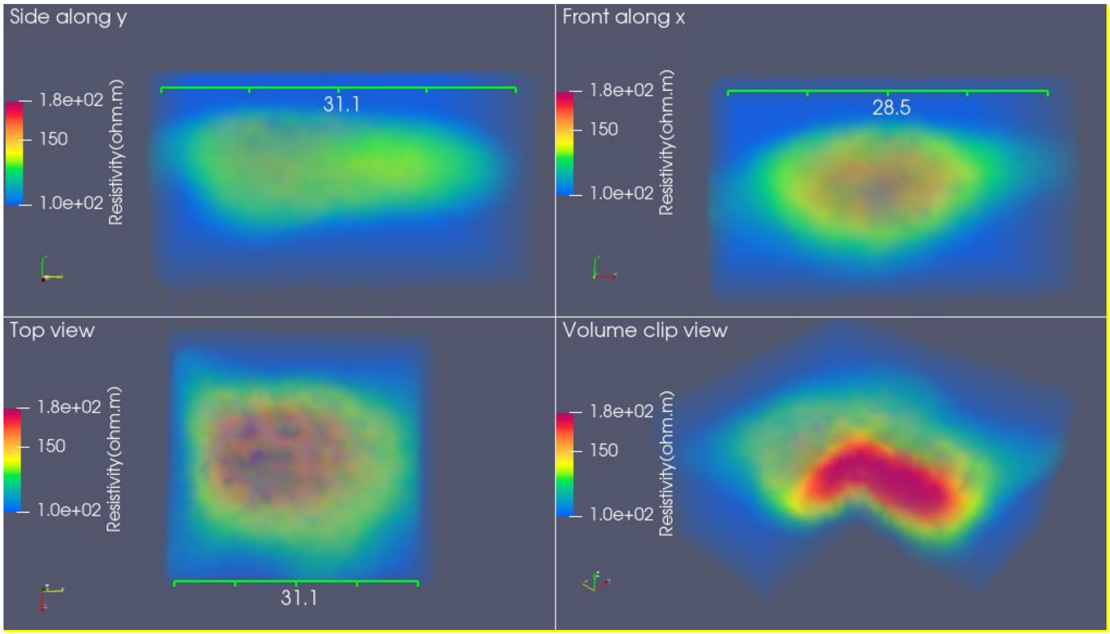

Figure 5.2.g — *ROI-focused inversion and clipped 3D view of the contaminated volume; the resistive nucleus is outlined within a relatively more conductive matrix.*

Applying a resistivity threshold of >150 Ω·m (Fig. 5.2.h.) isolates the geometry of the diesel-impregnated block. The extracted volume closely matches the physical dimensions measured during the setup (15×8×4 cm), confirming that the inversion accurately captures the resistive core associated with the contaminated material.

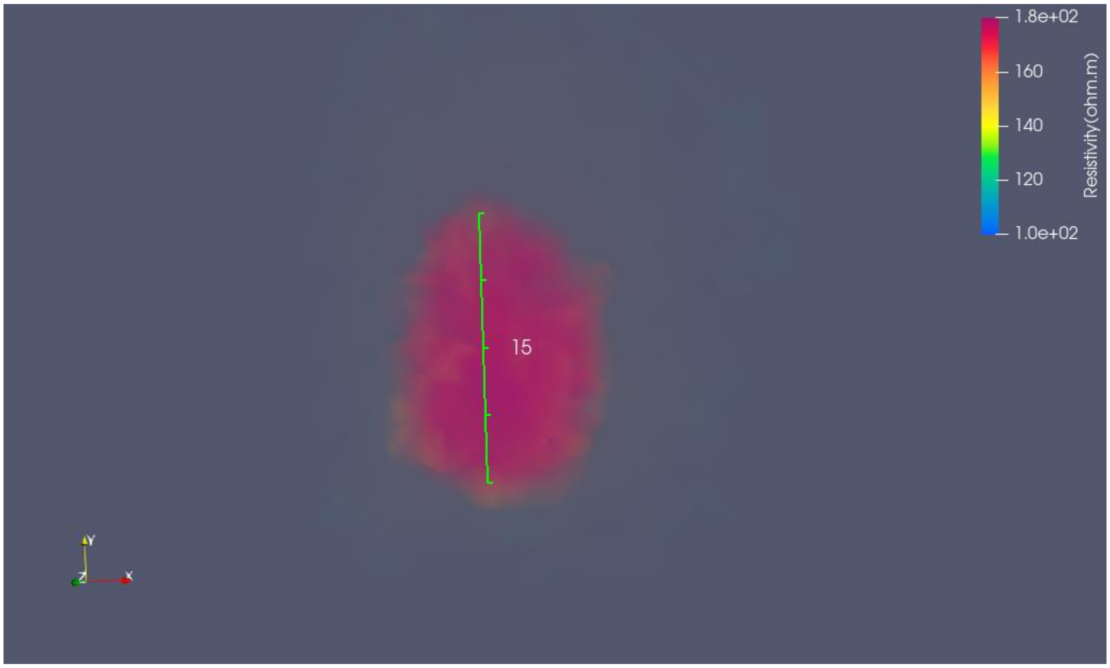

Figure 5.2.h — *Threshold (> 150 Ω·m) visualization of the original contaminated block, clearly outlining its initial geometry.*

5.2.6 Temporal evolution of inverted resistivity volumes

This section presents the temporal evolution of differential resistivity maps $\Delta\rho$ (T_i − T00) derived from both independent inversions and the time-lapse (TL) inversion framework. The comparison between the two approaches shows first-order coherence in the spatial distribution, polarity, and timing of the main resistivity anomalies, providing an internal consistency check before detailed interpretation

5.2.6.1 Raw data coherence and spatial validation

The temporal evolution of the inverted resistivity volumes was analysed in conjunction with the apparent resistivity trend observed in the raw dataset (Fig. 5.1.a). The $\Delta\rho_a$_mean vs. standard deviation plot provides a global reference framework for interpreting the sequence of inverted models. Each time step T_i was compared to the baseline T_0, and the spatial variations were evaluated as differential resistivity maps ($\Delta\rho_a = \rho_a(T_i) - \rho_a(T_{00})$). This approach highlights the progressive electrical evolution of the system, directly linking the volumetric inversion results to the laboratory measurements.

The sequence of $\Delta\rho_a$ ($T_i - T_0$) volumes confirms the same overall behaviour observed in the raw dataset, representing a spatially resolved counterpart of the temporal evolution of resistivity (Fig. 5.2.i, 5.2.l, 5.2.m):

- T01–T02 (Day 0; +2 h to +7 h 42 min) — A conductive transient is observed immediately after bacterial injection, consistent with the high conductivity of the injected solution. The contaminated core remains geometrically stable, while the surrounding matrix shows a measurable conductive response.
- T03 (Day 1) — The resistivity field begins to diverge from the baseline, reflecting early post-injection redistribution processes.
- T11 (Day 7) — A pronounced resistivity increase is visible in the contaminated region and its surroundings, consistent with the intermediate resistive stage observed in the raw-data mean trend.
- T20 (Day 11) — Resistivity decreases again relative to the previous stage, marking the start of a more conductive regime.
- T40 (Day 45) — A general reduction in resistivity occurs across a broad portion of the domain, corresponding to the strongest conductive phase identified in the temporal statistics.
- T49 (Day 66) — This frame captures the late stage immediately before the booster perturbation window.
- T50–T53 (Days 67–73) — Post-booster frames show the re-organization of resistivity patterns and the progressive re-equilibration of the system.

These spatial patterns reproduce the resistivity trend from the raw data: initial equilibration, resistivity rise during bacterial growth, conductive phase following ionic and metabolic activity, and stabilization after the booster injection. The $\Delta\rho_a$ maps thus provide a three-dimensional reconstruction of the temporal dynamics inferred from statistical analysis.

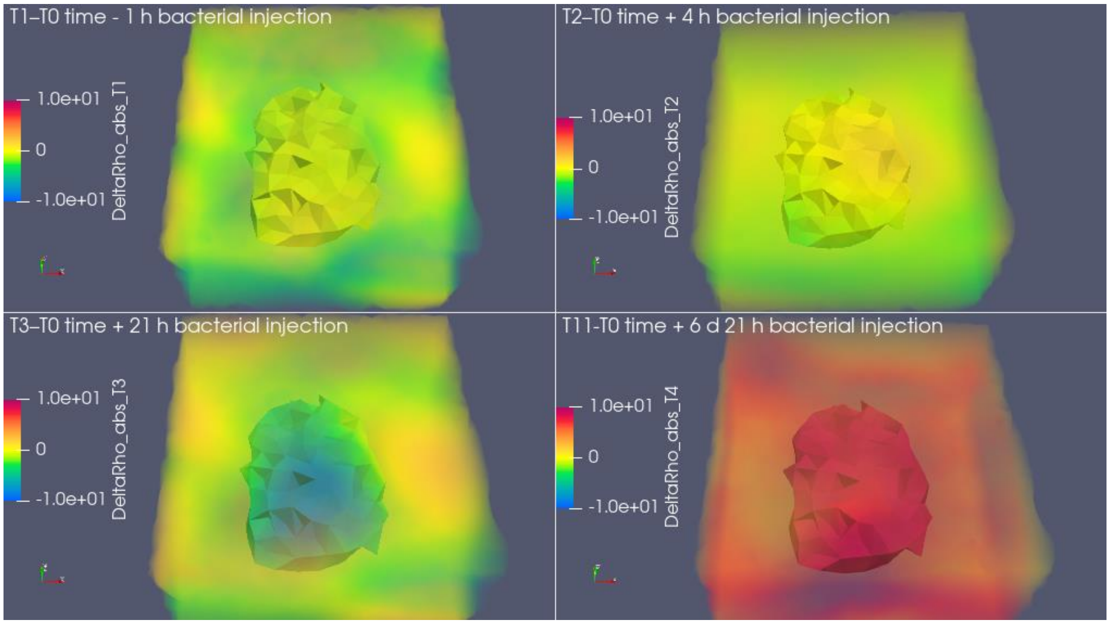

Figure 5.2.i — *Differential apparent resistivity maps,* $\Delta\rho_a = \rho_a(T_i) - \rho_a(T_{00})$*, early stages (T01, T02, T03, T11; scale ±10 Ω·m). Between T01 and T02 no significant resistivity variations are observed with respect to the baseline, indicating that the bacterial inoculation did not immediately induce measurable electrical changes at the scale of the inversion. At T03, a localized decrease in resistivity becomes visible within the contaminated nucleus, marking the onset of an active phase following injection. By T11, a pronounced resistivity increase develops within the contaminated volume, corresponding to a major reorganization of the electrical properties of the system.*

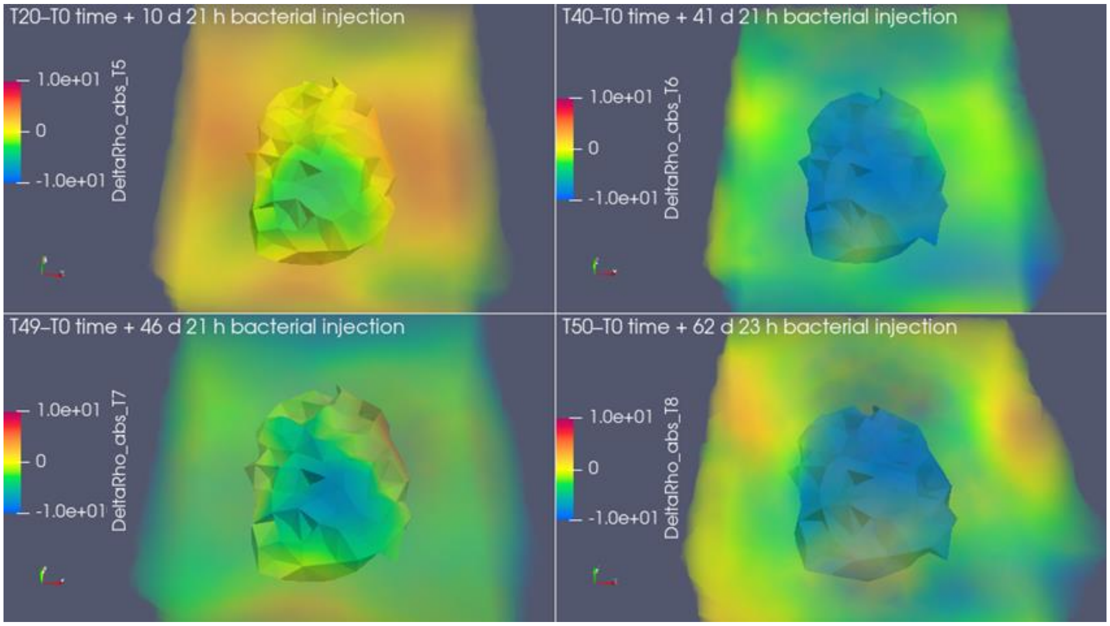

Figure 5.2.l — *Differential apparent resistivity maps, $\Delta\rho_a = \rho_a(T_i) - \rho_a(T00)$, intermediate stages (T20, T40, T49, T50; scale ±10 Ω·m). — $\Delta\rho_a$ (-10/+10 Ohm m); intermediate stages (T20–T50). The resistivity within the contaminated core after T20 decreases while the surrounding region becomes more conductive, revealing the expansion of the bio-ionic halo associated with bacterial and ionic processes At T20, a slight decrease in resistivity is observed within the contaminated volume, mainly localized in the lower portion corresponding to the Rhodococcus inoculation sector, while the surrounding matrix exhibits a mild resistivity increase relative to the baseline. At T40, a more generalized resistivity decrease affects both the contaminated core and the surrounding zone. At T49, spatial heterogeneity becomes evident within the contaminated volume, with the Rhodococcus-inoculated sector appearing more conductive than the Escherichia side, in agreement with the late-stage evolution highlighted by the raw-data resistivity trends. At T50, immediately after the saline–nutrient booster injection, a marked resistivity decrease develops within the contaminated volume, while the surrounding matrix shows a less pronounced conductive response.*

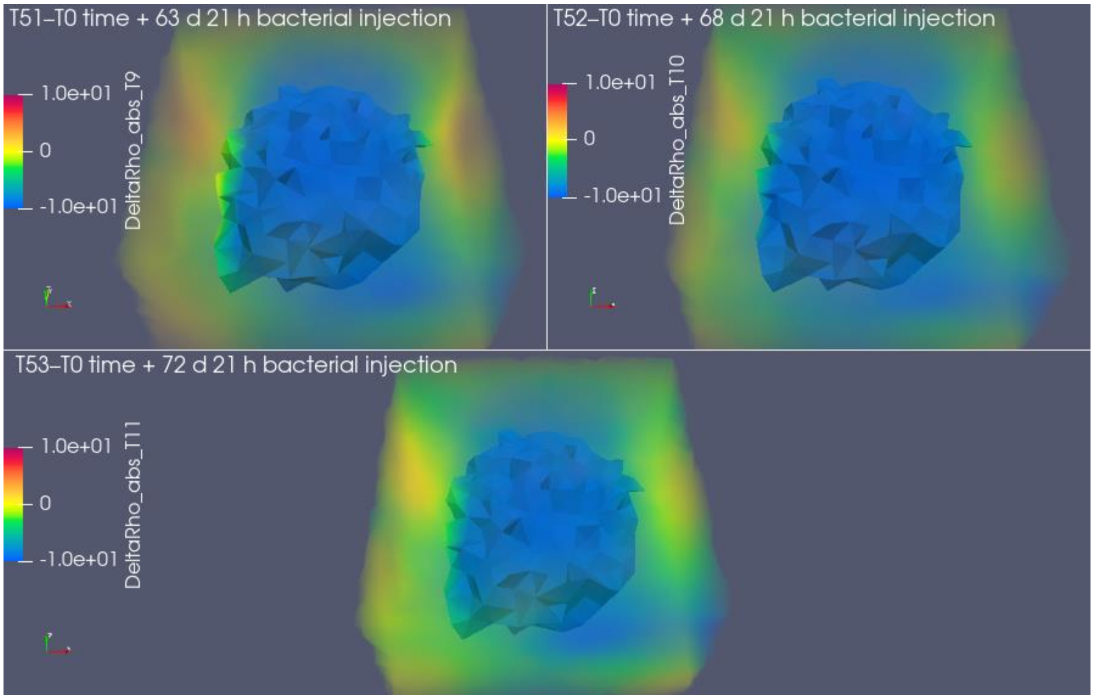

Figure 5.2.m — *Differential apparent resistivity maps, $\Delta\rho_a = \rho_a(T_i) - \rho_a(T00)$, late stages (T51–T53; scale ±10 Ω·m). Following the saline–nutrient booster injection, a marked and spatially coherent decrease in resistivity persists within the contaminated volume and extends into the surrounding matrix. The conductive anomaly remains stable from T51 to T53, indicating a sustained system-wide response rather than a transient perturbation. This behaviour is consistent with enhanced ionic availability and renewed microbial activity following nutrient addition, affecting both the diesel-impregnated core and the adjacent porous medium.*

5.2.6.2 Plan-View and depth-wise consistency of inversion results

To ensure the robustness and internal coherence of the inversion process, a set of global quality diagnostics was performed. These analyses validate the stability of the inverted models and the consistency between observed and modelled data, providing statistical and geometric insight into the reliability of the inversion results (Fig. 5.2.n, 5.2.o, 5.2.p).

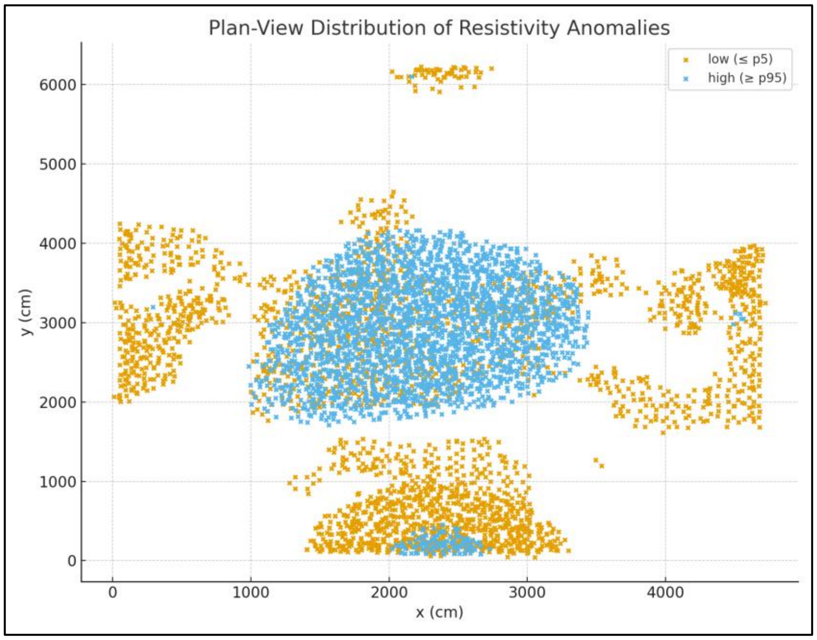

Figure 5.2.n — *Plan-view distribution of low (≤ p_5) and high (≥ p_{95}) resistivity anomalies. The low-resistivity zones outline conductive regions related to bacterial and ionic processes, while the high-resistivity core matches the contaminated nucleus.*

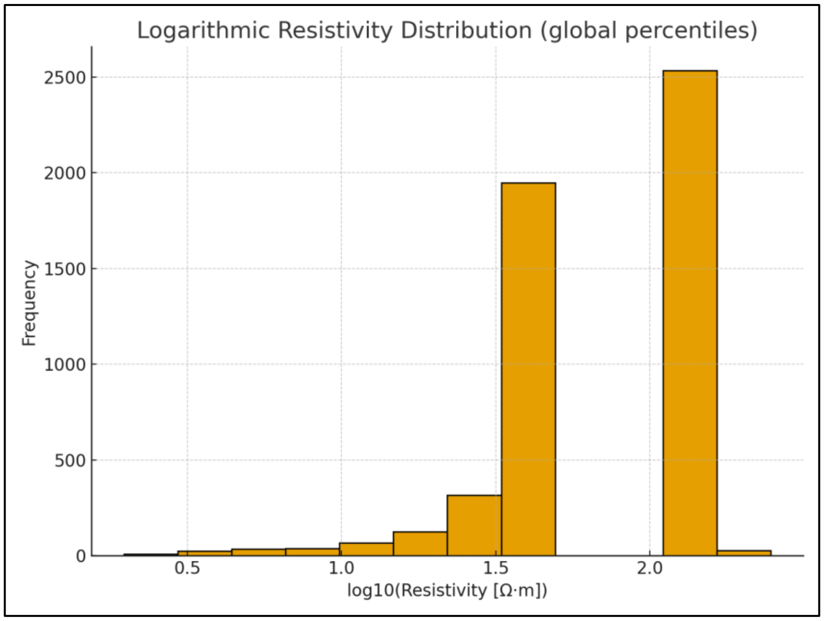

Figure 5.2.o — *Logarithmic distribution of resistivity values (global percentiles). The data follow a non-Gaussian distribution, with distinct conductive and resistive populations reflecting structural and biochemical variability.*

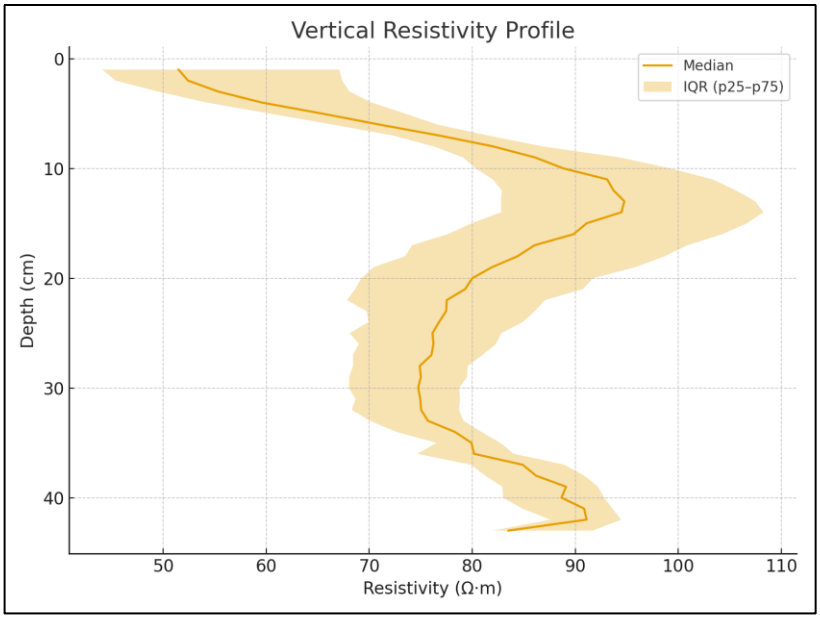

Figure 5.2.p — *Vertical resistivity profile showing the median and interquartile range (IQR). The shallow layers exhibit lower resistivity due to moisture and ionic effects, while deeper levels maintain higher values consistent with compacted and less reactive sand.*

The convergence between temporal trends, spatial distributions, and statistical diagnostics confirms that the inversion products are physically coherent with the measured data and laboratory evolution. This integration provides the foundation for the discussion section, where the electrical signatures are interpreted in terms of bio-electrochemical and hydro-ionic processes.

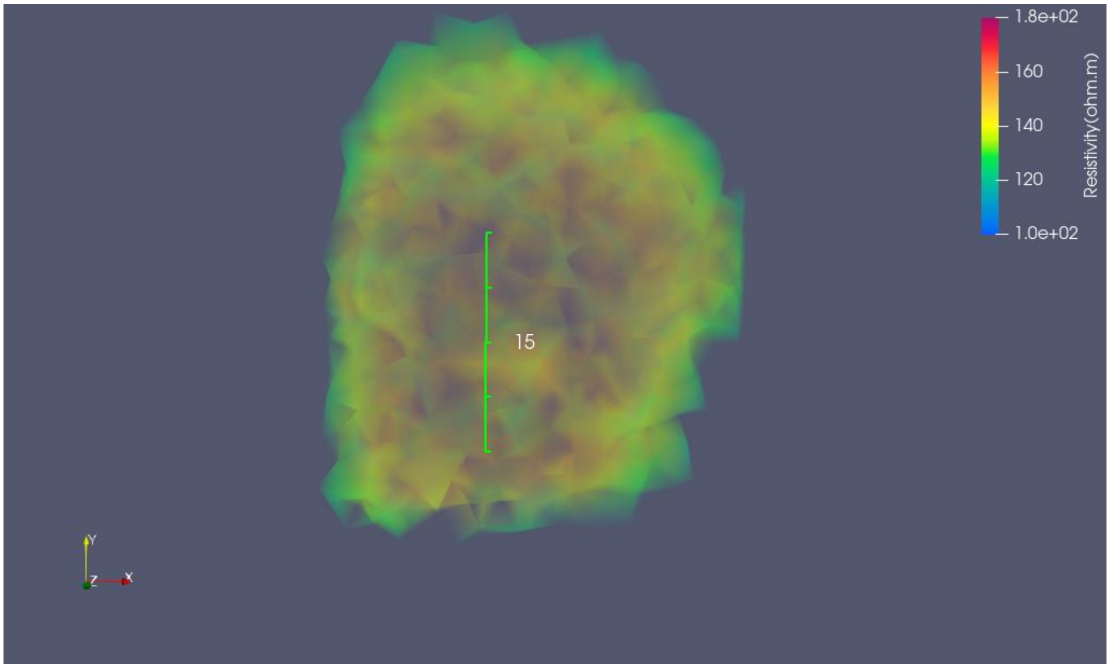

Figure 5.2.q — *Threshold representation (120 Ω·m) at T40 showing the diffusion of the original resistive core.*

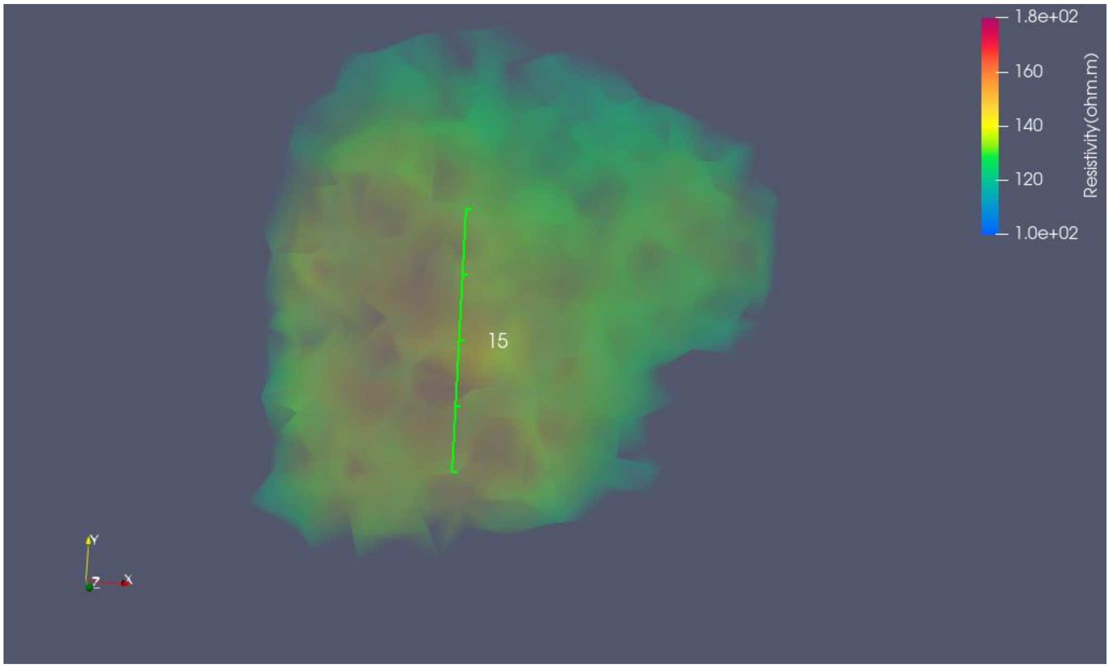

Figure 5.2.r — *Post-booster distribution showing the conductive halo surrounding the residual resistive core.*

By T49, the resistivity pattern stabilizes, confirming that the main electrical transformation occurred prior to the booster and was governed largely by autonomous microbial and ionic dynamics.

5.2.7 Statistical synthesis of inverted models

For each inverted volume, robust statistics (min, p_5, p_{25}, median, p_{75}, p_{95}, max) were computed. Median resistivity decreased from ≈ 150 Ω·m at T_0 to ≈ 85 Ω·m at T0**7**, and to ≈ 70 Ω·m post-booster (T08). The interquartile range expanded through time, confirming increasing electrical heterogeneity. The coefficient of variation (CV) rose from 0.18 to 0.47, reflecting a shift from a nearly uniform to a markedly heterogeneous system. These statistics quantitatively corroborate the visual interpretation of progressive conductivity increase and structural diffusion of the resistive nucleus.

5.2.8 Modal decomposition of inverted Δρ fields (SVD)

To isolate the dominant spatial–temporal patterns underlying the observed resistivity evolution, a modal decomposition was applied to the temperature-corrected and normalized Δρ% dataset, organized as a voxel × time matrix (Fig. 5.2.s). The analysis was performed using Singular Value Decomposition (SVD), which allows separation of orthogonal spatial structures and their associated temporal evolutions while ranking them according to their contribution to the total variance.

The decomposition follows the standard formulation:

$$A = U \Sigma V^T$$

where **A** is the matrix of normalized resistivity variations, **U** contains orthogonal spatial modes (columns), **V** the corresponding temporal modes, and **Σ** the diagonal matrix of singular values representing variance contributions. Retaining the first three modes accounted for > 90 % of the total variance, describing the main physical processes captured by the inversion. Formally, the kth mode contribution at voxel *i* and time *j* is:

$$U_{ik}\,\Sigma_{kk}\,V_{jk}$$

and the rank-r approximation of the dataset is:

$$A_r = \Sigma_{k=1}^{r}\,U\_{:k}\,\Sigma_{kk}\,V\_{:k}^{T}$$

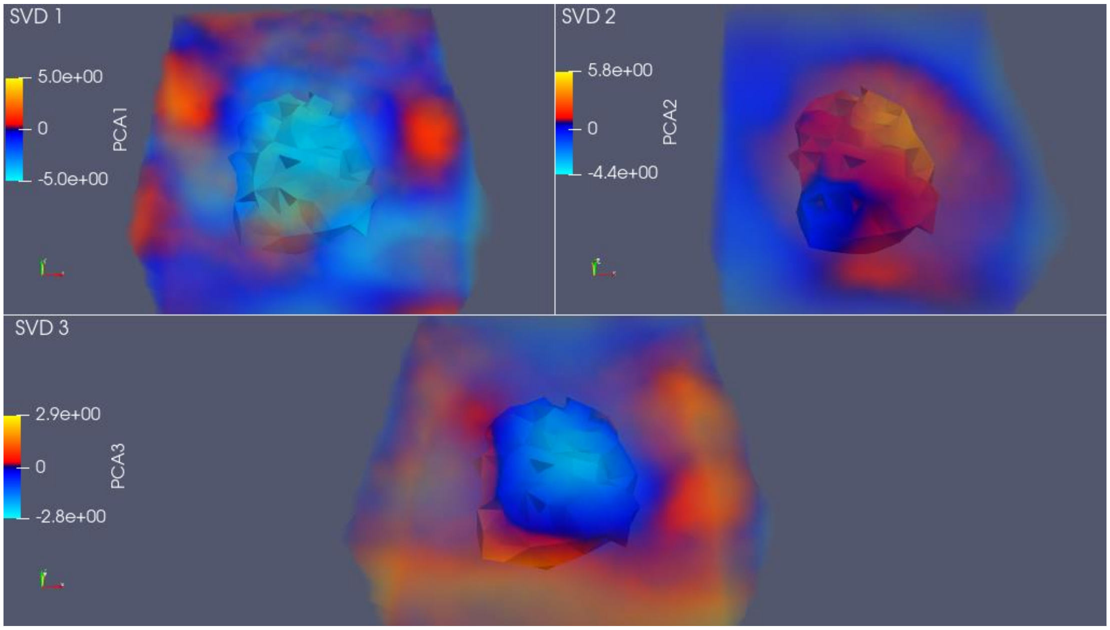

Figure 5.2.s — *Principal spatial modes (SVD1–SVD3) obtained from Singular Value Decomposition of the normalized Δρ% inversion fields. Each panel shows the spatial distribution of one orthogonal mode, scaled according to its individual variance contribution (note the different colour bars). SVD1 represents the dominant rim–core polarity associated with the long-term structural evolution of the contaminated block. SVD2 captures transient and asymmetric conductive patterns within the contaminated volume, reflecting temporally localized and spatially differentiated processes. SVD3 highlights lower-amplitude peripheral variations, interpreted as*

secondary ionic or biofilm-related effects. Together, the first three modes account for more than 90% of the total variance, indicating that the observed resistivity dynamics are controlled by a limited number of coherent eco-physical processes.

The first spatial mode (SVD1) captures the dominant rim–core polarity within the contaminated volume, separating the diesel-impregnated resistive nucleus from the surrounding, more conductive matrix. This mode reflects the long-term structural evolution of the contaminated block and represents the primary contribution to resistivity variance. Its spatial coherence and persistence through time indicate that it is controlled by large-scale eco-physical processes rather than transient perturbations.

The second mode (SVD2) highlights asymmetric and transient conductive structures within the contaminated volume, consistent with temporally localized responses observed in the time-lapse inversion. This mode captures the differentiated evolution between sub-regions of the contaminated block, including contrasts between the Rhodococcus- and Escherichia-inoculated sides, and is interpreted as reflecting biologically mediated redistribution of ionic pathways during intermediate stages of the experiment.

The third mode (SVD3) is characterized by lower-amplitude, peripheral spatial patterns, mainly expressed at the margins of the contaminated volume and in the surrounding matrix. This mode is interpreted as representing secondary processes, such as localized ionic migration, biofilm-related fluctuations, or redistribution effects induced by boundary conditions and fluid circulation, rather than primary biodegradation dynamics.

Importantly, the decreasing magnitude of the singular values from SVD1 to SVD3 explains the different color scales adopted for each spatial component in Fig. 5.2.s. Each mode is scaled according to its own variance contribution, and the absolute amplitudes are therefore not directly comparable across modes. Instead, the spatial patterns should be interpreted in a relative sense within each mode.

Overall, the SVD analysis confirms that the resistivity variations observed in the time-lapse ERT data are dominated by structured, physically and biologically meaningful processes within the contaminated region. The persistence of these modes after temperature correction further supports the interpretation that the electrical response is governed primarily by eco-physical interactions, including microbial activity and ionic reorganization, rather than by external or instrumental effects.

5.2.9 Temperature correction applied post inversion and residual SVD.

During the monitoring period, the sandbox temperature varied between approximately 20 °C and 24 °C. Electrical resistivity is known to depend on temperature according to an approximately linear empirical relationship:

$$\rho_T = \rho^{22}[1 + \alpha\,(T - 22)] \quad with\,\alpha \approx 0.02\,°C^{-1}$$

Although the magnitude of the expected temperature-induced resistivity variations is small compared to the observed Δρ amplitudes, an explicit correction was applied to isolate non-thermal contributions and to ensure that the dominant modes extracted by SVD reflect eco-physical and biological processes rather than seasonal or experimental temperature drift. Rather than applying a simple voxel-wise temperature correction prior to inversion, the temperature-correlated component was removed a posteriori from the normalized Δρ% matrix used for modal analysis. Let A denote the voxel × time matrix of normalized resistivity variations, and t the standardized temperature vector (length equal to the number of time steps). The orthogonal projector onto the subspace complementary to t is defined as:

$$M = I - \frac{t\,t^{\mathrm{T}}}{t^{\mathrm{T}}\,t}$$

The residual matrix is then obtained as:

$$A_{res} = A\,M = A - A\frac{t\,t^{\mathrm{T}}}{t^{\mathrm{T}}\,t}$$

This operation removes, by construction, the rank-1 component of A that is maximally correlated with temperature, without altering the spatial geometry of the remaining signals. The approach is mathematically justified in that it preserves all variability orthogonal to the thermal trend, while explicitly suppressing temperature-driven covariance. Singular Value Decomposition was subsequently applied to the residual matrix A_{res}.

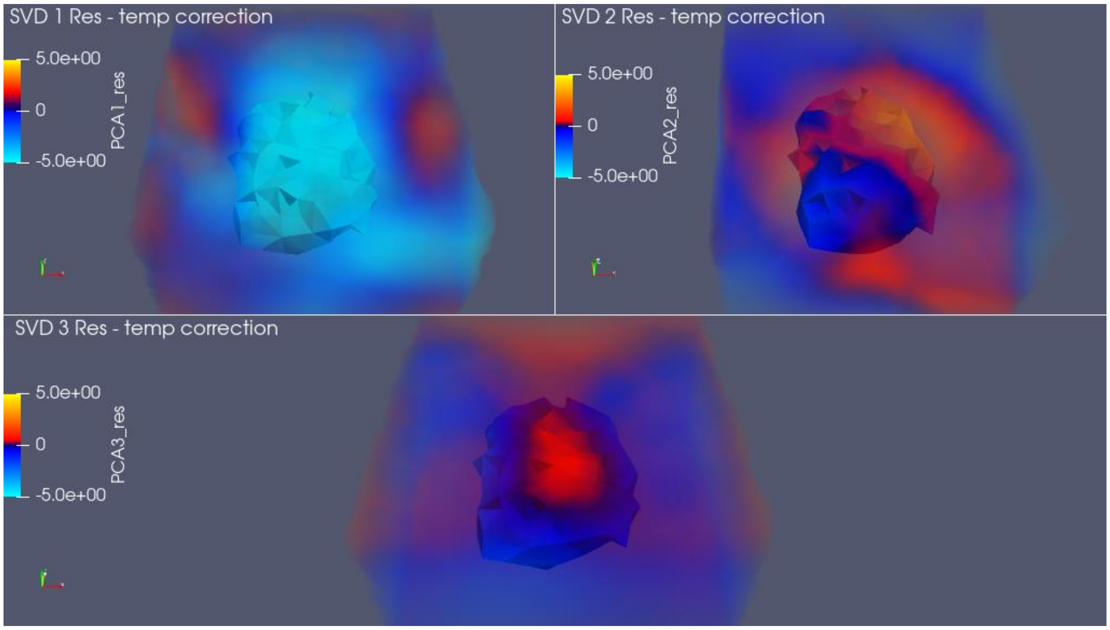

Figure 5.2.t — *Principal spatial modes (SVD1–SVD3) obtained from Singular Value Decomposition of the residual Δρ% matrix after removal of the temperature-correlated component. The temperature contribution was removed by orthogonal projection prior to SVD, ensuring that the displayed modes represent non-thermal variability only. Despite temperature correction, the dominant spatial structures—such as the rim–core polarity of the contaminated block and internal asymmetric patterns—are preserved, indicating that the observed resistivity evolution is primarily governed by eco-physical and biological processes rather than by thermal effects.*

The resulting spatial modes (Fig. 5.2.t) display coherent and localized structures comparable to those obtained from the uncorrected Δρ% analysis. In particular, the persistence of the rim–core polarity within the contaminated volume and of asymmetric internal patterns demonstrates that the dominant resistivity variations are not controlled by temperature fluctuations. The similarity between pre- and post-correction SVD results confirms that thermal effects play a secondary role in the observed resistivity evolution. Consequently, the electrical dynamics documented in this study can be confidently attributed to non-thermal processes, including microbial activity, ionic redistribution, and biofilm-mediated modifications of pore-scale connectivity.

5.2.10 Integrated interpretation of inverted results

The inversion-derived resistivity evolution reveals a coherent chronological sequence:

- Initial state (T00): A distinct resistive nucleus (> 150 Ω·m) corresponds precisely to the diesel-contaminated block.
- Early phase (T03–T11): The onset of conductivity increases signals activation of transport processes around the block.
- Autonomous evolution (T20–T49): Progressive diffusion of the resistive boundary and development of a conductive halo without external stimulation.
- Booster effect (T49-T50)**:** Reinforcement of an ongoing process; the conductive region encloses the residual resistive pocket.
- Stabilization (T51–T53): System approaches a mixed steady pattern with conductive rim and resistive pockets.

Residual modal analysis further demonstrates that these variations are not explained by temperature, confirming their non-thermal origin. The 3D inverted models thus provide a physically consistent representation of subsurface electrical evolution, forming the foundation for the discussion in Chapter 6.

5.3 Bacterial DNA Sequencing Results

5.3.1 Overview of biological sampling and analysis

The biological characterization aimed to determine the microbial composition within the contaminated zone at the end of the ERT monitoring experiment. Three sampling sectors were defined according to the initial bacterial inoculation layout: (i) the *Rhodococcus* side, (ii) the *Escherichia* side, and (iii) a reference uncontaminated sector (Blank). Each zone was sampled in two or three vertical sub-aliquots to capture the spatial variability of the microbial community. The *Rhodococcus* area was represented by three samples (top, middle, and bottom), the *Escherichia* sector by two (top and middle), while the uncontaminated control (Blank) consisted of one composite sample.

DNA was extracted using the DNeasy PowerSoil kit and sequenced through Illumina MiSeq (2 × 300 bp, V3–V4 region of 16S rRNA). Sequence quality filtering and Amplicon Sequence Variant (ASV) inference were carried out using the DADA2 pipeline, and taxonomy was assigned through the SILVA v138 database. Relative abundances were calculated as the proportion of normalized read counts per genus with respect to the total reads per sample.

Table 5.3.a — *Summary of sampling positions and biological analysis.*

Sample ID	**Subsamples (aliquots)**	**Sample description / position**	**Bacterial inoculum**	**Analytical methods**
C1	Top - Rhod-Rhodococcus 1	Contaminated sand volume	*Rhodococcus erythropolis*	sequencing
	Medium - Rhod-Rhodococcus 2			
	Bottom - Rhod-Rhodococcus 3			
C2	Top - Rhod-Coli 1	Contaminated sand volume	*Escherichia coli*	sequencing
	Medium - Rhod-Coli 2			
C3	Medium sample - Rhod-Bianco	Uncontaminated sand volume	None	sequencing

Figure 5.3.a — *Samples prepared for genetics analysis.*

In addition to the taxonomic characterization obtained through 16S rRNA gene sequencing, plate-count analyses were performed on samples collected at the end of the monitoring period to assess bacterial viability and growth potential. Counts conducted after 24 h and 48 h incubation indicate high levels of viable bacteria within the contaminated zone. In several samples, colony numbers exceeded the reliable counting range at low dilution levels, particularly after 48 h incubation, suggesting the presence of stress-adapted or slow-growing populations capable of delayed proliferation once transferred to favorable laboratory conditions.

These observations are consistent with the genetic results, which reveal a bacterial community dominated by hydrocarbon-tolerant and environmentally resilient genera, including Immundisolibacter, Rhodococcus, and Pseudomonas in the Rhodococcus-inoculated sector, and by Aquabacterium in the Escherichia coli sector. The coexistence of these taxa supports the interpretation of a structured microbial community shaped by long-term exposure to hydrocarbon contamination and limited nutrient availability.

Importantly, the plate-count data are not interpreted as a quantitative measure of in situ biomass, but rather as qualitative evidence of microbial persistence and viability at the end of the experiment. When considered together, genetic and culturable data indicate that the contaminated system hosted an active and differentiated microbial community, capable of sustained survival under extreme environmental conditions. This biological context provides an essential framework for interpreting the electrical variability observed during the ERT monitoring, without implying a direct or linear relationship between bacterial abundance and electrical response.

5.3.2 Taxonomic composition and dominant genera

The bacterial community was dominated by a limited number of taxa, accounting for more than 95 % of total reads. Across all samples, the most abundant genera were *Immundisolibacter*, *Rhodococcus*, *Aquabacterium*, and *Pseudomonas*, with minor contributions from *Bacillus* and other low-abundance taxa (< 1 %).

In the *Escherichia*-inoculated sector, the genus *Aquabacterium* clearly dominated (≈ 90 %), followed by small proportions of *Pseudomonas* and *Immundisolibacter*. This pattern is consistent across both upper (Coli-1) and middle (Coli-2) layers, suggesting a homogeneous community established in that region.

Conversely, the *Rhodococcus* sector exhibited a much more diverse composition. *Immundisolibacter* increased progressively with depth, from ≈ 35 % in Rhodococcus-1 (top) to ≈ 80 % in Rhodococcus-3 (bottom). *Pseudomonas* and *Rhodococcus* contributed between 5 % and 25 %, showing coexistence of hydrocarbon-degrading and redox-active species. The uncontaminated blank sample displayed only residual bacterial presence, dominated by "others < 1 %," confirming negligible biological activity in the pristine matrix.

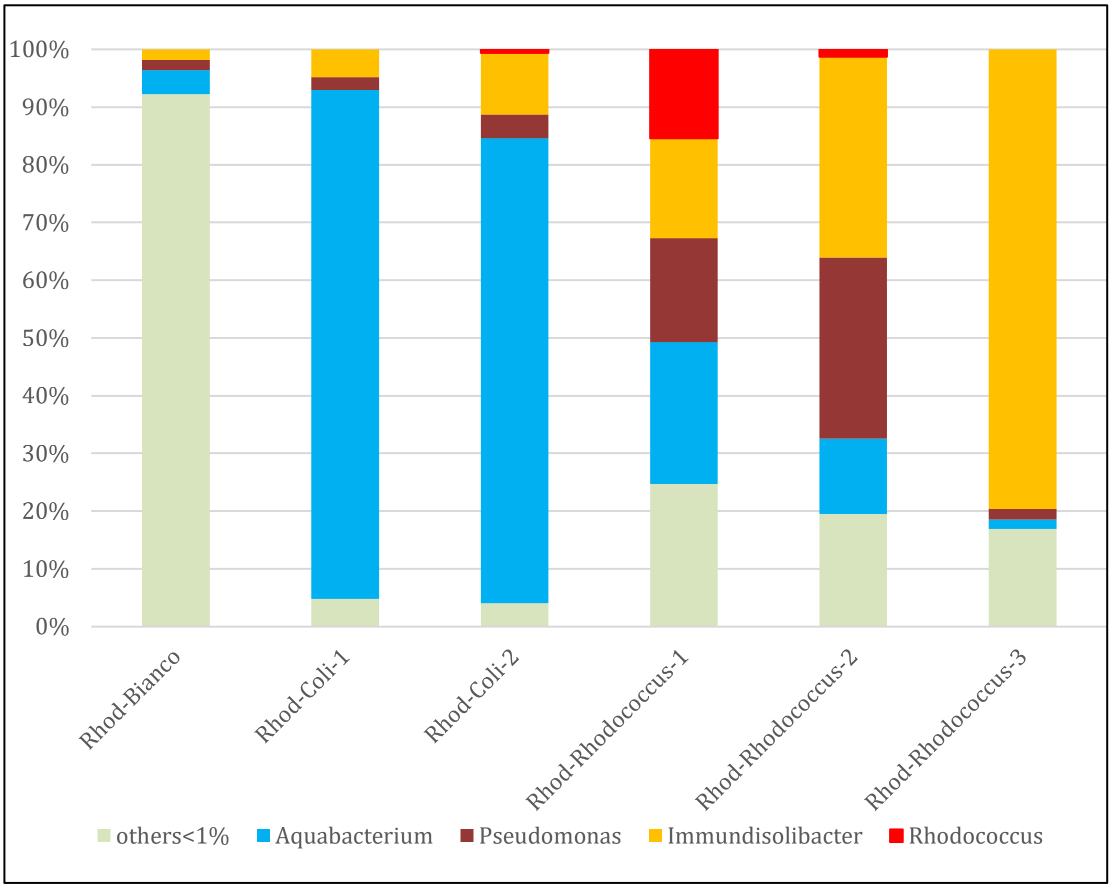

Figure 5.3.b — *Principal genera distribution across samples.*

5.3.3 Sample points distribution.

To relate the microbiological observations to the physical structure of the system, the sampling locations were projected onto the inverted 3D ERT model of the contaminated region. The *Rhodococcus erythropolis* and *Escherichia coli* samples were collected at the two opposite ends of the contaminated block, directly beneath their respective injection tubes. A third sample (“blank”) was collected outside the electrically defined contaminated region of interest and was used as a reference for sediment not directly impacted by bacterial inoculation. As discussed in previous sections, this blank does not represent pristine material but rather a zone not subjected to targeted biological stimulation.

The 3D clipped resistivity model of the contaminated volume (Fig. 5.3.c) highlights a well-defined resistive nucleus (>180 Ω·m), interpreted as the diesel-impregnated core, surrounded by a more conductive halo (approximately 120–140 Ω·m). This conductive envelope is attributed to be a zone with a lower hydrocarbon’s concentration, the diffusion zone, influenced by ionic redistribution but without microbial activity. The resulting geometry delineates a physically coherent framework within which microbial communities evolved, allowing taxonomic differences between sampling points to be interpreted in relation to a clearly constrained electrical and environmental context.

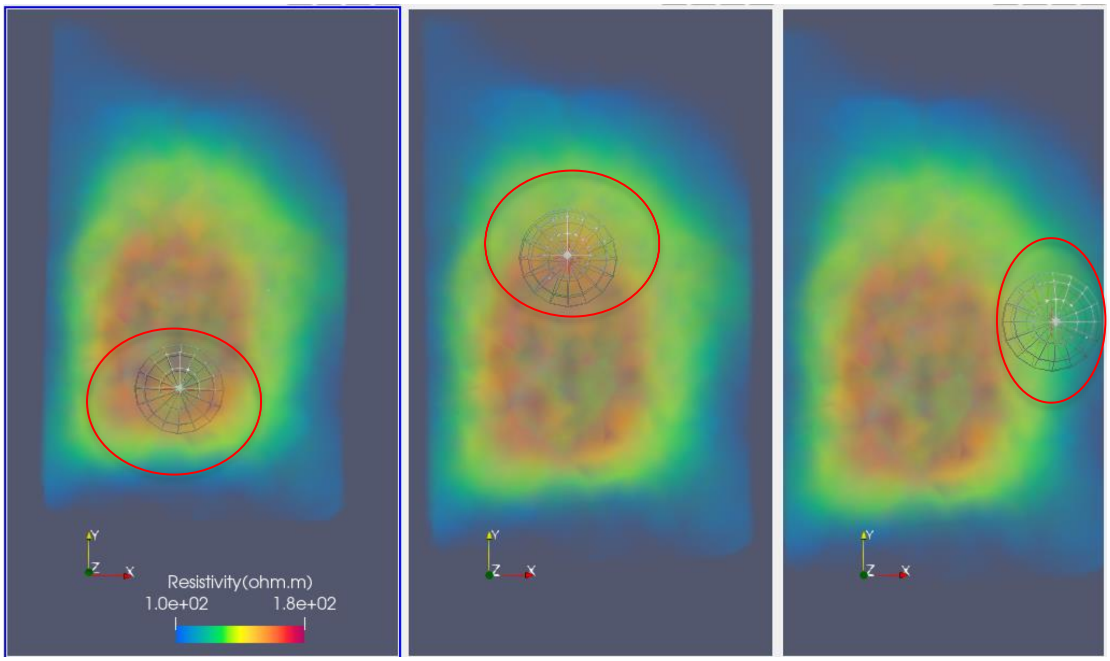

Figure 5.3.c — *Point of sampling locations (left R.erythropolis, medium E.coli, right "blank").*

5.3.4 Summary of genetic findings.

The genetic analyses provide an internal consistency check of the experiment, confirming a differentiation of bacterial communities within the same diesel-contaminated block following the two opposite inoculations. The sequencing results indicate a measurable vertical differentiation within the extracted cores. In particular, relative abundances vary between the upper and intermediate aliquots, suggesting that the microbial community was not vertically uniform within each sampling location. Therefore, the observed genetic contrasts reflect both lateral differentiation between the two inoculation sides and vertical gradients within each core, rather than a purely horizontal separation.

The sector inoculated with Rhodococcus erythropolis shows an enrichment in hydrocarbon-associated genera, with Rhodococcus being most evident in the upper aliquot and decreasing in the intermediate aliquot. Across the same samples, Immundisolibacter and Pseudomonas remain comparatively stable, while Aquabacterium is consistently minor in this sector.

Conversely, the sector inoculated with Escherichia coli is dominated by Aquabacterium, but the vertical comparison indicates a structured pattern: Rhodococcus is detectable in the intermediate aliquot while absent from the upper aliquot, and the relative balance among Immundisolibacter and Pseudomonas varies accordingly.

Importantly, DNA attributable to both inoculated strains was detected within the contaminated core, indicating that microbial cells—or their genetic material—were not confined to the immediate vicinity of the injection points. Instead, lateral redistribution within the diesel-impregnated matrix occurred, consistent with physical mixing, diffusion, and capillary-driven processes within the porous medium. This observation supports the interpretation that the contaminated volume behaved as a connected system rather than as a set of isolated compartments.

Overall, the sequencing results confirm the coexistence of laterally differentiated microbial communities within the same contaminated block, together with the persistence of an autochthonous bacterial assemblage originating from the experimental materials and background conditions. This spatial diversification is consistent with the electrical heterogeneity resolved by ERT and reinforces the interpretation of a coupled eco-physical response driven by microbial activity within a non-stratified but dynamically connected system.

5.4 Final chemical characterization of the sandbox system.

At the end of the monitoring campaign, a set of chemical analyses was performed to provide an independent end-point characterization of the polluted volume and a blank point alongside. These analyses were not designed to resolve temporal dynamics or vertical gradients during the monitoring period, but rather to verify the final spatial extent and persistence of hydrocarbon contamination within the experimental volume.

5.4.1 Sampling strategy and analytical scope

Chemical samples were collected after completion of the ERT monitoring campaign, by extraction of sediment cores from the sandbox. Each core was homogenized over its entire length prior to analysis and after the microbiological aliquot sampling. Consequently, no distinction between surface, intermediate, or basal layers is made in the chemical dataset. The analytical results therefore represent an integrated characterization of the sampled volume rather than depth-resolved information.

Three sampling locations were considered: the two zones corresponding to the original bacterial inoculations and a nominally uncontaminated reference zone (“blank”). It is important to note that the blank sample does not represent pristine material, as the sandbox was subjected to an extended aging period (approximately one year) prior to the experiment. During this period, hydrocarbon migration and redistribution were expected to occur, potentially affecting areas initially considered uncontaminated.

The objective of the chemical analyses was thus limited to assessing the presence, persistence, and spatial spread of hydrocarbon compounds at the end of the experiment, providing an external constraint for the interpretation of geophysical observations.

5.4.2 Summary of chemical results

End-point chemical analyses were performed on material collected from the extracted cores at the end of the monitoring period. Because subsampling was carried out on homogenized core material, the chemical results represent bulk conditions of each core and do not resolve vertical gradients within the contaminated interval. Table 5.4.a reports the analytical outputs for the three reference samples (blank, *Escherichia* side, *Rhodococcus* side).

Table 5.4.a — *Summary of chemical analysis results.*

	ppm (mg/Kg)	esadecano	n-c17	c19	n-c17/c19
BIANCO	2453.9	8.5	10.11	7.4	1.37
E.coli	6580.5	35.0511	38.35	30.61	1.25
Rhodococcus	7749.7	49.42	53.341	33.95	1.57

Detectable hydrocarbon concentrations were measured in all samples, including the blank core. This indicates that the system cannot be considered chemically compartmentalized at the sandbox scale at the time of sampling. Differences among samples are interpreted here as spatial variability of residual contamination and sampling heterogeneity, rather than as quantitative evidence of degradation. No mass balance or degradation rate is derived because baseline (pre-aging) chemical concentrations are not available. Collectively, the results presented in this chapter provide a multi-scale and internally consistent description of the electrical, biological, and chemical evolution of the sandbox system over the duration of the experiment. Statistical analysis of the full apparent-resistivity dataset highlights a temporally structured and non-random evolution characterized by distinct phases, transient perturbations, and progressive changes in variability. Three-dimensional inversions, performed using both independent and time-lapse strategies on a representative subset of acquisition steps, translate these temporal trends into coherent spatial patterns, revealing the persistence and gradual transformation of a resistive contaminated nucleus surrounded by a more conductive halo.

The convergence between independent inversions and time-lapse inversion results demonstrates first-order consistency in anomaly polarity, geometry, and temporal ordering, supporting the robustness of the inversion framework. The biological characterization confirms the establishment of differentiated microbial communities within the contaminated volume, while the detection of microbial DNA inside the diesel-impregnated core indicates lateral and internal accessibility of the polluted matrix. End-point chemical analyses further confirm the persistence of hydrocarbon contamination and its spatial diffusion beyond the original source volume, including zones initially designated as uncontaminated.

Importantly, each dataset is interpreted here within its own observational scope and limitations. No single line of evidence is used in isolation, and no quantitative coupling between electrical, biological, and chemical parameters is imposed at this stage. Instead, the results collectively define a set of empirical constraints on the spatial extent, temporal evolution, and internal connectivity of the system.

These constraints form the basis for the integrative interpretation developed in Chapter 6, where the observed electrical patterns are discussed in relation to microbial dynamics, contaminant redistribution, and eco-physical processes operating under extreme environmental conditions. The discussion builds upon the results presented here to explore mechanistic hypotheses, while explicitly acknowledging the experimental boundaries and uncertainties inherent to the system.

6 Discussion

6.1 Interpretative hypothesis and eco-physical framework

My interpretative logic follows a discovery-by-convergence approach, whereby initially unexpected observations acquire meaning when independent lines of evidence align. In this study, similar electrical behaviours observed in different portions of the sandbox—namely the diesel-contaminated unsaturated zone and the lower section affected by percolated hydrocarbons at the capillary fringe—together with microbial patterns and taxonomic variations, provide complementary perspectives that converge toward a coherent interpretation of bacterial community evolution under extremely toxic and nutrient-limited conditions.

Before the start of monitoring, the diesel-contaminated system was already in a partially equilibrated state in terms of both hydrocarbon distribution and microbial presence. During the long aging period preceding the experiment, diesel progressively spread through the sandy matrix: lighter fractions remained mainly within the unsaturated zone—where bacterial inoculation was later performed—while heavier fractions percolated downward, accumulating on and within the internal water table (≈ 40 L, as described in Chapter 3). Consequently, the electrical signals recorded during the monitoring phase represent an integrated eco-physical response combining moisture redistribution, ionic strength evolution, and microbial activity, rather than the manifestation of a single dominant process (Atekwana & Slater, 2009; Singha et al., 2014).

This configuration generated a complex electrical background, shaped both by the bidirectional expansion of hydrocarbons and by the presence of an autochthonous microbial community. Such a community likely originated from the sand, gravel, and water used in the setup: although sterilization procedures were applied, autoclaving cannot guarantee complete microbial removal and may leave spores or biofilm-protected cells viable (Markowicz et al., 2016; Pessacq et al., 2015).

Bacterial suspensions of *Rhodococcus erythropolis* and *Escherichia coli* were injected under slight overpressure directly into the contaminated unsaturated volume. This injection method, combined with subsequent daily aeration, promoted physical dispersion of microorganisms both laterally and vertically.

The documented presence of *Rhodococcus* beyond its nominal injection sector—specifically within the *Escherichia* side—demonstrates that microbial dispersion was not strictly confined to the original experimental layout. When considered together with the effective capillary redistribution responsible for hydrocarbon percolation toward the lower portion of the sandbox, this observation provides a physically plausible pathway for partial downward transport of microbial cells and/or their metabolic products.

Although direct microbiological evidence from deeper layers is not available, the convergence of physical, electrical, and biological observations suggests that bio-ionic processes were not limited to the shallow contaminated zone.

As a consequence, the same electrical response associated with microbial community development observed in the contaminated volume also appears in the lower part of the sandbox, albeit with slight hysteresis (delayed onset and prolonged response). This explains why the entire box exhibited a coherent electrical evolution despite the initially contaminated volume representing only about 0.34 % of the total sandbox volume.

The vertical profile (Fig. 5.2.o) further supports this interpretation, showing increased resistivity both in the contaminated surface zone and in the lower portion of the sandbox, indicative of the coexistence of resistive lenses with residual oil and conductive bands related to ion-enriched or biofilm-coated layers

Focusing on the contaminated volume, for which microbiological samples are available, and in addition to the data discussed in Section 5.2.4 (normalized to time zero), Figures 6.1.a–6.1.b illustrate the temporal evolution (top view) of resistivity derived from the time-lapse inversions. The electrical and microbiological observations can be read as a continuous sequence, in which each stage reflects a balance between microbial growth, substrate utilization, and ionic reorganization within the system.

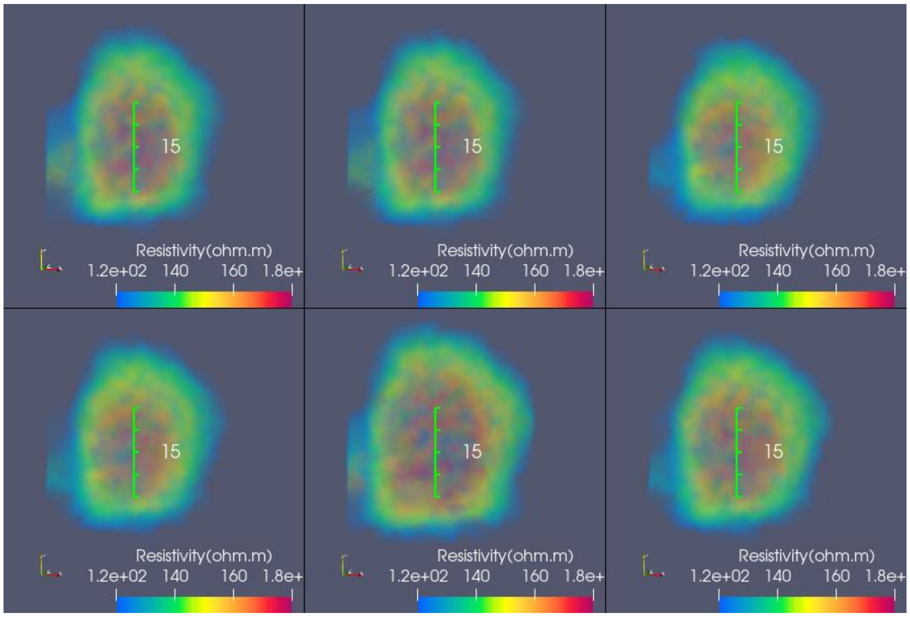

Figure 6.1.a — *Top-view resistivity distribution for the early monitoring stage. From Top left T00, T01, T02, T03, T11 and T20, showing the resistive nucleus of the contaminated block and the initial conductivity gradient*.

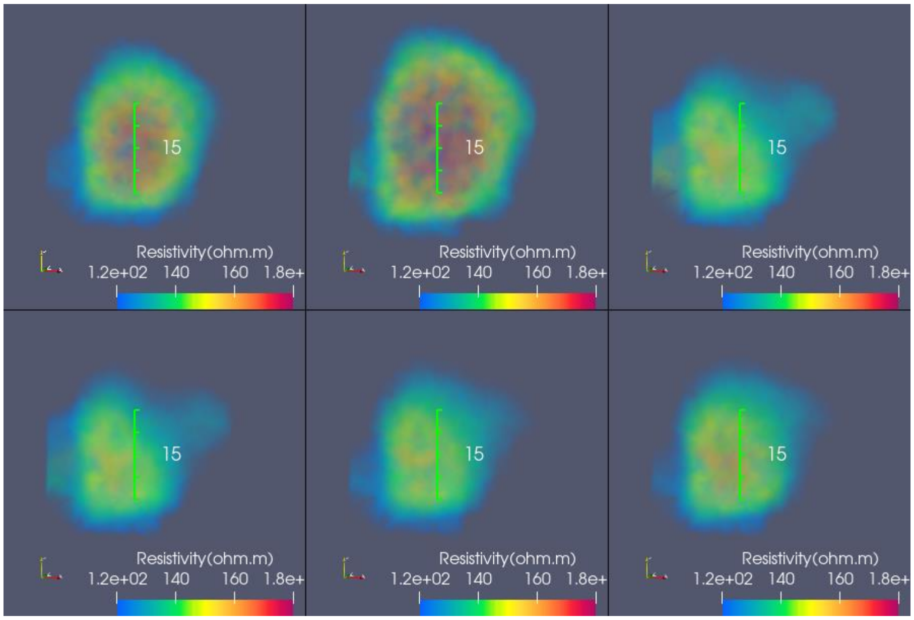

Figure 6.1.b — *Top-view resistivity distribution for the later stage from top left T40, T49, T50, T51, T52, T53. T49 represents the last pre-booster state, whereas T50–T53 illustrate the progressive attenuation of the central resistive anomaly following the injection of the saline–nutrient solution (NaCl with P, N and citrate).*

At the initial steps (T00–T01), resistivity remained stable (~140–150 Ω·m), indicating hydrostatic and electrical equilibrium. Three hours after inoculation (T02), a slight decrease was recorded, attributable to the physical perturbation produced by injection and to redistribution of ionic pore water. Within 24 hours (T03), resistivity returned close to baseline, suggesting equilibration of the injected suspension within the porous network. Beyond this initial physical transient, the subsequent alternation of resistivity increases and decreases through time cannot be explained by injection effects alone. Instead, the observed cyclic behaviour is consistent with a progressive redistribution of resources within the contaminated volume, governed by interactions between functionally distinct microbial groups. In this framework, early interface-modifying activity facilitates access to hydrocarbons, while secondary populations exploit released substrates and metabolites, leading to a dynamic reorganization of ionic pathways and electrical properties.

After approximately one week (T11), a marked increase in resistivity developed within the contaminated volume, clearly visible both in the 3D inverted models and in the mean resistivity trends (Fig. 6.1.c). This resistive phase is interpreted as the onset of microbial structuring and biofilm development. In particular, *Rhodococcus erythropolis* is known to produce trehalolipid biosurfactants and to possess a mycolic acid–rich cell envelope, which reduce interfacial tension, enhance adhesion to hydrophobic substrates, and promote micro-scale compartmentalization of pore space (de Carvalho & da Fonseca, 2005; Pacheco et al., 2010; Chen et al., 2013). Such processes decrease effective ionic connectivity and promote local polarization effects, resulting in an increase in bulk resistivity (Masy et al., 2016).

Around two weeks after inoculation (T20), resistivity decreased again, marking the transition toward a more conductive regime. This phase is consistent with the onset of cooperative microbial activity, in which ions and soluble metabolites released during primary hydrocarbon transformation enhanced pore-water conductivity and supported the development of secondary microbial populations, including *Pseudomonas*, *Aquabacterium*, and *Immundisolibacter* (Atekwana & Slater, 2009; Corteselli et al., 2017).

By approximately 45 days (T40), the decreasing trend continued across the contaminated volume, confirming sustained microbial activity and progressive accumulation of conductive metabolic by-products. This stage corresponds to the most conductive phase observed in the mean resistivity curves, particularly within the *Rhodococcus*-inoculated sector (Fig. 6.1.c).

At later times (T49), resistivity increased again within the contaminated volume, most likely reflecting ionic reorganization, partial oxidation or consumption of previously released metabolites, and a temporary reduction in conductive pathways prior to renewed stimulation (Johnson et al., 2010b; Masy et al., 2016). This secondary resistive phase is clearly expressed in the *Rhodococcus* curve, which reaches its highest values over the entire monitoring period.

Following the saline–nutrient booster injection (T50), a sharp decrease in resistivity was observed, particularly within the contaminated volume. This response reflects the combined effect of increased ionic strength and microbial reactivation. Two hours after injection, a highly conductive layer formed near the surface, partially masking the resistive core, while by the following day (T51) resistivity stabilized at lower values, indicating renewed metabolic activity supported by nutrient availability (Abdel Aal et al., 2014; Masy et al., 2016). This stabilized conductive regime persisted until the end of the experiment (T53).

These dynamics are summarized in Figure 6.1.c, which reports the mean resistivity evolution for the *Rhodococcus*, *Escherichia coli*, and blank zones. The *Rhodococcus* region exhibits the strongest non-monotonic behaviour, characterized by an initial resistivity increase followed by a prolonged conductive phase and a secondary resistive peak. In contrast, the *E. coli* sector shows a more moderate response, while the blank zone remains nearly stable (±5 %) throughout the experiment. The muted electrical response in the blank area, despite the chemical presence of hydrocarbons, indicates that the absence of primary degraders limited the initiation of structured bioelectrochemical processes.

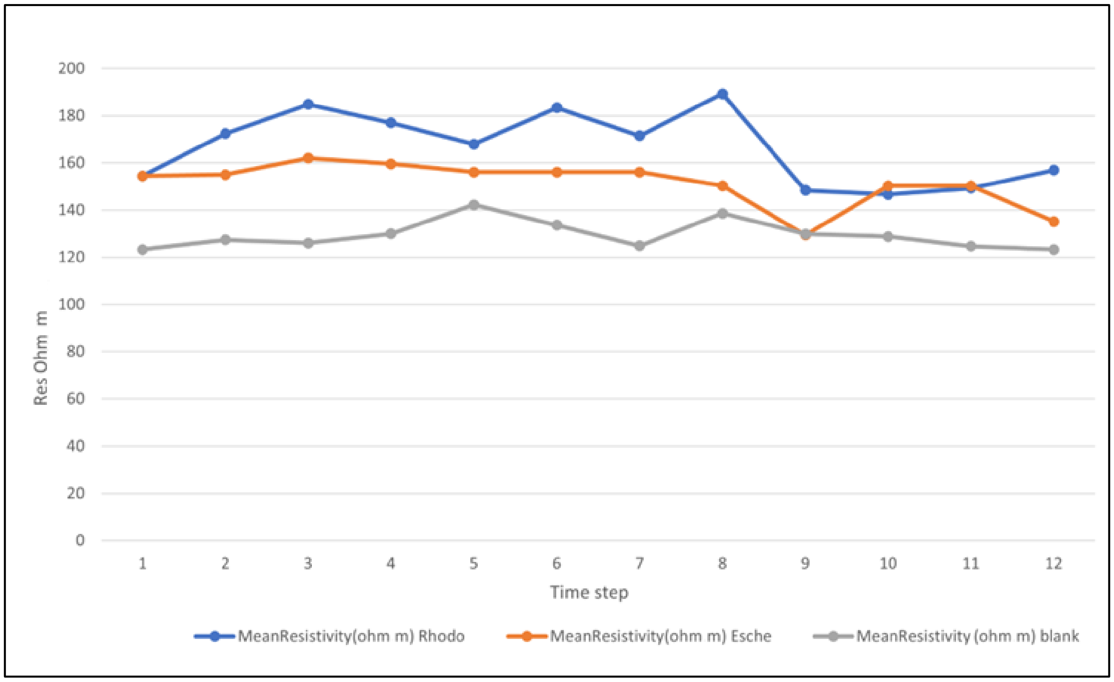

Figure 6.1.c — *Mean resistivity (Ω·m) versus time step for the Rhodococcus, Escherichia coli, and blank zones. The Rhodococcus-inoculated region displays pronounced non-monotonic behaviour, reflecting successive phases of microbial structuring, cooperative degradation, and ionic reorganization. The E. coli zone shows a weaker and delayed response, while the blank sector remains largely stable, highlighting the key role of specialized degraders in driving the observed electrical dynamics.*

To interpret these electrical dynamics in ecological terms, it is necessary to examine the taxonomic composition of the microbial community at the end of the experiment. Referring to Figure 5.3.b**,** the dominant genera detected at the end of the experiment can be interpreted as a functionally coherent consortium rather than as isolated taxonomic signatures.

Rhodococcus erythropolis (phylum Actinobacteria) is a Gram-positive bacterium characterized by a lipid-rich, mycolic-acid cell envelope, a trait widely associated with strong adhesion to hydrophobic substrates, tolerance to hydrocarbon toxicity, and survival under nutrient-limited conditions (de Carvalho & da Fonseca, 2005; Laczi et al., 2015). In oil-impacted porous media, these interface-adapted properties promote early colonization of hydrocarbon droplets, biosurfactant production (e.g. trehalolipids), and biofilm or exopolymeric matrix development, leading to localized restructuring of pore-scale connectivity and ionic pathways (Pacheco et al., 2010; Chen et al., 2013). This provides a plausible functional basis for the early resistivity increase observed after inoculation.

Alongside *Rhodococcus*, Figure 5.3.b also shows several Gram-negative genera commonly reported as secondary or downstream actors in hydrocarbon-impacted soils. *Pseudomonas* spp. are well known for producing rhamnolipid biosurfactants that enhance hydrocarbon emulsification and bioavailability, thereby supporting cooperative degradation pathways and potentially increasing ionic mobility at the mesoscale (Salazar-García et al., 2025; Wang, 2021).

Aquabacterium spp. are Gram-negative, strictly aerobic bacteria typically described as metabolically versatile organisms capable of exploiting soluble organics and intermediate compounds rather than acting as primary hydrocarbon degraders. Species such as *Aquabacterium terrae* have been isolated from soil environments and are associated with aerobic downstream utilization of organic intermediates, consistent with a stabilizing role during later stages of community development (Dahal et al., 2021; Feng et al., 2023).

Finally, *Immundisolibacter* emerges as a specialist associated with the degradation of high–molecular-weight aromatic hydrocarbons. DNA-SIP, metagenomic, and functional network analyses identify members of this genus as dominant benz(a)anthracene degraders in contaminated soils, with their abundance modulated by co-occurring PAHs and nutrient availability (Jiménez-Volkerink et al., 2023; Chen et al., 2024). Such specialization toward recalcitrant aromatic fractions is consistent with late-stage community reorganization and competitive interactions among degraders.

Additional independent evidence comes from SVD analysis of temperature-corrected $\Delta\rho$ % residuals (Fig. 5.2.r). The decomposition of resistivity fields shows that most variance is concentrated in three main modes: SVD1 highlights the resistivity decrease associated with microbial community structuring; SVD2 reflects the differentiated evolution between Rhodococcus and Escherichia regions; and SVD3 represents internal transient dynamics related to ionic redistribution and biofilm fluctuations.

The persistence of these signatures after temperature correction confirms that the observed resistivity variations are primarily governed by non-thermal bioelectrochemical processes, consistent with the proposed eco-physical interpretation. In this sense, the time-lapse ERT monitoring captures not only the presence and redistribution of contamination, but also the temporal signature of inter-genus dynamics governing resource availability and ionic organization within an extreme, nutrient-limited system.

6.2 Data sonification to analyse temperature effect

The thermal correction applied to the raw data was validated through a parallel sonification process Following the sonification framework proposed by Dell'Aversana et al., 2016, by which the entire data set of measure (Vp and In current) has been converted into sound to assess the impact of temperature.

The entire dataset captures a superposition of slow thermal–hydraulic processes and fast, transient, microbially or ionically driven events. Therefore, to interpret resistivity variations as authentic biogeophysical signatures, it was essential to verify that the temperature effect was correctly identified and separated, ensuring that the residual signal reflects biotic and ionic processes. Three complementary datasets were analyzed for each time step: the apparent resistivity variation ($\Delta\rho = (\rho(t) - \rho_0)/\rho_0$), the statistical decomposition obtained through RPCA (L-mean and S_mean components), and the mean temperature of the cell. These numerical data were then complemented by a sonification approach, following the conceptual framework proposed by Dell'Aversana et al. (2017). Here, the measured potential differences |mV|—the physical quantities originally recorded by the Syscal—were mapped to audible frequencies, with |mV| controlling pitch, z corresponding to time, and x controlling stereo position. This mapping returns directly to the raw voltage ΔV (in mV), which, when combined with the injected current In and the geometric factor k, determines apparent resistivity through $\rho_a = k \cdot \Delta V / I$. In this way, the sonification preserves the physical meaning of the measurements while offering an intuitive, perceptual form of data analysis.

After converting the ERT time series into a continuous chronological sound sequence, Harmonic–Percussive Source Separation (HPSS) was applied to decompose the audio into harmonic (slow, sustained energy, equivalent to L) and percussive (short, transient energy, equivalent to S) components. This method was conceived not as an artistic experiment, but as a side project to verify that temperature was not the primary factor controlling resistivity changes. By linking physical, statistical, and auditory representations of the same process, the approach provided an independent perceptual validation of the temperature correction.

The auditory analysis revealed a clear distinction between the components**.** Fig. 6.2.a shows the temporal evolution of the normalized RMS energy for the harmonic (green), percussive (red), and cleaned (blue) signals. The harmonic component dominates and changes slowly, reflecting the thermal–hydraulic background, whereas the percussive component is sharper and more irregular, matching transient, non-thermal fluctuations associated with biotic and ionic activity. The cleaned signal preserves the transient structure while suppressing slow variations, reproducing the temperature-free $\Delta\rho$ pattern. In practical terms, this means that when listening to the cleaned audio track, one is effectively hearing only the fast variations associated with microbial and ionic evolution—the biological activity expressed through its electrical signature.

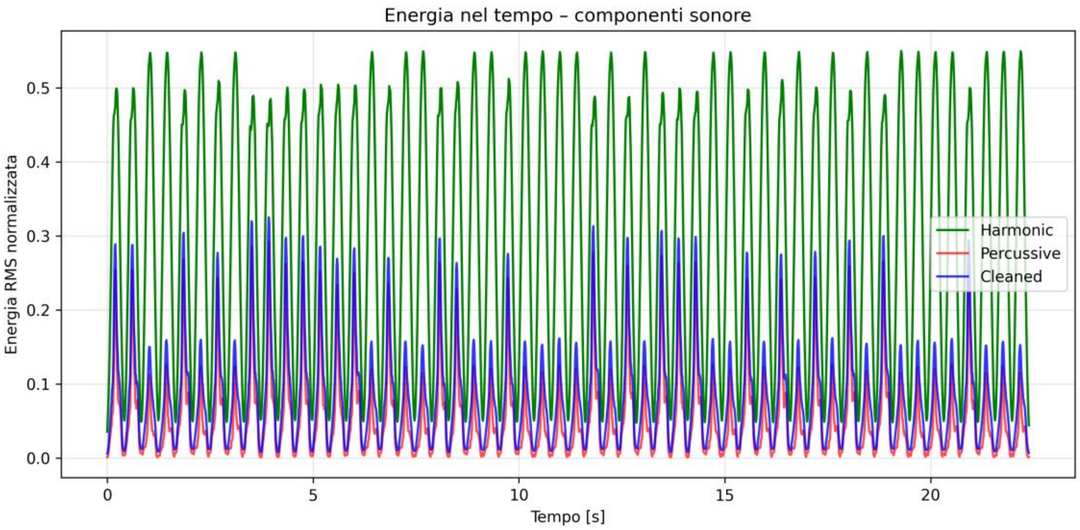

Figure 6.2.a — *temporal evolution of the normalized RMS energy for the harmonic (green), percussive (red), and cleaned (blue) signals*

Complementarily, Fig. 6.2.b displays the averaged frequency spectra of the same components. The harmonic energy (green) concentrates at low frequencies ($<10^2$ Hz), corresponding to slow temperature-related responses, while the percussive component (red) extends to higher frequencies (up to $\sim10^3$ Hz), representing short-lived, non-thermal dynamics. The cleaned spectrum (blue) bridges the two, depicting the combined yet temperature-corrected behaviour of the system. These patterns confirm that sonification captures the same physical partition obtained through RPCA: temperature controls the harmonic, low-frequency content, while microbial and ionic processes dominate the percussive, high-frequency range.

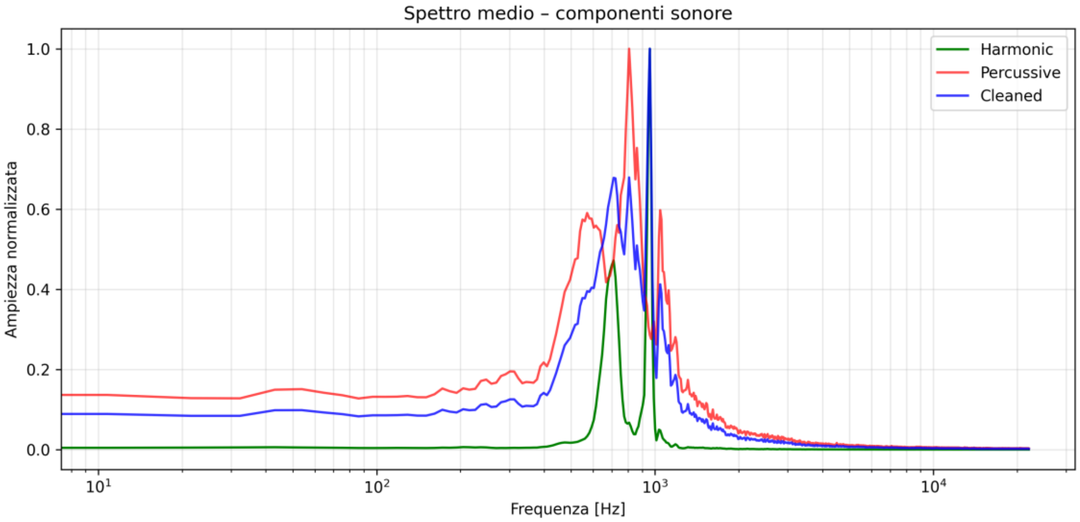

Figure 6.2.b — *averaged frequency spectra of the same components. The harmonic energy (green) concentrates at low frequencies (<10^2 Hz), corresponding to slow temperature-related responses, while the percussive component (red) extends to higher frequencies (up to ~10^3 Hz), representing short-lived, non-thermal dynamics.*

When comparing the auditory and statistical domains, the correspondence becomes evident. The harmonic audio energy mirrors the temperature trend and the L-mean component, whereas the percussive bursts align with S_mean and with the residual $\Delta\rho$ after temperature regression. Two distinct analytical views therefore converge on the same interpretation: thermal = harmonic, and biotic/ionic = percussive. This agreement confirms the robustness of the temperature correction and strengthens the conclusion that the main resistivity fluctuations are biologically mediated, not thermally induced.

7 Conclusions

This research demonstrates that time-lapse Electrical Resistivity Tomography (ERT) can successfully capture the evolution of microbial and ionic processes in contaminated porous media. The combination of 3D inversion, multivariate analysis (PCA/RPCA), and microbiological data produced an integrated biogeophysical interpretation framework capable of identifying dynamic phenomena associated with hydrocarbon degradation. The 73-day laboratory experiment reproduced the conditions of a natural "bioremediation" process, providing both methodological and conceptual insights into how microbial activity influences subsurface electrical properties. From a methodological standpoint, it confirmed that ERT can resolve time-dependent variations linked to microbial metabolism when supported by robust statistical decomposition and careful temperature correction. The integration of PCA and RPCA successfully distinguished the global conductive trends from transient localized phenomena, offering a statistically consistent framework for separating biotic and abiotic influences. The approach demonstrated that electrical signals are not dominated by random noise but by structured and recurrent changes, whose evolution mirrors microbial growth, substrate transformation, and ionic redistribution.

Overall, these results demonstrate that temperature acts only as a slow, secondary driver, while the transient signals—retained after normalization and regression—represent genuine biotic or ionic transformations. The sonification approach thus proves valuable not only as a communicative tool but as an effective diagnostic instrument: when the sound is harmonic, temperature dominates; when it becomes percussive, microbial and ionic dynamics prevail.

In summary, the validated workflow can be expressed as: $\Delta\rho(t) \rightarrow$ RPCA(L,S) $\rightarrow$ Sonification(HPSS) $\rightarrow$ Thermal Regression $\rightarrow$ Residual Analysis $\rightarrow$ Cross-Correlation Check. Combining the $\Delta\rho$–T correlation, the residual behaviour of S and L components, and the auditory decomposition (Fig. 6.2.b) provides a comprehensive demonstration that the temperature effect can be isolated and controlled, while the remaining electrical variability preserves the authentic biotic narrative of resistivity evolution.

Looking ahead, this integrated method could evolve into a real-time monitoring system, capable of translating electrical variations into audible feedback. By continuously transforming resistivity data into sound, operators may one day perceive the microbial or ionic evolution of subsurface environments directly through listening. Future work will focus on analyzing the audio progression of microbial community development, exploring whether specific frequency signatures correspond to microbial succession or metabolic shifts.

8 Bibliography

Abdel Aal, G.Z. & Atekwana, E.A. (2014). Effect of microbial processes on geoelectrical signatures of hydrocarbon-contaminated sediments: Laboratory and field-scale experiments. Geophysics, 79(2), B101–B112.

Abdel Aal, G.Z., Atekwana, E.A., Radzikowski, S.E., & Rossbach, S. (2004). Effect of microbial processes on electrolytic and interfacial electrical properties of porous media. Geophysical Research Letters, 31(12), L12505.

Abdulkadir, M., Atekwana, E.A., Werkema, D.D., & Slater, L.D. (2019). Time-lapse electrical resistivity tomography for monitoring hydrocarbon microbially mediated transformation (MMT) under controlled conditions. Journal of Applied Geophysics, 167, 103–117.

An, D., Caffrey, S.M., Soh, J., et al. (2013). Metagenomic analysis reveals highly diverse carbon fixation microorganisms in a petroleum-hydrocarbon-contaminated aquifer. *Applied and Environmental Microbiology*, 79(12), 3869–3877

Atekwana, E.A. & Slater, L.D. (2009). Biogeophysics: A new frontier in Earth science research. Reviews of Geophysics, 47, RG1003.

Atekwana, E.A., Sauck, W.A., & Werkema, D.D. (2000). Investigations of geoelectrical signatures at hydrocarbon contaminated sites. Journal of Applied Geophysics, 44, 167–180.

Atekwana, E.A., Werkema, D.D., & Atekwana, E.A. (2004). Biogeophysical signatures of hydrocarbon microbially mediated transformation and microbial activity. Journal of Environmental and Engineering Geophysics, 9(1), 9–19.

Besson, A., Hayley, K., & Binley, A. (2019). Quantifying temperature effects on electrical resistivity in porous media. Hydrology and Earth System Sciences, 23, 437–451.

Binley, A. & Kemna, A. (2005). Electrical methods for subsurface characterization: A review. In Hydrogeophysics (Eds. Y. Rubin & S. Hubbard). Springer, pp. 129–156.

Binley, A. & Slater, L. (2020). Resistivity and Induced Polarization: Theory and Applications to the Near-Surface Earth. Cambridge University Press.

Blanchy, G., Boyd, J., Mathias, S.A., & Binley, A. (2020). ResIPy: An intuitive open source GUI for complex geoelectrical inversion and model management. Computers & Geosciences, 137, 104423.

Callahan, B.J., McMurdie, P.J., Rosen, M.J., et al. (2016). DADA2: High-resolution sample inference from Illumina amplicon data. Nature Methods, 13, 581–583.

Chambers, J.E., Wilkinson, P.B., Uhlemann, S., et al. (2014). Geophysical monitoring of hydrogeological processes using automated time-lapse ERT. Near Surface Geophysics, 12(4), 413–426.

Chen, T.-W., Tsai, W.-H., Chang, Y.-C., et al. (2024). Characterization of prokaryotic community dynamics and functional profiles in soils contaminated long-term with petroleum hydrocarbons in response to the addition of soil bioremediation nutrients. *Journal of Hazardous Materials*, 454, 131479.

Clement, R. & Moreau, S. (2016). On the quality metrics and stability of 3D tetrahedral meshes for electrical resistivity tomography. Geophysical Journal International, 205, 1043–1056.

Dahal, R.H., Han, J.Y., Lee, H., Chaudhary, D.K. & Kim, D.-U. (2021). *Aquabacterium terrae* sp. nov., isolated from soil. *International Journal of Systematic and Evolutionary Microbiology*, 71(8), 004617.

Dahlin, T. (2000). Short note on electrode charge-up effects in DC resistivity data acquisition using multi-electrode arrays. Geophysical Prospecting, 48(1), 181–187.

Dell'Aversana, P., Gabbriellini, G., and Amendola, A. (2016). Sonification of geophysical data through time–frequency analysis: theory and applications. Geophysical Prospecting, 65(1), 146–157.

de Carvalho, C.C.R. & da Fonseca, M.M.R. (2005a). The remarkable Rhodococcus erythropolis: Strain diversity and biotechnological potential. FEMS Microbiology Ecology, 51, 389–399.

de Carvalho, C.C.R. (2005b). Adaptation of Rhodococcus erythropolis to organic solvents: Cell surface properties and solvent tolerance. Applied Microbiology and Biotechnology, 68, 404–410.

Doetsch, J., Linde, N., Vogt, T., Binley, A., & Green, A.G. (2012). Imaging and quantifying salt transport in a riparian groundwater system by means of 3D ERT monitoring. Journal of Hydrology, 438–439, 25–35.

Feng, L., Yan, J., Zhang, Y., et al. (2023). Characterization of polyhydroxybutyrate (PHB) synthesized by newly isolated rare actinomycetes *Aquabacterium* sp. A7-Y. *International Journal of Biological Macromolecules*, 238, 124096.

Geuzaine, C. & Remacle, J.-F. (2009). Gmsh: A three-dimensional finite element mesh generator with built-in pre- and post-processing facilities. International Journal for Numerical Methods in Engineering, 79, 1309–1331.

Ghazali, F.M., Rahman, R.N.Z.A., Salleh, A.B., & Basri, M. (2004). Microbially mediated transformation of hydrocarbons in soil by microbial consortium. International Biodeterioration & Biodegradation, 54, 61–67.

Hayley, K., Bentley, L.R., & Gharibi, M. (2010). Time-lapse electrical resistivity monitoring of frost and thaw conditions. Journal of Hydrology, 385, 273–284.

Herring, T., Hassen, A., & Binley, A. (2021). Modeling temperature-dependent resistivity changes in soils and sediments. Geophysical Research Letters, 48(2), e2020GL090459.

Hubbard, S.S. & Rubin, Y. (2000). Hydrogeophysics. Water Resources Research, 36(12), 3769–3798.

Jiménez-Volkerink, S.N., Jordàn, M., Benito, G., et al. (2023). Bacterial benz(a)anthracene catabolic networks in contaminated soils and their modulation by other co-occurring high-molecular-weight PAHs. *Environmental Microbiology*, 25(9), 3562–3579.

Karaoulis, M., Revil, A., & Doetsch, J. (2011). Monitoring of hydrological processes using time-lapse ERT: Case studies and methodology. Geophysics, 76(5), G37–G51.

Kharey, R., Li, Z., & Yang, X. (2025). Pangenomic analysis of three putative hydrocarbon-degrading genera. Frontiers in Microbiology, 16, 102345.

Konhauser, K.O. (2007). Introduction to Geomicrobiology. Blackwell Publishing, Oxford.

Li, C., Guo, L., Li, J., & Li, B. (2013). Characterization of Rhodococcus erythropolis and its biosurfactant production for hydrocarbon degradation. Applied Biochemistry and Biotechnology, 171, 1715–1725.

Li, Q., You, P., Wang, J., et al. (2020). Effects of co-contamination of heavy metals and total petroleum hydrocarbons on soil bacterial community and function network reconstitution. *Journal of Hazardous Materials*, 398, 122934

Loke, M.H. (2021). Resistivity and IP Inversion Software Manual. Geotomo Software, Malaysia.

Madigan, M.T., Martinko, J.M., & Bender, K.S. (2018). Brock Biology of Microorganisms (15th ed.). Pearson Education.

Markowicz, A., Piotrowska-Seget, Z., & Wozniak-Karczewska, M. (2016). Ecological succession of microbial communities in long-term diesel-contaminated soils. Archives of Environmental Protection, 42(4), 3–11.

Masy, T., Budach, I., Rossi, M., Revil, A., & Atekwana, E.A. (2016). Electrical resistivity tomography to monitor enhanced biodegradation of hydrocarbons by Rhodococcus erythropolis. Journal of Contaminant Hydrology, 184, 1–13.

Menke, W. (2012). Geophysical Data Analysis: Discrete Inverse Theory (3rd ed.). Academic Press.

Naidu, R., Kookana, R.S., Oliver, D.P., Rogers, S., & McLaughlin, M.J. (Eds.) (1996). Contaminants and the Soil Environment in the Australasia-Pacific Region. Springer, Dordrecht.

Nan, Y., Zhang, Q., Zhang, Y., et al. (2024). Rhodococcus erythropolis-mediated microbially mediated transformation and biosurfactant activity under extreme hydrocarbon load. Environmental Science and Pollution Research, 31, 35332–35352.

Oldenburg, D.W. & Li, Y. (1999). Estimating depth of investigation in DC resistivity and IP surveys. Geophysics, 64(2), 403–416.

Pacheco, G.J., Ciapina, E.M., & de Carvalho, C.C.R. (2010). Characterization of biosurfactants produced by Rhodococcus erythropolis and their role in hydrocarbon degradation. Brazilian Journal of Microbiology, 41, 685–693.

Pessacq, J., Colombo, C., & Morelli, I. (2015). Functional microbial succession in diesel-contaminated soil microcosms. Water, Air, and Soil Pollution, 226, 20.

Piccardi, P., Vessman, B., & Mitri, S. (2022). Ecology of microbial interactions: Priming species and cooperative metabolism. Nature Communications, 13, 5708.

Revil, A., Atekwana, E.A., & Zhang, C. (2012). A model for electrical conductivity of biofilms and hydrocarbon-contaminated porous media. Geophysical Research Letters, 39, L09402.

Revil, A., Karaoulis, M., Johnson, T., & Kemna, A. (2013). Review of resistivity and induced polarization imaging in geophysical monitoring. Geophysical Journal International, 195, 1–24.

Rücker, C., Günther, T., & Spitzer, K. (2006). Three-dimensional modeling and inversion of DC resistivity data incorporating topography—Part 1: Modeling. Geophysical Journal International, 166(2), 495–505.

Salazar-García, L.M., Damas-Ramos, L.C., Martínez-Ramos, A., et al. (2025). CRISPR-driven enhanced hydrocarbon emulsification in an environmental *Pseudomonas aeruginosa* strain. *Environmental Science & Technology*, 59(7), 10215–10225

Sales da Silva, L., Oliveira, F., & Costa, A.M. (2020). Hydrocarbon contamination and bioremediation: A review of microbial and physical processes. Environmental Pollution, 263, 114543.

Shah, M.P. & Deka, D. (Eds.) (2025). Soil Bioremediation. Springer Nature, Cham.

Slater, L.D. (2007). Near surface electrical characterization of hydraulic conductivity. Geophysics, 72(2), F35–F48.

Teng, Y., Li, Y., & Chen, W. (2023). Geoelectrical monitoring of oxidant injection and hydrocarbon remediation processes. Journal of Environmental Management, 332, 117366.

Tsai, C.-J., Hsu, S.-C., & Wang, C.-C. (2025). Characterization of prokaryotic community dynamics and functional profiles in long-term petroleum-contaminated soils. Frontiers in Environmental Science, 13, 1509843.

Tsai, W.-H., Chen, T.-W., Chang, Y.-C., et al. (2025). A field-scale assessment of the efficacy of bioremediation of petroleum hydrocarbon-contaminated soils using two biostimulants. *Journal of Contaminant Hydrology*, 251, 104210.

Wang, G. & Or, D. (2010). Mechanisms and ecological implications of the movement of bacteria in soil. *Soil Biology and Biochemistry*, 42(10), 1612–1620.

Wang, J.-D. (2021). iTRAQ-based characterization of proteomic change in petroleum hydrocarbon-degrading *Pseudomonas aeruginosa* under different pH condition

Werkema, D.D., Atekwana, E.A., Endres, A.L., et al. (2003). Microbial activity and geophysical signatures in hydrocarbon contaminated soils. Journal of Environmental and Engineering Geophysics, 8(1), 45–55.

Wilkinson, P.B., Meldrum, P.I., Chambers, J.E., et al. (2012). Practical approaches to optimizing multi-electrode array configurations for electrical resistivity tomography. Geophysical Journal International, 189(1), 428–442.

Xu, J., Li, Y., & Zhang, C. (2019). Functional shifts and enrichment of hydrocarbon-degrading bacteria during assisted bioremediation. Microbial Ecology, 77, 25–39.

Youssef, S., Shabana, A., & Abo-Amer, A.E. (2020). Diesel-degrading bacteria and the impact of biosurfactant production on hydrocarbon removal. Microbial Cell Factories, 19, 1–14.

Zhang, Q., Lambert, G., Liao, D., et al. (2010). A novel form of collective motion by soil bacteria. *Proceedings of the National Academy of Sciences of the United States of America*, 107(31), 13626–13630.

Acknowledgements

I would like to express my deepest gratitude to the entire staff of the University of Milano–Bicocca for their continuous support and collaboration throughout this doctoral research. Their technical and logistical assistance has been fundamental to the success of this work.

Special thanks go to Alberto Villa, for his scientific guidance and constant encouragement, and to Nicoletta, Elena, and Stefano Basiricò for their valuable help during the experimental setup and data processing.

I am sincerely grateful to the Laboratory of Environmental Microbiology, in particular to Prof. Andrea Franzetti, Alessandra, and Valeria, for their constant support, precision, and dedication in processing and interpreting the microbial data.

Many thanks to Prof. Paolo Frattini and Prof. Giovanni Crosta for their supervision, for believing in this project, and for the insightful discussions that greatly improved the scientific quality of this thesis.

This project was made possible thanks to the collective effort of many people whose personal contributions have been deeply appreciated throughout this journey. Without their support, this research would not have been possible.

My sincere appreciation also goes to Geoinvest S.r.l., whose support made this doctoral experience possible.